Paul-Drude-
Institut für
Festkörperelektronik

Leibniz-Institut im Forschungsverbund Berlin e.V.

AnnualReport 2021

Table of Contents

Scientific Advisory Board of Paul-Drude-Institute 2021

Prof. Dr. Manfred Bayer Fakultät Physik Experimentelle Physik 2 Technische Universität Dortmund Deutschland 2016–2019 2020-2023	**Dr. Martin Behringer** OSRAM Opto Semiconductors GmbH OS CTO TLED R Regensburg Deutschland 2018–2021
Prof. Dr. Oscar Dubon University of California Berkeley, California U.S.A. 2017–2020 2021–2024	**Prof. Nicolas Grandjean** Ecole Polytechnique Federale de Lausanne EPFL SB IPHYS LASPE Switzerland 2018–2021
Dr. Michelle Johannes Center for Computational Materials Science Naval Research Laboratory Washington DC U.S.A. 2018–2021	**Prof. Dr. Dagmar Gerthsen** Karlsruher Institut für Technologie (KIT) Karlsruhe Deutschland 2020-2023
Dr. Heike Riel IBM Research – Zürich Rüschlikon Schweiz 2017–2020 2021-2024	**Prof. Dr. Matthias Wuttig** RWTH Aachen Physikalisches Institut Aachen Deutschland 2013–2017 2018-2021
Prof. Dr. Werner Wegscheider Advanced Semiconductor Quantum Materials Laboratory for Solid State Physics ETH Zürich Schweiz 2017–2020 2021-2024	

Highlights

Coherent electro-optomechanics at GHz frequencies with confined microcavity exciton-polaritons

A. S. Kuznetsov, K. Biermann, P. V. Santos

Optomechanical (OM) resonators - systems that couple optical and mechanical degrees of freedom - are of great interest for fundamental studies and applications. One of the present technological challenges is to combine OM with semiconductor-based microcavity (MC) for the cavity quantum electrodynamic (cQED) control of opto-electronic excitations down to single quantum level in nanostructures.

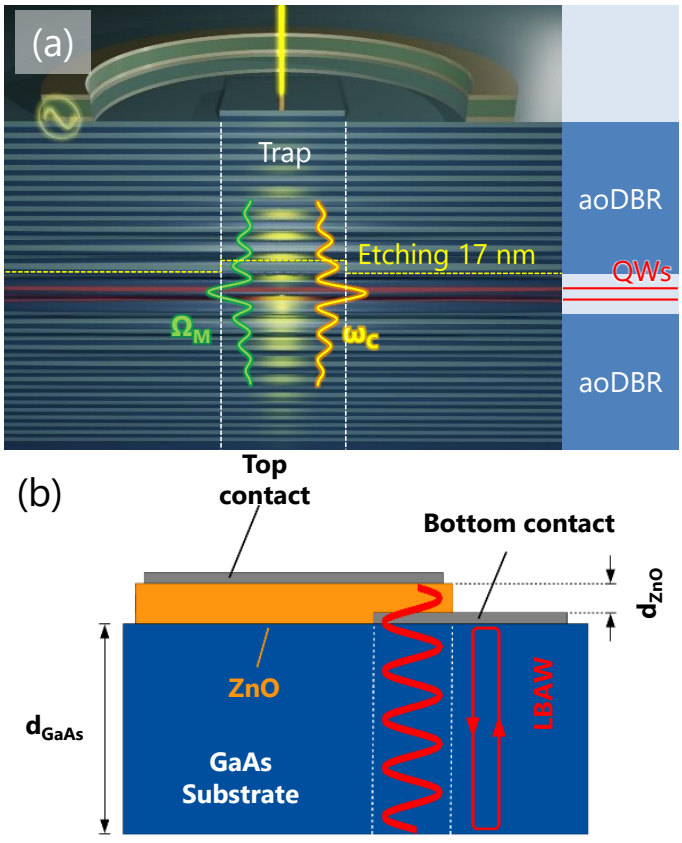

Fig. 1. (a) Cross-section of a hybrid photon-phonon microcavity with intracavity traps for the simultaneous confinement of exciton-polaritons (energy $\hbar\omega_C$) and phonons (of energy $\hbar\Omega_m$). The cavity is formed by two acousto-optic distributed Bragg reflectors (aoDBRs) around a spacer region with embedded quantum wells (QWs). Phonons are electrically injected by an radio-frequency (rf) driven bulk acoustic wave (BAW) resonator (BAWRs) with an aperture for the optical excitation and detection of polaritons. (b) Cross-section of a BAWR on a bare GaAs substrate consisting of a piezoelectric ZnO layer sandwiched between two metal electrodes. The rf voltage applied to the electrodes excites phonons in the form of GHz longitudinal BAWs with center frequency given by $\lambda_{BAW} = v_{BAW}/2d_{ZnO}$, where v_{BAW} is the acoustic velocity and d_{ZnO} is the ZnO thickness.

Emerging applications include the coherent manipulation of quantum states in the nanoscale devices, the interconversion of optical and microwave photons, as well as optical information transfer between on-chip qubits. In this context, the coupling of GHz vibrations (phonons) to solid-state excitations has become relevant for advanced photonic applications, including the emerging fields of quantum communication and computation [K. Fang *et al.*, Nat. Photonics **10**, 489–497 (2016)].

Semiconductor planar MCs (cf. Fig 1(a)) are an ideal system for the controlled manipulation of opto-electronic excitations. These structures efficiently confine photons and quantum well (QW) excitons within a spacer region embedded in-between distributed Bragg reflectors (DBRs). The strong coupling between photons and QW excitons resuts in exciton-polaritons (simply, polaritons), half-light half-matter quasiparticles with long time and spatial coherences. Planar MCs

have been used for many fundamental investigations including, for instance, the control of spontaneous emission and the demonstration of strong light-matter coupling. These studies have also triggered technological advances in the fabrication (in particular, using molecular beam epitaxy, MBE) and applications. The MBE grown (Al,Ga)As MCs are especially attractive owing to their high structural and opto-electronic quality. The development of vertical cavity surface emitting lasers is probably one of the best-known examples.

The MC-based optomechanics is motivated by the fact that an (Al,Ga)As MC confining near-infrared photons in its spacer also confines GHz phonons in the same spatial region [A. Fainstein *et al.*, Phys. Rev. Lett. **110**, 037403 (2013)]. Furthermore, we have recently demonstrated that the coherent phonons with frequencies up to 20 GHz can be electrically generated using piezoelectric bulk acoustic resonators (BAWRs) and injected into these hybrid MCs, thus providing a unique "electric knob" functionality [D.H.O. Machado *et al.*, Phys. Rev. Applied **12**, 044013 (2019)].

In this report, we introduce a novel semiconductor platform bridging cQED and electrically driven OM, based on the coherent coupling of GHz phonons and confined polaritons in structured (Al,Ga)As MC [A.S. Kuznetsov *et al.*, Phys. Rev. X **11**, 021020 (2021)]. The essential ingredients of the platform are: (i) a structured hybrid MC with μm-sized potential traps for the lateral confinement of polariton and phonons and (ii) BAWRs for the injection and detection of monochromatic GHz phonons. The traps can confine long-living phonons and optically pumped exciton-polariton condensates with long coherence time (i.e., exceeding the phonon oscillation period).

Using state-of-the-art MBE, the PDI has developed hybrid MCs embedding intracavity traps (cf. Fig. 1(a)) with high optical and acoustic quality factors (exceeding 10^3 at 10 K). In the (Al,Ga)As material system, the sound and light acoustic impedances ($Z_{sound}/Z_{light} \sim 0.83$) as well as the ratios between sound and light velocities ($c_2/c_1 \sim v_2/v_1 \sim 1:2$) are almost identical. As a consequence of this "double magic coincidence", an (Al,Ga)As MC designed to confine near-infrared photons also efficiently confines GHz phonons. Structured MCs with intracavity polariton traps [cf. Fig. 1(a)] are fabricated by interrupting the MBE growth after the deposition of the cavity spacer embedding the QWs and structuring it by photolithographically defined shallow (typically 10-20 nm) etching. The sample is then reinserted into the MBE chamber and overgrown with the upper distributed Bragg reflector (DBR). The patterning produces µm-sized mesas of different shapes, which maintain their shape during the subsequent overgrowth step. The etching blueshifts the optical and vibrational modes of the MC. The latter is used to create lateral potentials with discrete confined states for both polaritons and phonons [A.S. Kuznetsov *et al.*, Phys. Rev. B **97**, 195309 (2018)].

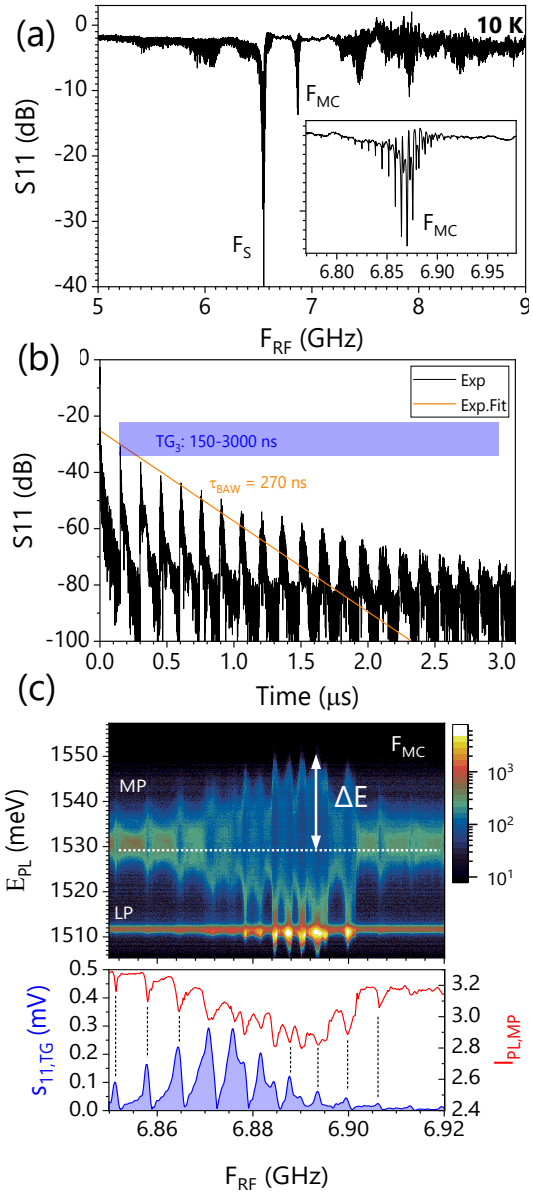

Fig. 2. (a) The rf power reflection coefficient (s_{11}) as a function of frequency of a BAWR at 10 K. The dips in the s_{11} correspond to the excitation of BAWs. The inset shows a zoom of the frequency region of the acoustic MC mode (F_{MC}). (b) Time-resolved acoustic echoes after roundtrips across the sample. The decay yields a phonon lifetime τ_{BAW} = 270 ns. The interference of the reflected waves gives rise to the frequency comb in the inset to (a). (c) (upper panel) The rf-frequency dependence of the polariton spectrum in the F_{MC} range. LP and MP denote the lower and middle polariton levels. (lower panel) The frequency dependencies of time-gated s_{11} corresponding to the time-range TG_3 in (b) and the integrated PL intensity ($I_{PL,MP}$). The MP modulation amplitudes (ΔE) at the comb frequencies exceed 25 meV.

The phonon generation relies on the transduction of a super-high-frequency (SHF, 3 – 30 GHz) radio-frequency (rf) voltage to sound waves achieved in capacitor-like piezoelectric structures – bulk acoustic wave (BAW) resonators (BAWRs) – fabricated on the sample surface (cf. Fig. 1(b)). The BAWR generates (and also detects) LA phonons over a broad range of frequencies, thus enabling rf-spectroscopic studies. Using numerical modelling, we have designed and fabricated BAWRs operating up to 20 GHz in GaAs structures, i.e., at frequencies significantly beyond those achieved with surface acoustic waves (SAWs). Unlike SAWs, which are confined to the sample surface, BAWs propagate towards the bulk and can, therefore, efficiently couple to QWs buried at arbitrary depths (e.g., within the space region of a MC, which is typically a few μm below the surface). Another important feature of SHF BAWs is the very weak and essentially frequency-independent acoustic attenuation at temperatures below $\sim$ 30 K. This leads to exceptionally long BAW propagation lengths, which reach up to a *cm*. Substrates with polished back-surfaces thus become efficient acoustic cavities with enhanced acoustic amplitudes: here, the BAWs experience specular reflection at the surfaces and make several roundtrips through the MC spacer before they attenuate, see Fig. 2(b).

The frequency dependence of the BAWR rf power-reflection coefficient [s_{11}, cf. Fig. 2(a)] allows a precise determination of the acoustic stopband defined by the DBRs as well as of the acoustic modes confined near the surface (frequency F_S) and within the MC spacer (F_{MS}). In the figure, the dips in the spectrum signalize the piezoelectric conversion of the rf signal

applied to the BAWR to acoustic modes. The sharp lines highlighted in the inset of Fig. 2(a) are due to the Fabry-Perot modes that undergo constructive interference upon back-reflection at the top and bottom sample surfaces. They give rise to a comb of resonances with the spacing determined by the total thickness of the sample, as displayed in the inset of Fig. 2(a). This phonon backfeeding to the MC region boosts the effective quality factor ($Q_{a,eff}$) to values $Q_{a,eff} > 10^4$ in the 5–20 GHz range and, hence, to very large $Q_{a,eff} \times frequency$ products exceeding 10^{14}. These high $Q_{a,eff}$ indicate an excellent decoupling of the electrically excited vibrations from the thermal phonon bath even at room temperature. The high $Q_{a,eff}$'s also enables the detection of small (sub MHz) changes in phonon frequency (e.g., such as those expected due to the phonon confinement) as well as time-domain echo spectroscopy with a very large (exceeding 90 dB) dynamical range. Here, the BAWR effectively detects the echoes of a short acoustic pulse after each round trip across the sample, as illustrated in Fig. 2(b). Using this approach, we have been able to observe tens of acoustic echoes and to determine phonon absorption length and lifetime, which at 10 K exceed one mm and 270 ns, respectively.

The piezoelectrically generated strain couples very efficiently to the polariton optical field via radiation pressure as well as to polariton excitonic field via electrostriction (i.e., the modulation of the excitonic levels mediated by the deformation potential interaction). The color map of Fig. 2(c) shows the dependence of the polariton photoluminescence (PL) spectrum on the rf frequency (for fixed a rf power) applied to the BAWR recorded in the configuration of Fig. 1(a) in an unstructured MC (i.e., without traps). The polariton lines become strongly energy-modulated at well-defined rf-frequencies. The frequency dependence of the modulation amplitudes of the PL energy (ΔE) and intensity ($I_{PL,MP}$) follows closely the frequency combs of the s_{11} spectrum, as shown in the lower panel of Fig. 2(c). ΔE reaches a record-high value of 25 meV at some of the resonances: this value is several times larger than the Rabi-coupling energy. Using the GaAs deformation potential, we estimate strain amplitudes in excess of 0.25 %. Even higher strain levels are expected in traps with laterally confined phonon fields.

A comparison of the acoustic modulation of the different polariton lines yields information about the modulation mechanisms. In the sample of Fig. 2(c), the middle polariton (MP) is exciton-like, while the lower polariton (LP) is photon-like. Over the whole rf-frequency range, the energy modulation of the MP is considerably larger than that for the LP, which proves that the modulation is dominated by the exciton-mediated deformation potential interaction.

The modulation studies of Fig. 2 were carried out in the incoherent regime, i.e., when the coherence times of the polariton particles are shorter than the phonon oscillation period. The coherent coupling between the phonons and polaritons is realized at high polariton densities. Polaritons are composite bosons: as a consequence, a polari-

ton gas undergoes a transition to a collective quantum state, Bose-Einstein-like (BEC) condensate, when thermal de Broglie wavelength of the particles exceeds the average inter-particle separation with decreasing temperature and/or increasing particle densities. As for an atomic BEC, the ensemble then collapses into a macroscopic quantum state (a polariton BEC) described by a single, spontaneously built wave function with long spatial extent (up to several tens of μm). The strong inter-particle interactions associated with the excitonic polariton component give rise to pronounced nonlinearities, which have been exploited for the investigations of vorticity and superfluidity as well as for the realization of ultra-fast optical switches. In contrast to atomic BECs, polariton polariton BECs are metastable due to photon losses but can be maintained by continuous optical excitation. In that way, BECs with coherence times (τ_{coh}) substantially longer (up to the ns regime) than the photon lifetime in the MC (tens of ps) can be achieved.

The long temporal coherence of confined phonons and polaritons together with the strong phonon-polariton interactions have important consequences for the optomechanical coupling in arrays of traps. In particular, we have recently demonstrated that coupled confined polariton BEC states in arrays of traps self-oscillate at the phonon frequency when the energy difference between neighboring traps becomes a multiple of the phonon quantum, thus leading to phonon sidebands in the emission spectrum [D.L. Chafatinos *et al.*, Nature Communications **11**, 4552 (2020)]. The same work also shows that the stimulated population of the 20 GHz phonons exceeds 10^5 times the thermal occupation, thus demonstrating an optically driven phonon laser.

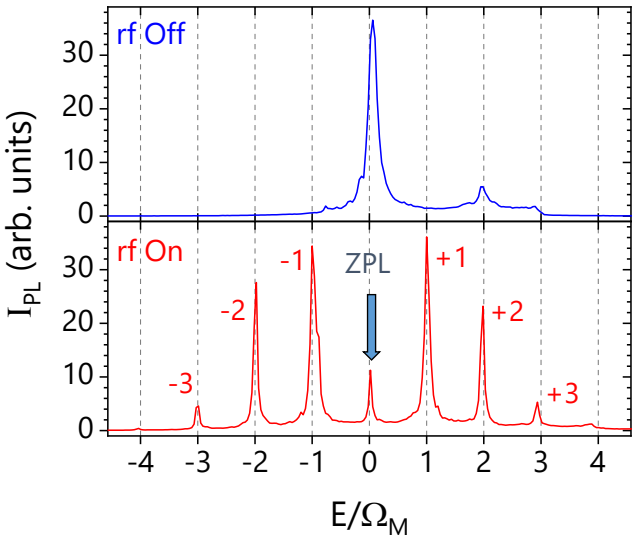

Fig. 3. (upper panel) High-resolution PL spectrum of the ground state of a polariton BEC confined in a $4 \times 4 \mu m^2$ trap in the absence of acoustic excitation with a linewidth $\Gamma_{pol} = 2\pi \times 1.2\ GHz$. (lower panel) Corresponding PL spectrum under a 7 GHz electrically excited phonon field, displaying phonon sidebands. The PL energy (horizontal scale) is specified in units of the phonon quantum $\hbar\Omega_M$ ($\Omega_M = 2\pi \times 7\ GHz$) relative to the zero-phonon line (ZPL).

Finally, we show that the coherent phonon-polariton interaction can also be detected in single traps. Using high resolution spectroscopy, we have established that the coherence time of confined polariton BECs exceeds the photon lifetime by more than two orders of magnitude. Specifically, the black line in upper panel of the Fig. 3 shows a high-resolution spectrum of the ground-state of a polariton BEC confined in a single 4×4 μm^2 trap. The emission is dominated by a single main peak with a spectral linewidth of $\Gamma_{pol} = 2\pi \times 1.5$ GHz, which translates into τ_{coh} = 660 ps. Values τ_{coh} up to 2 ns have been measured. Such a long

coherence time far exceeds the 140 ps oscillation period of phonons with the resonance frequency of f_{BAW} = 7 GHz. The condition $\tau_{coh} > 1/f_{BAW}$ is a prerequisite for the acoustic modulation in the regime of resolved phonon sidebands, which heralds a coherent interaction between phonons and polaritons. The latter regime is demonstrated by the red curve in the lower panel of Fig. 3, which displays the PL spectrum of the same trap when exposed to an electrically excited acoustic comb mode at approximately 7 GHz (i.e., like the ones in Fig. 2(c)). The spectrum reveals well-defined and symmetrical phonon sidebands resulting from the coherent energy modulation. Notably, the zero-phonon line (ZPL) is strongly suppressed under phonon driving, thus demonstrating electro-optomechanically induced transparency.

In conclusion, hybrid MCs confining SHF phonons and near-infrared polaritons establish a powerful platform to bridge the fields of OM and cQED. A key advantage of the platform is the electrical excitation (and detection) of coherent SHF phonons by piezoelectric bulk transducers. In this way, the phonon frequency, amplitudes and injection region within the MC can be precisely controlled. The excited SHF phonons resonantly couple to exciton-polaritons via the deformation potential, resulting in huge polariton energy modulation amplitudes, i.e., exceeding the polariton linewidth by two orders of magnitude even at low polariton densities. As the confined polaritons transition to a BEC state, their coherence time becomes much larger than the phonon oscillation period. This condition allowed us to observe well resolved acoustic sidebands with electrically injected SHF phonons in a single trap as well as phonon lasing in coupled trap systems. The results presented here open a route to the coherent optical control via phonons as well as towards advanced on-chip functionalities including interfacing of near-infrared and microwave excitations.

We acknowledge the financial support by German DFG (grant 359162958).

Van der Waals epitaxy of ferromagnetic Fe_3GeTe_2 films on graphene

J. M. J. Lopes, D. Czubak, E. Zallo, A. I. Figueroa[1], C. Guillemard[2], M. Valvidares[2], J. Rubio-Zuazo[3], J. López-Sánchez[3], S. O. Valenzuela[1], M. Hanke, M. Ramsteiner

Magnetic two-dimensional (2D) materials are promising building blocks for the development of ultra-compact spintronic devices with faster response and low power dissipation. Their study is also expected to open new perspectives on a more versatile modulation of magnetism, beyond what can be achieved in three-dimensional magnetic films. As an example, combining layered magnets with other 2D crystals such as graphene to form van der Waals (vdW) heterostructures offers great potential to tailor magnetism via proximity-induced phenomena.

Among the available 2D magnets, Fe_3GeTe_2 (FGT) is particularly promising due to its outstanding properties. FGT is a ferromagnetic conductor with a robust out-of-plane anisotropy and, most remarkably, highly tunable properties. It has been shown that magnetism in FGT can be tuned via electrostatic gating as well as modulation in its composition, allowing to achieve Curie temperatures (T_C) near 300 K. Besides these possibilities, strain engineering and substitutional doping have been identified as effective routes to tune the magnetic properties of FGTs. Finally, although a native surface oxide forms upon air exposure, degradation in FGT is not as severe as in other 2D magnets such as chromium trihalides, which may facilitate its integration into devices.

The vast majority of the research on FGT and related vdW heterostructures has been performed on micrometer-sized flakes exfoliated from bulk crystals. While such samples allow the exploration of fundamental properties as well as novel device concepts, they are incompatible with standard device fabrication, which usually requires a wafer-scale, uniform form of material. Hence, it is currently of paramount importance to investigate large-scale epitaxy of FGT on different substrates, including other 2D materials to form vdW heterostructures.

In this work, we assess the feasibility of growing FGT on graphene by using molecular beam epitaxy (MBE). Morphological and structural characterization confirmed the realization of large-area, continuous FGT/graphene heterostructure films with high structural quality. Additionally, magnetism in the samples was probed macro- and microscopically, revealing a ferromagnetic behavior for the FGT films that is similar to state-of-the art exfoliated flakes. These results are highly relevant for further research on wafer scale growth of vdW heterostructures combining FGT with other 2D crystals for the realization of multifunctional, atomically thin devices.

FGT was synthesized by MBE using elemental Fe, Ge, and Te evaporated from

[1]Catalan Institute of Nanoscience and Nanotechnology (ICN2), Barcelona, Spain.
[2]ALBA Synchrotron Light Source, Barcelona, Spain.
[3]Spanish CRG BM25-SpLine at The ESRF—The European Synchrotron, Grenoble, France.

Knudsen cells. Continuous films with thicknesses around 10 and 20 nm [(i.e., from 12 to 25 FGT quintuple layers (QL); 1 QL corresponds to approximately 0.8 nm formed by sequential Te/Fe/FeGe/Fe/Te slabs)] were obtained using growth times of 1 and 2 h, respectively. As substrates, $1\times1\,cm^2$-large pieces of epitaxial graphene on 4H-SiC(0001) were utilized. They were fabricated via SiC surface graphitization at high temperatures in an Ar atmosphere, following a well-established protocol [M. H. Oliveira, Jr., *et al.*, Appl. Phys. Lett. **99**, 111901 (2011)]. FGT films were also synthesized on $1\times1\,cm^2$ $Al_2O_3(0001)$ pieces using the same conditions for comparison. For all growth experiments, a substrate temperature of 300 °C was employed. Finally, the FGT films were capped in some cases *in situ* with about 5-nm-thick Te layer deposited after sample cooling to room temperature. This procedure was adopted in order to reduce FGT surface oxidation upon prolonged air exposure, which could hinder the successful use of surface-sensitive techniques such as x-ray absorption spectroscopy (XAS), x-ray magnetic circular dichroism (XMCD), and grazing incidence x-ray diffraction (GID) [see results below].

Figure 1(a) shows an atomic force microscopy (AFM) image of a 10-nm-thick FGT film, which reveals the continuous coverage over the graphene/SiC surface terraces. Discontinuities (holes) in the film are observed mostly close to step edges (indicated by red arrows), resulting in relatively small areas with exposed graphene. The appearance of such morphological irregularities is probably related to an inability of FGT to grow—under the employed synthesis conditions—on the bi- to few-layer-thick graphene ribbons and patches located on step edge regions [L. A. Galves *et al.*, Carbon **115**, 162 (2017)]. They exhibit a much lower chemical reactivity in comparison to the one of monolayer graphene covering surface terraces. This variation is known to af-

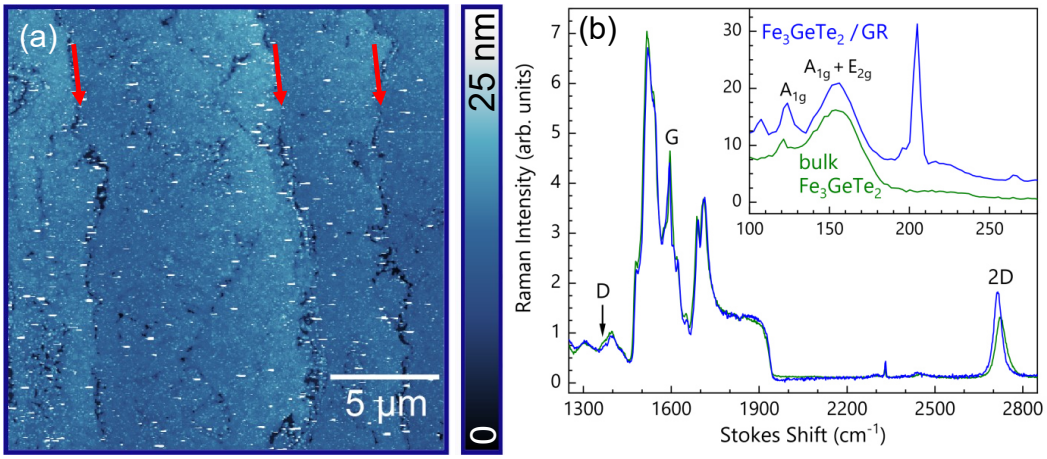

Fig. 1. (a) AFM image of a 10-nm-thick FGT film grown on graphene/SiC(0001). The red arrows indicate the position of steps on the graphene/SiC(0001) surface. (b) Raman spectra for excitation at a wavelength of 473 nm showing the graphene and SiC components for samples with (blue spectrum) and without (green spectrum) a 20-nm-thick FGT film on top. The inset depicts the A_{1g} and A_{1g}+E_{2g} Raman components associated with the FGT film (blue spectrum). For comparison, the Raman spectrum collected from a commercially available bulk FGT crystal is also plotted (green spectrum).

fect the overgrowth of 2D materials [M. Heilmann *et al.*, ACS Appl. Mater. Interfaces **12**, 8897 (2020)]. Further optimization of the FGT growth parameters is anticipated to mitigate this problem. The root-mean-square (RMS) roughness of the FGT film was measured to be about 1 nm in $1\times1\,\mathrm{cm}^2$ on a surface terrace, which is higher than the one measured on graphene surfaces (RMS $\approx$ 0.2 nm). Note that the AFM images depicted here were acquired from non-capped FGT films exposed to air for several days. Thus, natural oxidation of the topmost few layers of the FGT film is expected to affect the surface roughness [D. Kim *et al.*, Nanotechnology **30**, 245701 (2019)].

The results of Raman spectroscopy shown in Fig. 1(b) confirmed that the graphene did not suffer structural changes due to the FGT synthesis. Besides the SiC background signal, the graphene-related 2D and G peaks remain mostly unaltered. The intensity of the defect-related D peak does not increase after growth. This confirms the structural integrity of graphene and indicates that no rehybridization takes place in graphene, e.g., due to the formation of covalent bonds with FGT. The Raman measurements also confirmed the formation of FGT. The inset in Fig. 1(b) shows two components appearing at about 120 and 155 cm^{-1}, which are associated with the A_{1g} and the superposition of the A_{1g}+E_{2g} phonon modes in FGT, respectively. The peak located around 205 cm^{-1} originates from SiC.

Figures 2(a) and 2(b) present reflection high energy electron diffraction (RHEED) patterns obtained before and after FGT growth, respectively. For the latter, the narrow streaks indicate epitaxial growth of a 2D film with a smooth surface. The shift in their location with respect to the pattern obtained for graphene/SiC reveals the evolution to a larger in-plane lattice constant as expected for FGT. Further information on the structure of FGT/graphene heterostacks was obtained by GID. Figure 2(c) shows an in-plane reciprocal space map of a Te-capped, 10-nm-thick FGT film on graphene/SiC, in which the color-coded scattered intensity in reciprocal space is plotted as a function of reciprocal lattice units (rlu), referring to the hexagonal lattice of SiC(0001). Note that we use the four-component vector notation for hexagonal symmetry, i.e., (hklm) = (hk.m) = (hk-(h+k)m). There are highly localized substrate reflections, namely the SiC$(2\bar{1}.0)$ one and its higher orders. A line scan crossing the SiC$(2\bar{1}.0)$ reflection is superimposed to the map. We have also drawn different radii corresponding to net plane distances of graphene, G(10.0) and G(11.0), and FGT, i.e., the FGT(n0.0) with n = [2..4] and FGT(nn.0) with [n = 1..3]. Based on the three most intense contributions from FGT, i.e., (11.0), (30.0), and (22.0), one can deduce an average in-plane lattice parameter for FGT of 4.011 Å, which indicates a tensile strain of about 0.5 % [taking as a reference value $d_{FGT} = 3.991$ Å for bulk crystals from H.-J. Deiseroth *et al.*, Eur. J. Inorg. Chem. 1561 (2006)]. The observed strain might be related to structural deformation in the FGT layers due to bending around surface irregularities (e.g., graphene wrinkles and SiC surface steps).

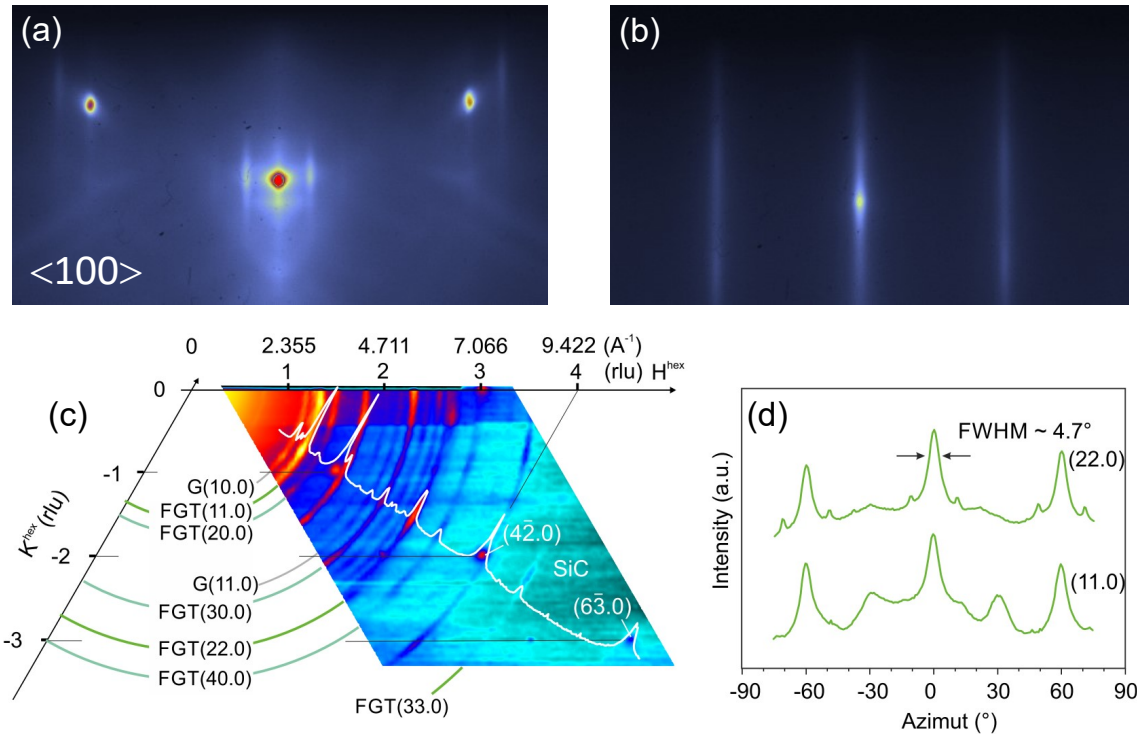

Fig. 2. *In situ* RHEED patterns taken perpendicular to the SiC⟨100⟩ direction, (a) before and (b) after FGT growth. (c) GID in-plane reciprocal space map of a Te-capped, 10-nm-thick FGT on a graphene/SiC(0001) sample. The corresponding absolute length (in units of $Å^{-1}$) of the scattering vector is additionally provided along the H^{hex} axis. The white profile shows a linear scan along the SiC$[2\bar{1}.0]$ direction. (d) Two azimuthal intensity profiles intersecting the maxima caused by the FGT lattice.

Following the intensity distribution along the FGT arcs, one recognizes a preferential azimuthal orientation of the FGT layer in a way that the FGT[11.0] net planes are parallel to the SiC[11.0] ones. Two of those angular profiles crossing the FGT(11.0) and (22.0) reflections are plotted in Fig. 2(d). They exhibit a full width at half maximum (FWHM) of about 4.7°, indicating a FGT lattice well aligned to the substrate. Additionally, there are weaker maxima 30° off revealing a smaller fraction of the FGT layer, which appears twinned to the major variant. Moreover, low-intensity maxima symmetric to the FGT(22.0) one at 0° and ±60° are also observed, which are about 10° off the $[2\bar{1}.0]$ direction. These highly symmetric sub-features are most probably due to a coincidence lattice between the FGT and the underlying graphene and/or SiC.

The magnetic and electrical characteristics of FGT/graphene heterostacks were investigated by transverse resistance (R_{xy}) measurements. In ferromagnetic materials, R_{xy} under the application of an out-of-plane magnetic field H is given by the superposition of the ordinary (OHE) and anomalous (AHE) Hall effects. Whereas the OHE contains information about the electrical characteristics, the AHE can be utilized to investigate the magnetic order. Figure 3(a) displays R_{xy} for a 20-nm-thick FGT film on graphene/SiC measured at different temperatures during subsequent downward and upward sweeps of an external magnetic field. The AHE is clearly detected as a square-shape hysteresis loop superimposed on an OHE contribution with a linear de-

pendence on the external field. The occurrence of the AHE reflects the ferromagnetic order in FGT, with the observed remanence providing evidence for a perpendicular magnetic anisotropy. The temperature dependences of the coercivity (H_c) and ΔR_{AHE} are shown in Fig. 3(b) [ΔR_{AHE} is defined as the value of R_{AHE} at magnetization saturation]. Both quantities decrease with increasing temperature, and their extrapolation to zero indicates a T_C of about 220 K, in agreement with values reported for FGT flakes.

From the slope of the OHE contribution to the Hall curves shown in Fig. 3(a), a low-temperature carrier density of $6.8\times10^{13}\,\mathrm{cm}^{-2}$ is extracted which, in principle, can be ascribed to *n*-type doped graphene on SiC(0001). In contrast, FGT films are expected to exhibit a hole-like transport character with an opposite R_{OHE} slope of much lower absolute value corresponding to a carrier density of approximately $2\times10^{15}\,\mathrm{cm}^{-2}$, as determined for FGT films grown on Al_2O_3(0001) (not shown). The sheet resistivity of the FGT/graphene heterostructure ($150\,\Omega\ \mathrm{sq}^{-1}$) is found to be almost one order of magnitude smaller than the one commonly observed for our graphene films (about $2\,\mathrm{k}\Omega\ \mathrm{sq}^{-1}$). These findings are explained by considering parallel conduction through two transport channels for the analysis of the OHE. In this case, the sign as well as the absolute value of the R_{OHE} slope depend on the relative conductivities of the FGT and graphene films. Therefore, they generally do not reflect the carrier type and density of only one of the two transport channels. Finally, measurements performed utilizing magnetic fields with magnitudes above 4 T reveal that R_{xy} exhibits plateaus which are associated with the manifestation of the quantum Hall effect (QHE) in graphene. This underlines the high quality and carrier mobility of the graphene film underneath FGT over the large-area van der Pauw (vdP) structure.

XMCD/XAS results obtained for a Te-capped, 20-nm-thick FGT film are shown in Fig. 4. The magnetic hysteresis loop in Fig. 4(a) was recorded at the base temperature of 3 K with the beam energy fixed at the maximum of the Fe L_3 XMCD sig-

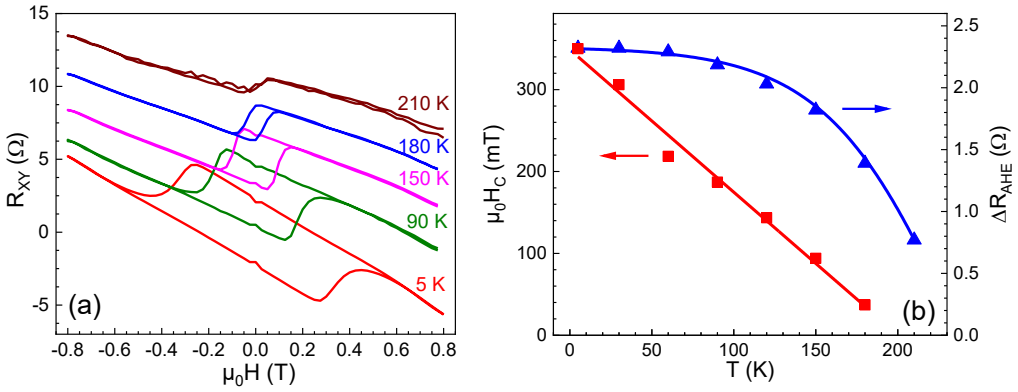

Fig. 3. (a) Transverse resistance R_{xy} of a $1\times1\,\mathrm{cm}^2$ FGT/graphene vdP structure during downward and upward magnetic field sweeps at different temperatures. The R_{xy} curves for temperatures above 5 K are upshifted by $2.5\,\Omega$ for clarity. (b) Coercive field H_c and saturation resistance ΔR_{AHE} extracted from the AHE contribution as a function of temperature. The solid lines are guides to the eye.

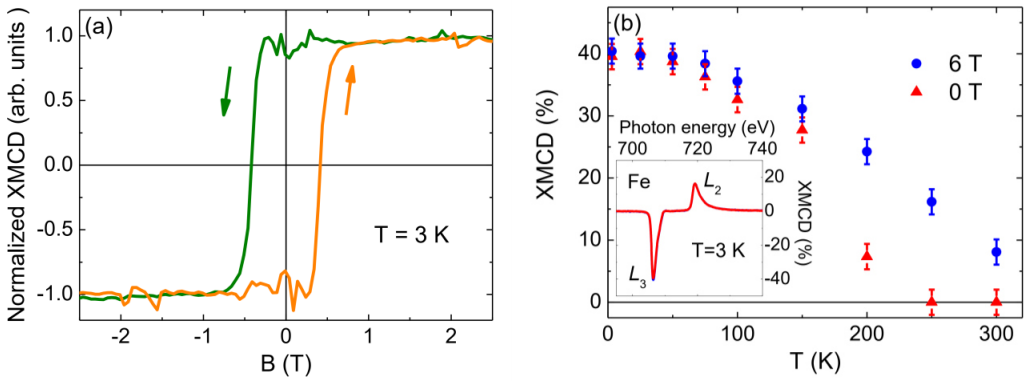

Fig. 4. (a) Hysteresis loop recorded at the Fe L_3 edge for a Te-capped, 20-nm-thick FGT film on graphene/SiC(0001) at 3 K. The XMCD signal is normalized to its value in saturation. (b) Temperature dependence of the Fe L_3 XMCD maximum in saturation (6 T, blue circles) and remanence (red triangles). Inset: XMCD signal recorded at 3 K under an out-of-plane magnetic field of 6 T (blue) and at remanence (red).

nal (706.4 eV) [see inset in Fig. 4(b)]. The signal is normalized to an energy point at the pre-edge region (703 eV), measured on the fly with a magnetic field (B) ramp of 1.5 T min^{-1} at high B (from $\pm$6 to $\pm$2 T) and of 1.0 T min^{-1} at low B (from $\pm$2 to $\mp$2 T). In accordance with the magnetotransport results, the square shape of the loop reveals the strong out-of-plane ferromagnetic character of the Fe atoms in the FGT film. The temperature dependence of the maximum of the Fe L_3 signal in saturation (6 T) and remanence (0 T) are plotted in Fig. 4(b). The remanent magnetization extrapolates to zero at about 220 K, which agrees closely with the value of T_C found by transport measurements. The XMCD signal at 6 T persists at room temperature, demonstrating a strong paramagnetic response, even though the long-range ferromagnetic order has already vanished. Application of the magneto-optical sum rules for XAS and XMCD [B. T. Thole *et al.*, Phys. Rev. Lett. **68**, 1943 (1992)] allowed us to extract the orbital, spin, and total magnetic moments (m_{orb}, m_{spin}, and m_{total}) of Fe 3d electrons in the ground state. From the experimental Fe $L_{2,3}$ edges in the spectra at 3 K and 6 T, we obtain $m_{\mathrm{orb}} = (0.047 \pm 0.004)\,\mu_{\mathrm{B}}$/Fe, $m_{\mathrm{spin}} = (1.13 \pm 0.09)\,\mu_{\mathrm{B}}$/Fe, and $m_{total} = (1.18 \pm 0.10)\,\mu_{\mathrm{B}}$/Fe. The orbital-to-spin moment ratio is 0.042 ± 0.008, which is comparable to that of elemental Fe (0.043) and somewhat larger than what is reported for FGT single crystals (0.03).

In summary, vdW epitaxy of FGT on graphene was studied via MBE. The realization of large-area FGT/graphene heterostructures with high structural and interface quality could be demonstrated. Magneto-transport and XMCD/XAS investigations revealed a robust perpendicular magnetic anisotropy in FGT and the observation of plateaus associated with the QHE effect in graphene. These results are relevant for further research on wafer-scale growth of vdW heterostructures with multifunctional properties. By combining FGT with other 2D crystals including transition metal dichalcogenides and hexagonal BN, we envision the realization of spintronic devices with dimensions and performance not achievable with conventional bulk materials.

Brief Reports

Lattice parameters of $Sc_xAl_{1-x}N$ layers grown on GaN(0001) by plasma-assisted molecular beam epitaxy

D. V. Dinh, J. Lähnemann, L. Geelhaar, O. Brandt

(Sc,Al)N ternary alloys have attracted considerable interest for surface acoustic wave devices due to their outstanding piezoelectric properties [M. Akiyama *et al.*, Adv. Mater. **21**, 593 (2009)]. Additionally, (Sc,Al)N layers grown on GaN templates have been considered for high-electron-mobility transistors with unprecedented electron sheet density [M. T. Hardy *et al.*, Appl. Phys. Lett. **110**, 162104 (2017)].

(Sc,Al)N layers are fabricated most frequently by sputtering, but the resulting material generally exhibits a very low crystallinity. Recently, (Sc,Al)N layers of higher crystallinity have been synthesized by plasma-assisted molecular beam epitaxy (PAMBE). Despite the improved structural properties of these layers, the existing studies do not agree on the dependence of both the in-plane a and out-of-plane c lattice constants on the Sc content, for which widely different values have been reported. However, the c/a ratio of (Sc,Al)N is predicted to basically determine its piezoelectric coefficients [H. Momida *et al.*, Appl. Phys. Express **11**, 041201 (2018)]. Hence, an accurate knowledge of the lattice constants of (Sc,Al)N is essential not only to synthesize lattice-matched layers on GaN, but also to understand the elastic and piezoelectric properties of these layers.

In this study, we investigate the crystalline properties and determine the lattice parameters of $Sc_xAl_{1-x}N$ layers grown on undoped GaN(0001)/sapphire templates using PAMBE. The composition of the layers is varied by changing the Sc flux while keeping the Al flux constant. Likewise, we keep the growth temperature constant at 700 °C. The Sc content x of the layers is determined independently by two analytical techniques, namely, x-ray photoelectron spectroscopy (XPS) and electron dispersive x-ray spectroscopy (EDX). The lattice constants of the layers are measured using a triple-axis high-resolution x-ray diffraction (XRD) system equipped with a Ge(220) hybrid monochromator and a Ge(220) analyzer. We investigate layers with a thickness of 100–120 nm to facilitate the detection of asymmetric XRD peaks allowing us an accurate determination of both the out-of-plane and in-plane lattice constants.

Figure 1(a) shows the dependence of the Sc content in the solid phase, as measured by XPS and EDX, on the corresponding beam flux ratio. A linear relation is observed as expected in the absence of desorption of the group III elements. Symmetric ω-2θ XRD scans, as shown in Fig. 1(b), reveal that layers with high structural perfection are obtained for $x \approx 0.1$. The distinct thickness fringes allow us to determine the layer thickness of (105 ± 1) nm. The XRD peak of layers with both lower and higher Sc content broadens notably. For the highest Sc content, the appearance of an additional peak gives evidence of phase separation. This phase separation is due to the fact that

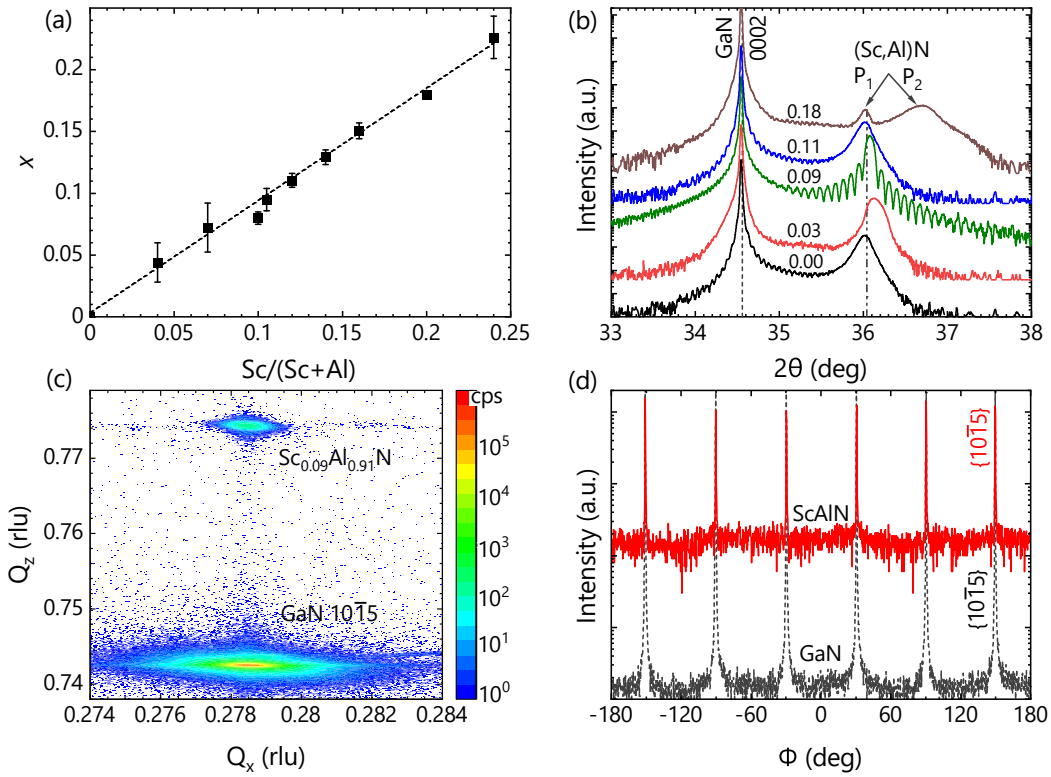

Fig. 1. (a) Sc content of the $Sc_xAl_{1-x}N$ layers under investigation. The data points represent the average of the values determined by XPS and EDX. (b) Symmetric ω-2θ XRD scans of $Sc_xAl_{1-x}N$ layers on GaN(0001). The Sc content is indicated in the figure. The dashed and dash-dotted lines indicate the 0002 2θ positions of relaxed GaN and AlN, respectively. (c) RSM of the $Sc_{0.09}Al_{0.91}N$ layer around the asymmetric GaN $10\bar{1}5$ diffraction peak. (d) Azimuthal ϕ scans of the $Sc_{0.09}Al_{0.91}N$ and GaN $10\bar{1}5$ peaks.

AlN crystallizes in the wurtzite structure, while ScN exhibits the rock-salt structure. Therefore, at a certain value of x, a transition from the wurtzite to the rock-salt structure will occur [C. Constantin *et al.*, Phys. Rev. B **70**, 193309 (2004)].

Reciprocal space maps (RSM) around the asymmetric GaN $10\bar{1}5$ diffraction peak are measured to obtain further insight into the crystal structure of the (Sc,Al)N layers and to get access to their in-plane lattice constants. Figure 1(c) shows an RSM of the 105-nm-thick $Sc_{0.09}Al_{0.91}N$/GaN layer. Besides the GaN $10\bar{1}5$ peak, only the (Sc,Al)N $10\bar{1}5$ peak is observed, indicating that this layer also has a hexagonal wurtzite crystal structure with the (0001) surface orientation. This conclusion is confirmed by azimuthal scans of the $Sc_{0.09}Al_{0.91}N$ $10\bar{1}5$ and GaN $10\bar{1}5$ peaks as shown in Fig. 1(d). Additionally, the RSM demonstrates that the $Sc_{0.09}Al_{0.91}N$ layer is pseudomorphic to GaN.

For improved accuracy, the a and c lattice constants of the (Sc,Al)N layers are calculated from the angular positions of the symmetric 0002 and asymmetric $10\bar{1}5$ XRD peaks. The measured lattice constants of $Sc_xAl_{1-x}N$ layers previously reported in the literature and of the layers studied here are shown as a function of x in Fig. 2. It should be noted that due to the phase separation, it is impossible to measure the a lattice constant for the samples with $x > 0.15$. The value of a has been found to increase linearly ($a = 3.116 + 0.765\,x$) with increasing x [Fig. 2(a)], resulting in lattice matching of GaN

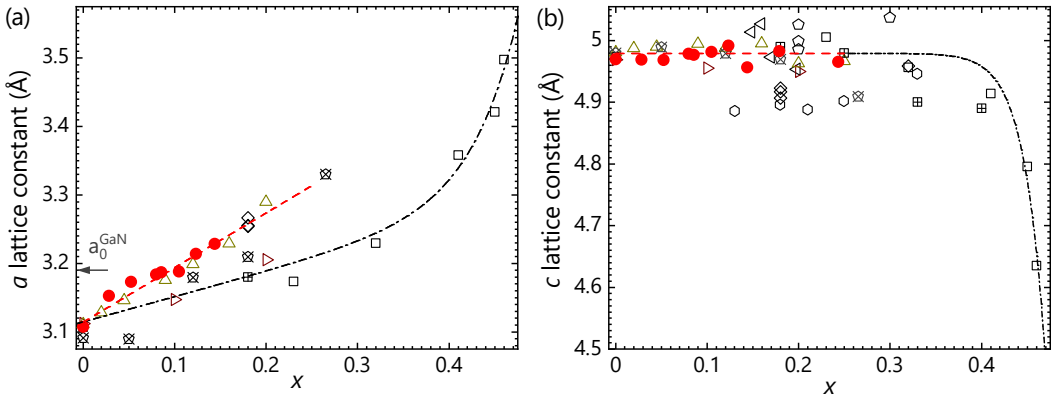

Fig. 2. (a) In-plane (a) and (b) out-of-plane (c) lattice constants as a function of x of the $Sc_xAl_{1-x}N$/GaN layers studied in this work (•). Lattice constants of (Sc,Al)N from previous work are also shown for comparison. Lines in both figures are guides to the eye. The arrow in (a) indicates the relaxed in-plane lattice constant (a_0^{GaN}) of GaN.

for $x = 0.095$. In contrast, the value of c remains almost constant [Fig. 2(b)]. This anisotropic expansion was observed before for (Sc,Ga)N, and attributed to local distortions of the wurtzite structure due to the existence of a layered hexagonal phase of ScN [C. Constantin, *op. cit.*].

The c lattice constants obtained for the (Sc,Al)N samples studied here are close to the values previously reported in the literature for $x < 0.15$. However, for $x > 0.15$, the values exhibit notable deviations. This fact is presumably related to the transition from the wurtzite to rock-salt structure as discussed above.

The crystallinity of the $Sc_xAl_{1-x}N$ layers is investigated by measuring 0002 and $10\bar{1}2$ x-ray rocking curves in the quasi-symmetric skew-geometry. Figure 3(a) shows the values for the full-width at half-maximum (FWHM) of these diffraction profiles as a function of x and, equivalently, the lattice mismatch to GaN(0001). The FWHM values of both peaks decrease with increasing x, reach minimum values at $x \approx 0.1$, and then increase for higher x. This trend matches exactly with the change of lattice mismatch between (Sc,Al)N and GaN. For the $Sc_{0.09}Al_{0.91}N$ layers, FWHM values of 240″ and 270–370″ are obtained for the 0002 and $10\bar{1}2$ rocking curves, respectively. These values are comparable to those of the GaN templates, indicating

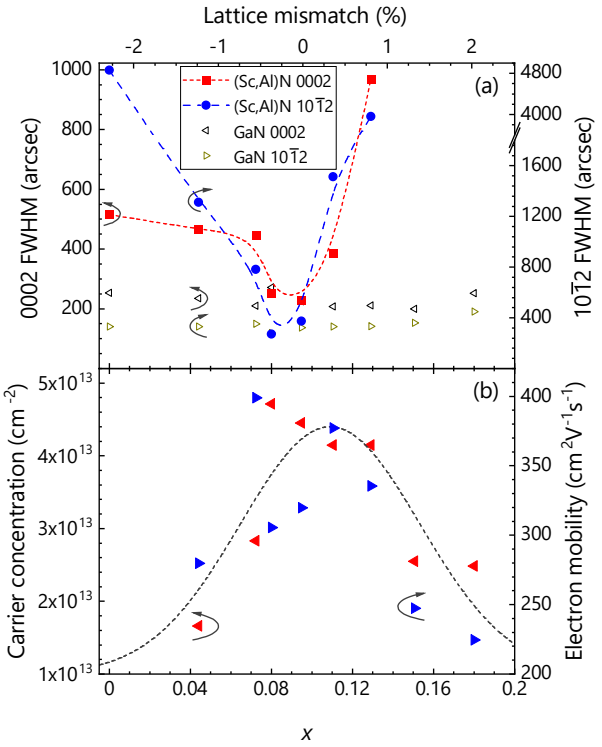

Fig. 3. (a) FWHM of the 0002 and $10\bar{1}2$ x-ray rocking curves and (b) 2DEG sheet density and mobility of the $Sc_xAl_{1-x}N$/GaN layers plotted as a function of x. The lines are a guide to the eye.

the high crystalline quality of these layers. Note that this is the first time that asymmetric rocking curves could be measured for (Sc,Al)N.

Finally, it is of interest to examine the electrical properties of the (Sc,Al)N/GaN structures, which we do here by room-temperature Hall effect measurements. The results are displayed in Fig. 3(b), and reveal a maximum electron sheet density and mobility at $x \approx 0.1$, i. e., for lattice-matched films. For low Sc concentrations as in this work, the (Sc,Al)N layers remain insulating, similar to pure AlN, and the rather high electron sheet densities measured can only originate from two sources: the intentionally undoped GaN template and the two-dimensional electron gas (2DEG) induced by the difference in electrical polarisation between GaN and (Sc,Al)N. For the former, separate Hall measurements yield sheet densities of $2 \times 10^{13}\,\mathrm{cm}^{-2}$ (corresponding to a volume density of $5 \times 10^{16}\,\mathrm{cm}^{-3}$) and a mobility of $200\,\mathrm{cm}^2\mathrm{V}^{-1}\mathrm{s}^{-1}$, values very close to those obtained for Sc contents far from lattice matching. Evidently, the increase in both sheet density and mobility close to lattice matching is due to the formation of a 2DEG. Analyzing the data in the framework of a two-conduction-band model [D. C. Look *et al.*, J. Appl. Phys. **74**, 311 (1993)], we obtain values of $4.5 \times 10^{13}\,\mathrm{cm}^{-2}$ and $375\,\mathrm{cm}^2\mathrm{V}^{-1}\mathrm{s}^{-1}$ for the sheet density and mobility of the 2DEG at $x = 0.1$, values close to actual (Sc,Al)N/GaN high-electron-mobility transistor structures reported by other groups [M. T. Hardy *et al.*, *op. cit.*]. Away from lattice matching, the 2DEG rapidly degrades presumably due to the formation of dislocations at the hetero-interface.

Concluding, we have accurately determined the composition and lattice constants of (Sc,Al)N layers on GaN(0001) by independent experimental techniques. A lattice match to GaN is established at a Sc content of about 0.1. (Sc,Al)N layers with this composition exhibit a very high structural perfection (essentially limited by that of the template) and give rise to a 2DEG at the (Sc,Al)N/GaN interface with a high sheet density.

Adsorption-controlled $LaInO_3$ growth by plasma-assisted molecular beam epitaxy

G. Hoffmann, D. Klimm[1], and O. Bierwagen

The family of complex oxides comprises dielectric, semiconducting, superconducting, ferromagnetic, and ferroelectric materials. Their common, perovskite, crystal structure provides the basis for combining these oxides and their respective properties epitaxially to form (multi)functional heterostructures. Among these oxides, the wide-bandgap semiconductor $BaSnO_3$ (BSO) has the highest room-temperature electron mobility—up to 320 cm^2/Vs for bulk material [H. J. Kim *et al.*, Appl. Phys. Express **5**, 061102 (2012)] and 183 cm^2/Vs for thin films [H. Paik *et al.*, APL Mater. **5**, 116107 (2017)] have been reported. BSO has a band gap of $E_g \approx 3.1$ eV. Interfacing the non-polar oxide BSO with the wider-band gap ($E_g \approx 5.0$ eV) polar oxide $LaInO_3$ (LIO), has been predicted to induce and confine a two-dimensional electron gas (2DEG) at the interface through polarization doping [K. Krishnaswamy *et al.*, Appl. Phys. Lett. **108**, 083501 (2016)]. Different flavors of molecular beam epitaxy (MBE) have demonstrated the adsorption-controlled growth of BSO thin films with the highest quality and electron mobility [S. Raghavan *et al.*, APL Mater. **4**, 016106 (2016), A. Prakash *et al.*, J. Vac. Sci. Technol A **33**, 060608 (2015)], whereas the MBE growth of LIO has not been reported to date.

Here, we demonstrate the adsorption-controlled growth of LIO thin films by plasma-assisted MBE using In and La effusion cells and a controlled flow of oxygen injected into the plasma source run at a RF power of 200 W. In order to sustain the plasma even at low O_2 fluxes in the range of 0.06–0.14 sccm we provided an additional 0.1–0.2 sccm Ar flux to the plasma source using a separate mass flow controller. A line-of-sight quadrupole mass spectrometer allows us to analyze the flux desorbing from the substrate.

Our LIO films are grown on orthorhombic (110)-oriented $DyScO_3$ (DSO) substrates. As shown in Fig. 1(a), LIO also possesses an orthorhombic unit cell with lattice parameters $a = 0.595$ nm, $b = 0.571$ nm, and $c = 0.824$ nm [K. Krishnaswamy *et al.*, Appl. Phys. Lett. **108**, 083501 (2016)]. The In atoms are surrounded by oxygen atoms in a tilted octahedral arrangement. Both, DSO and LIO form a coinciding (100)-oriented pseudocubic unit cell in their orthorhombic (110)-orientation [see Fig. 1(b)]. The resulting lattice mismatch of these pseudocubic cells is in the range of 4.5–5.5% depending on the orientation of the a, b, and c directions between LIO and DSO. The pseudocubic cell of the LIO results in an alternating stacking of polar LaO (+1) and InO_2 (-1) planes due to the charge transfer of 0.5 electrons per unit cell from the LaO to the InO_2 below and above [see Fig. 1(c)]. At the LIO/BSO interface, a net charge of 0.5 electrons per

[1]Leibniz-Institut für Kristallzüchtung im Forschungsverbund Berlin e.V., Max-Born-Straße 2 D-12489 Berlin

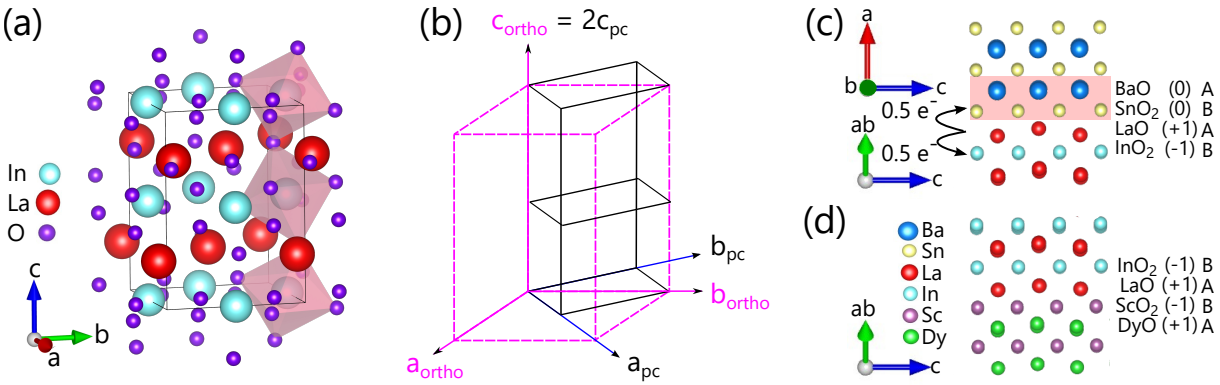

Fig. 1. (a) Orthorhombic LIO unit cell with three octahedra formed by the oxygen atoms highlighted in red. (b) Sketch of the relationship of the orthorhombic (pink) and related $1 \times 1 \times 2$ pseudocubic (black) LIO unit cell. (c) Cation stacking at the LIO/BSO interface. Due to the polar discontinuity (indicated by the bracketed numbers) charge transfer from the LaO to the SnO_2 layer provides electrons to a 2DEG (red shaded area). (d) Schematic cation stacking for LIO on DSO according to our growth approach. The lattice mismatch between DSO and LIO along the *ab*-plane and *c*-plane is 5.14% and 4.56%, respectively.

unit cell transfered to the neutral SnO_2 layer is predicted to form a 2DEG in the BSO, illustrated by the red shaded area, that is partially confined by the conduction band offset between LIO and BSO [K. Krishnaswamy *et al.*, Appl. Phys. Lett. **108**, 083501 (2016)]. The low lattice mismatch of 1.1 to 1.4% (depending on the orientation of the LIO orthorhombic unit cell) between BSO(100) and LIO(110) promises a high-quality interface for the epitaxial realization of this 2DEG.

Prior to growth the DSO substrates were annealed at 1050 °C in oxygen at atmospheric pressure in a tube furnace for 6 hours. This treatment provides a stable, ScO_2-terminated surface [see Fig. 1(d)] that enables LIO growth with controlled stacking sequence and regular step-terrace structure related to the unintentional substrate off-cut.

Possessing two different cations, a common challenge for the MBE-growth of complex oxides is the realization of the proper cation stoichiometry of 1:1. As long as one cation (or its suboxide) can desorb from the film surface at growth temperature, the film stoichiometry can self-adjust as adsorption of this cation is controlled by the flux of the other cation, the O-flux, and the thermodynamically stable film composition. This "adsorption-controlled" approach has been used by others and ourselves to grow $BaSnO_3$ [H. Paik *et al.*, APL Mater. **5**, 116107 (2017), A. Prakash *et al.* J. Mater. Chem. C **5**, 5730 (2017)]. In the case of LIO, the low vapor pressures of La (and its suboxide LaO) result in a sticking coefficient of unity at the growth temperatures accessible to us, whereas In (and its suboxide In_2O) possess a high-enough vapor pressure to grant desorption from the growth surface. To delineate the growth conditions that provide an LIO film free of any secondary solid La_2O_3 or In_2O_3 phases, an Ellingham diagram was computed using the FactSage™ thermochemical software package. This diagram shows the formed solid phases as function of temperature and oxygen partial pressure. For the calculation of the LIO phase, the heat capacity c_p and formation enthalpy ΔH

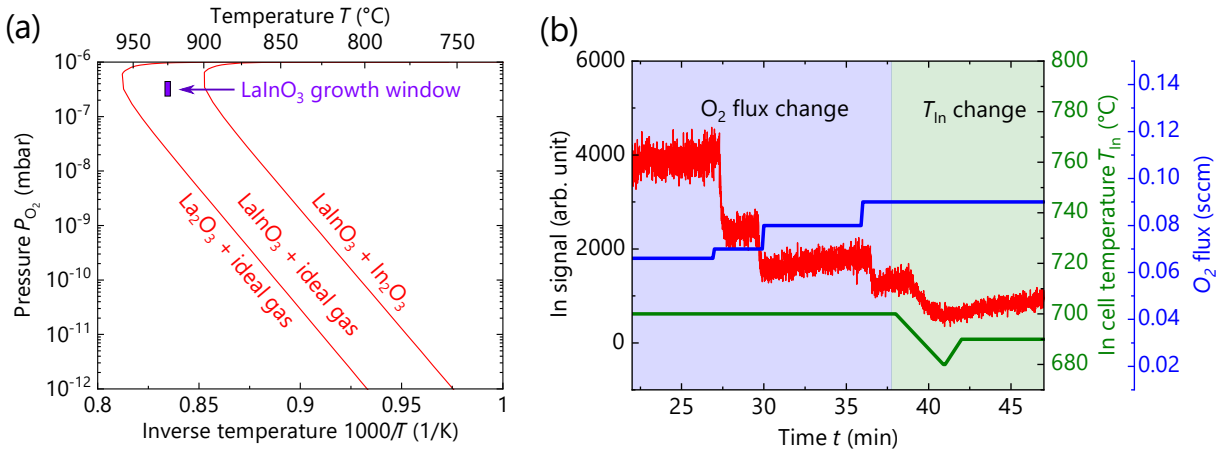

Fig. 2. (a) Ellingham diagram for LIO growth showing the experimentally determined growth window (purple square) as well as theoretically expected solid equilibrium phases LIO + In_2O_3, LIO, and La_2O_3 (red lines). The ideal gas mainly consists of the volatile In_2O. (b) Measured In desorption from LIO growth front (indicative of In_2O desorption) for varying O_2 flux (blue shaded area) and varying In cell temperature (green shaded area).

of bulk LIO were experimentally measured and added to the database. The Ellingham diagram shown in Fig. 2(a) was calculated in an In excess and for a total pressure of 10^{-6} mbar to match our MBE conditions in terms of excess In flux and O_2 background pressure. The pure LIO solid phase is delineated by two lines towards lower (higher) temperatures or higher (lower) oxygen pressures that lead to the formation of secondary In_2O_3 (La_2O_3) phases. The ideal gas consists of In_2O (desorbing In-species) and O_2.

Experimentally, we found an appropriate growth window at a fixed substrate temperature of T_{sub} = 925 °C in the O_2 flux range of 0.1–0.12 sccm which corresponds to oxygen partial pressures of $2.88–3.78\times10^{-7}$ Torr measured by quadrupole mass spectrometry. These growth conditions indicated by the purple square in Fig. 2(a) are within the theoretically predicted growth window if we disregard the effect of the plasma. The La flux determined the film growth rate (fixed at 1 nm/min) while In is provided in a slight excess. Fig. 2(b) shows the desorbing In_2O flux measured as In fragment by line-of-sight quadrupole mass spectrometry. In the blue shaded region, the desorbing In flux decreases with increasing O_2 flux indicating adsorption control by the O_2 flux as more In is incorporated into the film. In the green shaded area, the In signal follows the In cell temperature since less In is being desorbed when less In is provided.

After growth, the samples were investigated using atomic force microscopy (AFM) and x-ray diffraction (XRD). Fig. 3(a) shows an AFM image of a 44 nm-thick film with a root-mean-square roughness of 0.25 nm. The step terrace structure of the underlying DSO substrate is still clearly visible, underlining the smooth film morphology. The inset of Fig. 3(a) shows a streaky RHEED pattern acquired along the LIO [110] azimuth of the film indicating epitaxial two-dimensional growth. Fig. 3(b) shows a symmetric

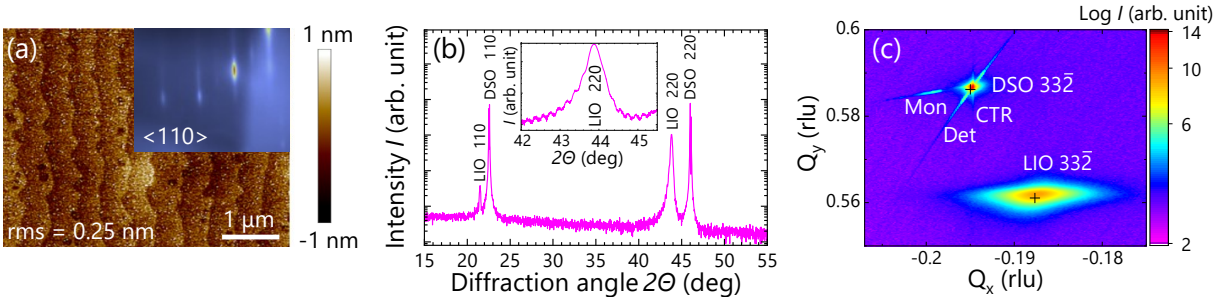

Fig. 3. (a) AFM image of a 44 nm-thick LIO layer. The step terrace structure of the underlying DSO substrate is still clearly visible. Inset: RHEED pattern acquired along the [110] azimuth of the LIO layer. (b) Wide-range X-ray ω - 2Θ scan of the LIO/DSO heterostructure indicating absence of secondary phases. Inset: LIO 220 reflex with thickness fringes of a 44 nm-thick LIO Layer. (c) RSM of the 33$\bar{2}$ reflex of a 165 nm-thick LIO layer grown on DSO substrate under similar conditions as the sample in (a) and (b). The crystal truncation rod, the monochromator streak, and the detector streak are labeld by CTR, Mon, and Det, respectively. The black squares show the theoretically expected reflex positions indicating an almost fully relaxed LIO layer.

2Θ - ω XRD scan along the out-of-plane direction. No additional phases (e.g., In_2O_3 or La_2O_3) were observed and the thickness of the LIO film was determined by the thickness fringes of the LIO 220 reflex shown in the inset. The full-width-at-half-maximum (FWHM) of the ω-rocking curve (not shown) of the LIO 220 reflex for samples inside the growth window ranged from 0.09° to 0.11° revealing the growth of high-quality LIO on DSO for the given fair lattice match. A reciprocal space map (RSM) of the 33$\bar{2}$ reflex of a 165 nm thick LIO film on a DSO substrate is shown in Fig. 3(c). The black crosses mark the theoretically expected position of the DSO and LIO reflexes indicating an almost fully relaxed LIO layer despite the broadened LIO peak.

For samples that were grown at higher or lower oxygen partial pressures, the FWHM values of the rocking curve increased by a factor of 3–5 indicating the boundaries of the growth window. Furthermore, an additional phase was observed in XRD measurements for a sample that was grown at 730 °C substrate temperature and with $P_{O_2} = 7.8\times10^{-8}$ mbar (not shown). We identified this phase as In_2O_3 by its 222 reflex in agreement with the predicted In-rich regime in Fig. 2(a). However, even though our findings of an appropriate growth window overlap with the predicted region in Fig. 2(a), the size of the window resulting in high quality $LaInO_3$ films is significantly smaller than one would assume from the calculated phase diagram and may need further investigation of the film quality as a function of both pressure and temperature.

In summary, we have developed the adsorption-controlled epitaxial growth of LIO films by plasma-assisted MBE. Growth on DSO substrates results in single crystalline films with smooth morphology. In combination with our existing expertise in the MBE-growth of BSO(100) layers, the gained understanding on LIO growth enables us to next realize LIO/BSO heterostructures in pursuit of the interfacial 2DEG in this polar/non-polar perovskite heterostructure.

Bandgap widening and behavior of Raman-active phonon modes of cubic single-crystal $(In,Ga)_2O_3$ alloy films

J. Feldl, M. Feneberg[1], A. Papadogianni, J. Lähnemann, T. Nagata[2], O. Bierwagen, R. Goldhahn[1], M. Ramsteiner

The sesquioxides In_2O_3 and Ga_2O_3 are wide-bandgap semiconductors, which hold promise for applications in the field of transparent electronics. Since the fundamental bandgaps of these two binary compounds in their most stable structural phases span the range from 2.7 eV (In_2O_3) to 4.8 eV (Ga_2O_3), an extended tunability of the electronic properties is expected for $(In,Ga)_2O_3$ alloys. However, the crystal structure of In_2O_3 is cubic bixbyite, whereas Ga_2O_3 assumes a monoclinic structure (β-Ga_2O_3) in thermal equilibrium. Accordingly, the knowledge about the miscibility of the binary compounds for a specific crystal structure is of crucial importance. Furthermore, material properties such as the electronic band structure and the behavior of phonon modes in $(In,Ga)_2O_3$ alloys are of fundamental interest.

In this work, we use spectroscopic ellipsometry, hard X-ray photoelectron spectroscopy, and Raman spectroscopy to study the electronic and vibrational properties of high-quality, cubic, single-crystal $(In,Ga)_2O_3$ films synthesized by molecular beam epitaxy (MBE).

The $(In_{1-x}Ga_x)_2O_3$ films were grown on (111) surfaces of yttria-stabilized zirconia substrates by plasma-assisted MBE at a substrate temperature of 600 °C. After growth, the nominally undoped samples were thermally annealed under an oxygen atmosphere leading to carrier concentrations of several 10^{17} cm^{-3}. For studying free-carrier related phenomena, a Sn-doped alloy film with a nominal Ga content of 8 % was grown. All films are cubic (bixbyite structure) with Ga contents of $0 \leq x \leq 0.1$

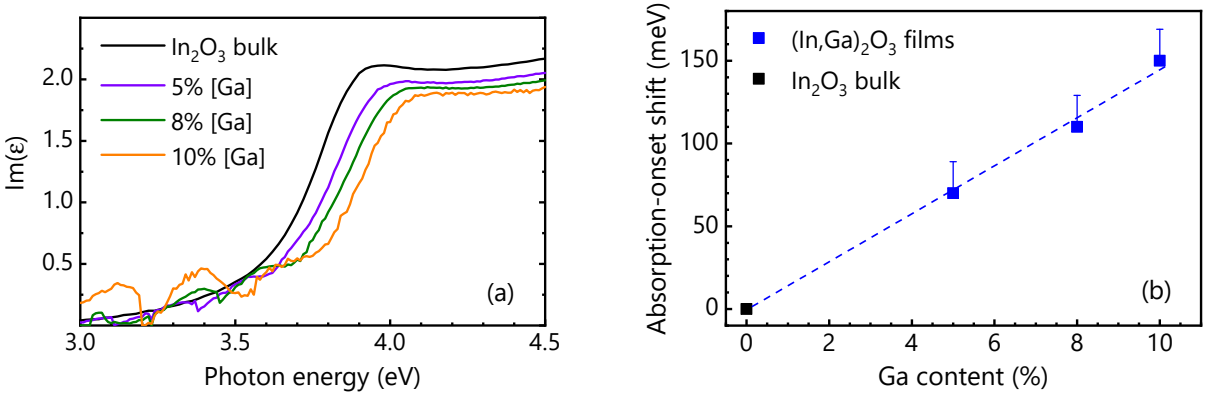

Fig. 1. (a) Point-by-point fitted imaginary part of the dielectric functions ϵ in the spectral range between 3.0 and 4.5 eV for nominally undoped $(In,Ga)_2O_3$ films with different Ga contents. (b) Energy shift of the absorption onset with respect to that of cubic In_2O_3 as a function of Ga content. The error bars indicate an estimated correction for the influence of the strain on the absorption onset.

[1]Institut für Physik, Otto-von-Guericke-Universität Magdeburg, Germany.
[2]National Institute for Materials Science, Tsukuba, Japan.

according to energy-dispersive X-ray spectroscopy. In addition, a high-quality, bulk single-crystal In_2O_3 sample was utilized for reference purposes.

Figure 1(a) displays the imaginary parts of the dielectric functions (DFs) for the undoped $(In,Ga)_2O_3$ films in the spectral range between 3.0 and 4.5 eV measured by spectroscopic ellipsometry. The binary film exhibits an onset of optical absorption at about 3.8 eV as previously reported for undoped or low doped In_2O_3. Due to the dipole forbidden nature of the fundamental bandgap, this absorption onset is related to the dipole-allowed transition from the conduction band minimum to a lower lying valence band. The DFs of the alloy films provide clear evidence for a blueshift of the onset of optical absorption with increasing Ga content as shown in Fig. 1(b), which reveals a nearly linear relationship with a slope of $\Delta E/\Delta x = 1{,}450$ meV. Our finding is in strong contrast to several publications, where even a redshift is reported as a consequence of the incorporation of Ga into In_2O_3. For our oxygen annealed samples with carrier concentrations of no more than 10^{18} cm^{-3}, carrier induced effects such as the Burstein-Moss shift can be neglected. Regarding the possible influence of residual lattice strain on the optical absorption onset of the alloy films, it has to be considered that maximum tensile in-plane strain values of about 0.2 % have been determined by X-ray diffraction measurements for In_2O_3 films with thicknesses above 200 nm grown under the same conditions. Assuming such a strain level for the present alloy films, a strain-induced redshift of the optical absorption onset by 19 meV would have to be taken into account. In accordance with our findings for the optical bandgap, the results obtained by X-ray photoelectron spectroscopy (not shown here) reveal also for the fundamental bandgap a monotonic increase with Ga content, again in contrast to the initial redshift reported in several publications.

The carrier concentration in the Sn doped alloy film could be varied by different annealing conditions from 4×10^{19} to 3.5×10^{20} cm^{-3}, which allowed us to investigate the impact of the doping level for an alloy film at exactly the same Ga content ($x = 8$ %). From the DFs in the spectral range between 3.0 and 4.5 eV (not shown here), a shift of the absorption onset is deduced, which monotonically increases with carrier concentration up to 350 meV, in quantitative agreement with the results obtained for cubic In_2O_3. The parameter-free point-by-point DFs in the infrared spectral range are shown in Fig. 2. Using the

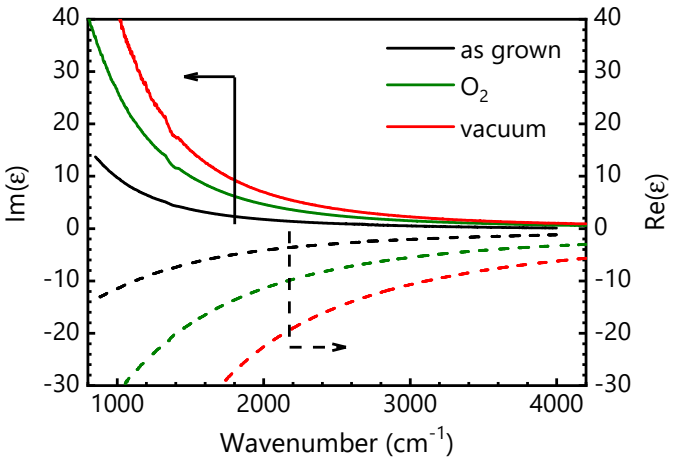

Fig. 2. Point-by-point fitted infrared dielectric functions (solid lines: real parts, dashed lines: imaginary parts) of an n-type doped $(In,Ga)_2O_3$:Sn film ($x = 0.08$) before (as-grown) and after oxygen and vacuum annealing.

Drude model for the free-carrier contribution to fit the line shape of the complex DFs, the deduced plasma frequencies exhibit the expected monotonic increase with carrier concentration. The accordingly derived effective masses (0.2 to $0.33m_0$) depend on the doping level, in accordance with the case of cubic In_2O_3. However, a significant change of the effective masses induced by Ga incorporation could not be extracted. Most importantly, our results demonstrate that the advantage of bandgap engineering by alloying can be transferred to transparent conducting oxides.

Room temperature (295 K) Raman spectra of the nominally undoped $(In,Ga)_2O_3$ films are shown in Fig. 3 for excitation close to the optical bandgap of In_2O_3. The spectrum of the In_2O_3 reference sample exhibits the expected optical phonon lines between 135 and 635 cm^{-1}. The same optical phonon lines are resolved in the spectra of the $(In_{1-x}Ga_x)_2O_3$ samples with an increased line width and a shift to higher frequencies, with the exception of a few low-intensity and high-frequency modes. This finding confirms the bixbyite structure of the alloy films for Ga contents up to 10 %. No splitting could be observed for the phonon modes from the alloy samples, indicating a one-mode behavior of the corresponding phonon modes.

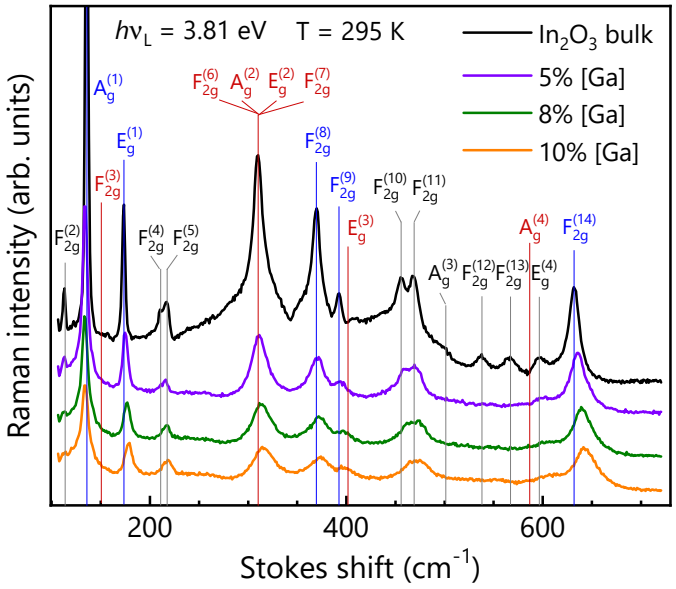

Fig. 3. Room temperature (295 K) Raman spectra of $(In_{1-x}Ga_x)_2O_3$ films for different nominal Ga contents x and a reference In_2O_3 bulk sample excited at a photon energy of 3.81 eV. The frequencies of the phonon modes marked by vertical lines and labels. The frequencies of the modes marked by blue vertical lines are shown in Fig. 4.

A reliable evaluation of the dependence on the Ga content has been possible for five optical phonon modes. The shifts of their Raman peak frequencies with respect to the corresponding In_2O_3 frequencies are shown in Fig. 4 as a function of the Ga content. The modes $E_g^{(1)}$, $F_{2g}^{(8)}$, $F_{2g}^{(9)}$, and $F_{2g}^{(14)}$ exhibit a nearly linear blueshift with increasing Ga content. In contrast, only for the $A_g^{(1)}$ mode a redshift is found with a very weak dependence on the Ga content. The nearly linear dependences observed for most phonon frequencies (cf. Fig. 4) provide evidence for the absence of a solubility limit regarding the substitutional incorporation of Ga on group-III lattice sites in In_2O_3 for Ga contents up to 10 %. In contrast, a constant phonon mode frequency for Ga contents larger than 6 % has been reported for sintered ceramic alloy films in the literature. The occurrence of a maximum phonon frequency following an initial linear blueshift has been explained by phase separation. Consequently, our results provide evidence for a

higher Ga solubility limit for alloy films grown by MBE under the chosen conditions.

The phonon frequencies are expected to depend on the residual lattice strain in the alloy films. As mentioned above, a maximal tensile in-plane strain level of about 0.2 % has been found for In_2O_3 films grown under the same conditions. For such a strain level, a redshift of the phonon modes by roughly 0.35 % has been observed for binary In_2O_3 films (not shown here). Assuming the same relative strain-induced frequency shift for the alloy films, the data shown in Fig. 4 are displayed with error bars, which indicate the correction for the expected strain-induced redshift on the high-frequency side. In contrast to the optical absorption onset, the influence of free carriers on the phonon modes in centrosymmetric bixbyite films can be neglected for our analysis. Altogether, several optical phonon modes appear to be suitable for the determination of the Ga content in $(In,Ga)_2O_3$ films by Raman spectroscopy. In this respect, the $F_{2g}^{(14)}$ mode at 635 cm^{-1} is best suited, i.e., it has the strongest absolute dependence on the Ga content (cf. Fig. 4). In fact, we have been able to reveal phase separation in MBE-grown alloy films for Ga contents above 10 % in the framework of a more recent study.

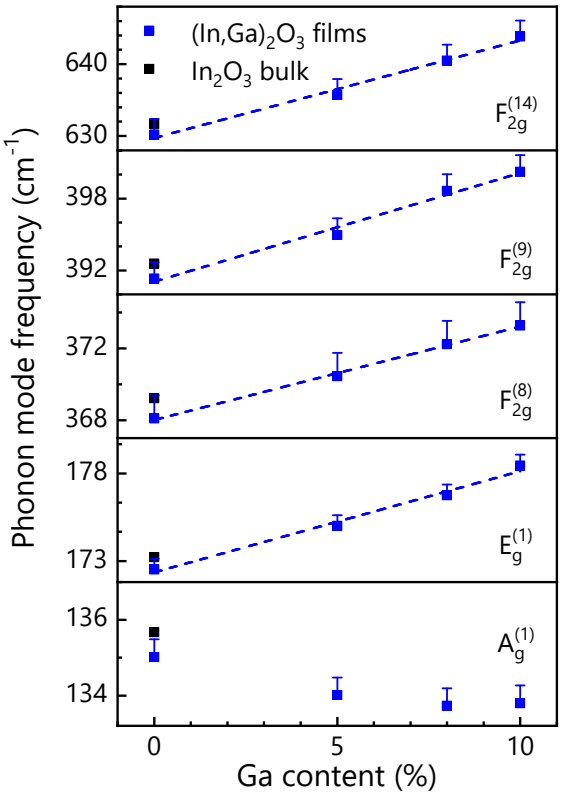

Fig. 4. Room temperature phonon mode frequencies observed in Raman spectra of $(In_{1-x}Ga_x)_2O_3$ films as well as in bulk In_2O_3 as a function of the nominal Ga content (x). The error bars indicate a correction for the expected strain-induced redshift.

We would like to thank Dr. Zbigniew Galazka for providing us with the state-of-the-art In_2O_3 bulk reference sample. This work was performed in the framework of GraFOx, a Leibniz-ScienceCampus partially funded by the Leibniz association.

Electronic end states in dimerized quantum-dot chains engineered atom by atom

V. D. Pham, S. C. Erwin, F. v. Oppen, K. Kanisawa, S. Fölsch

A topological insulator is nonconducting in its interior but has metallic surface states within the energy band gap resulting from the atomic structure and symmetry of the bulk. The surface states cannot be removed by perturbations as long as the bulk spectrum remains gapped. This robustness is remarkable from the fundamental point of view and suggests new technological applications. The Su-Schrieffer-Heeger (SSH) model of polyacetylene constitutes a particularly clear and important example of a one-dimensional (1D) topological phase. It represents a chain of degenerate orbitals in which electrons can hop with alternating amplitude between nearest-neighbor sites. This simple picture captures the properties of symmetry-protected boundary states at the interface between distinct topological phases.

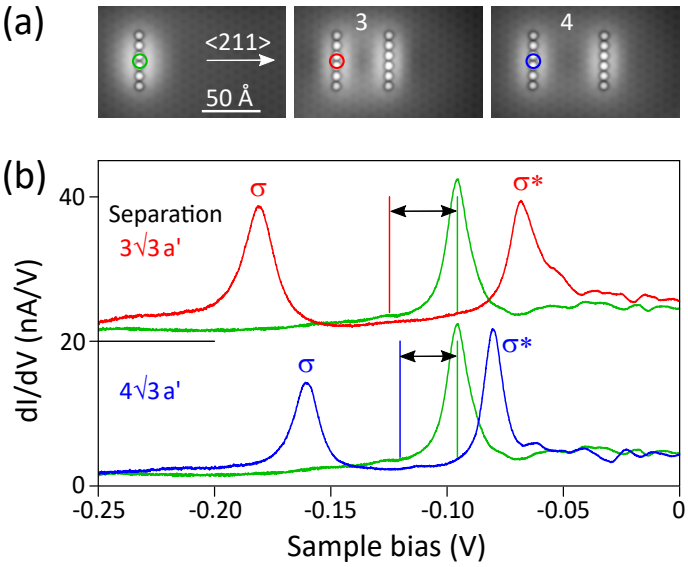

Fig. 1. (a) STM images (0.1 nA, 0.1 V) of a quantum-dot monomer (left) made of six In adatoms and quantum-dot dimers (center and right) with interdot separations of 3 and 4 in units of $\sqrt{3}a'$, $a' = 8.57$ Å is the surface-lattice constant. (b) Conductance spectra of the monomer (green) and the two dimers (red and blue): the monomer gives rise to a confined state about 0.1 eV below E_F while a bonding (σ) and an antibonding state (σ^*) emerge for the dimers [spectra taken at the tip positions marked in (a)]. Arrows indicate the downshift of the $\sigma - \sigma^*$ doublet relative to the monomer energy induced by the potential that each dot experiences from the other.

Using the approach of atom manipulation by cryogenic scanning tunneling microscopy (STM) we created dimerized quantum-dot chains on the InAs(111)A surface to mimic the alternating hopping of the SSH model. The building block of the chains is a "longish" quantum dot consisting of six indium adatoms lined up on adjacent surface sites. The left hand-side panel in Fig. 1(a) shows an STM topography image of such an In_6 dot in which the adatoms are evenly spaced by $a' = 8.57$ Å (a' is the surface-lattice constant of the 2×2 In vacancy reconstruction). Placing the STM tip at constant height above the dot and recording the bias-dependent conductance dI/dV (as an approximate measure of the electronic density of states) yields the green spectrum reproduced in the upper and lower part of Fig. 1(b). A single conductance peak is observed indicating a state at about 0.1 eV below the Fermi level (at sample bias $V = 0$). We showed earlier that this state derives from surface-state electrons of pristine InAs(111)A which are confined by the positively charged In adatoms constituting the dot.

The center and right hand-side panels of Fig. 1(a) show STM topography images of individual quantum-dot dimers with interdot separations of 3 (center) and 4 (right) in units of $\sqrt{3}a'$. The corresponding conductance spectra in Fig. 1(b) [red and blue curve] reveal a bonding (σ) and an antibonding state (σ^*) resulting from the quantum coupling between the dots in the dimer. This coupling decreases with increasing separation as evident from the observed $\sigma - \sigma^*$splittings. In addition, the $\sigma - \sigma^*$ doublet is downshifted relative to the corresponding confined-state energy of an individual In_6 dot. This shift decreases as the interdot separation increases. We interpret it as an electrostatic shift which arises from the potential change that each dot experiences from the other.

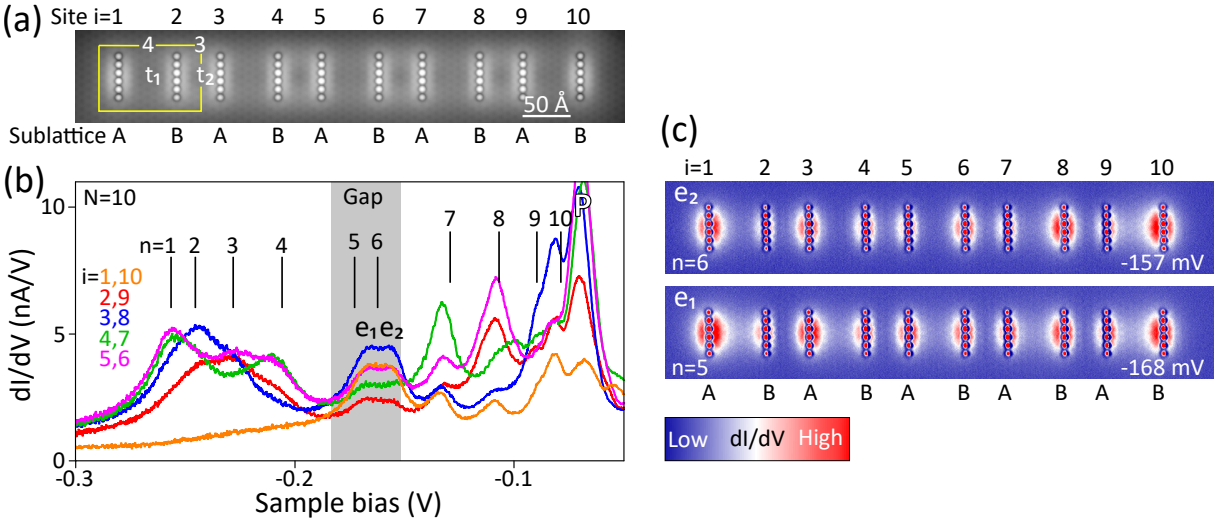

Fig. 2. (a) STM image (0.1 nA, 0.1 V) of a dimer chain with $N = 10$ dots and alternating separations of 4 and 3 in units. The unit cell marked yellow contains two dots residing on A and B sites of the sublattice structure, respectively. The intracell hopping t_1 is smaller than the intercell hopping t_2. (b) Conductance spectra obtained with the tip probing the sites indexed i (spectra taken at symmetry-equivalent sites are averaged). Vertical bars mark the levels calculated for a SSH chain with $N = 10$ and hoppings $(t_1, t_2) = (39, 55)$ meV; the levels are rigidly shifted in energy to match the sequence of conductance peaks, the gap region of an infinite chain is shaded gray. The observed conductance peaks within the gap (labelled e_1 and e_2) reveal the emergence of end states. The spectral feature labelled P indicates a bound state of the electron accumulation layer and does not belong to the molecular states of the dimer chain. (c) Conductance maps recorded at constant tip height and at the biases where the states e_1 and e_2 are observed in the spectra. The states have maximum probability density at the end sites and decay on their respective sublattice into the bulk.

In a next step, we assembled chains of quantum-dot dimers. The STM topography image in Fig. 2(a) shows a chain consisting of five dimers, thus a total of $N = 10$ dots. The unit cell occupied by a single dimer is marked yellow. Each unit cell contains one dot residing on sublattice A and the other on sublattice B. In this particular example, the separation within each cell is 4 units whereas the intercell separation is 3 units. In a single-particle tight-binding (TB) description, we assume that the hopping is half the $\sigma - \sigma^*$ splitting of the individual dimers shown in Fig. 1. The hopping within a cell is thus $t_1 = 39$ meV while that between cells is larger, $t_2 = 55$ meV, implying that the weaker hopping occurs at the ends. In the SSH model this choice of alternating

hopping leads to the emergence of a localized state at both ends of a finite chain, one residing on sublattice A and the other on sublattice B. In the limit of a long chain, these end states are centered in the energy band gap of the dimerized chain and decay exponentially into the bulk. In a finite chain, the overlap of the end states leads to an energy splitting between their odd and even superpositions.

Figure 2(b) shows conductance spectra obtained by probing the dots along the dimer chain. A sequence of conductance peaks is observed which reflect the "molecular" states of the finite chain. For comparison, the vertical bars mark the theoretical energy levels of a finite SSH chain with $N = 10$ labelled by the quantum number n. The theoretical energies were obtained from the eigenvalues of the corresponding TB Hamiltonian assuming the hopping values (t_1, t_2) discussed above plus a rigid shift (equivalent to constant but nonzero onsite energy) to match the experimentally observed peaks. The gray-shaded area marks the gap between the energy bands of the corresponding infinite dimer chain with a gap width of $2|t_1 - t_2|$. The theoretical levels with $n = 5$ and 6 correspond to the split end states within the gap.

It is evident from Fig. 2(b) that the experimental spectra are essentially consistent with the theoretical level structure. Of particular interest are the two states observed in the mid-range, labelled e_1 and e_2, which are located within the predicted gap region. Figure 2(c) shows spatial conductance maps of the dimer chain recorded at the bias voltages where the two states e_1 and e_2 are observed in panel (b). The maps reveal that the states e_1 and e_2 have maximum probability density at the end dots and reside predominantly on A (B) sites in the left (right) half of the chain. Indeed, this observation is consistent with the case of a finite SSH chain for which the split end states reside on the two different sublattices and decay into the bulk.

Nevertheless, there are also deviations from the ideal SSH case. Most notably, the measured energy levels are asymmetric about their average value. In contrast, the SSH model implies sublattice symmetry and thereby a level spectrum that is symmetric about the center of the gap. The experimentally found asymmetry is a consequence of sublattice-symmetry breaking which arises because the dots are charged and create an onsite potential along the chain that is higher at the ends than in the middle. The effect of finite screening – which is characteristic for a semiconductor material as investigated here – also leads to the aforementioned observation that the $\sigma - \sigma^*$ doublet of an individual dimer is downshifted relative to the corresponding confined-state energy of a single dot [cf. Fig. 1(b)]. We performed a TB analysis which includes the screened potential from all the In adatoms to further quantify the impact on the energy level spectrum and the wave functions of the observed states. Notwithstanding these deviations from the ideal SSH case, the end states indeed exist in the dimerized quantum-dot chains realized in this project.

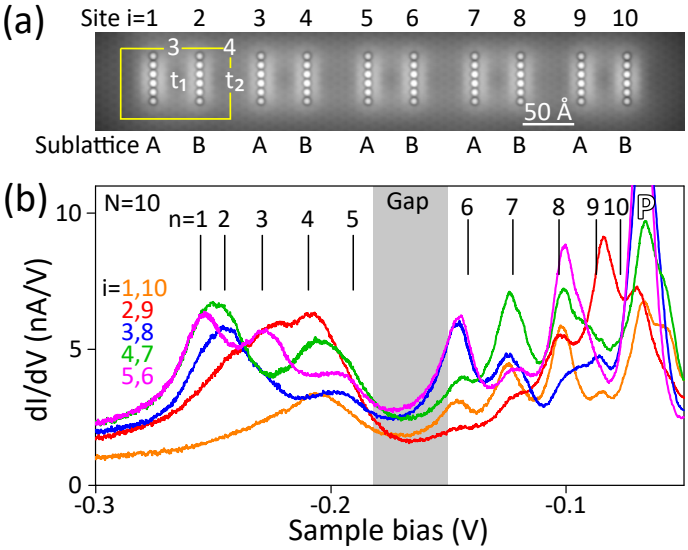

Fig. 3. (a) STM topography image (0.1 nA, 0.1 V) of a dimer chain made of $N = 10$ dots with alternating spacings inverted relative to those of the chain in Fig. 2. The intracell hopping t_1 is larger than the intercell hopping t_2, suggesting that the chain is in the trivial phase. (b) Corresponding conductance spectra and SSH level structure (vertical bars) calculated with hoppings $(t_1, t_2) = (55, 39)$ meV. In agreement with the expectation for the trivial phase, no conductance peaks fall into the gap region of an infinite dimer chain with the hopping values quoted above.

To finally verify these findings, the dimer chain discussed above can be rearranged in a way that the stronger hopping occurs at the ends. This situation is illustrated by the STM topography image in Fig. 3(a) showing a chain of five dimers in which the alternating hopping is inverted relative to the previous case in Fig. 2(a). Within the SSH model, this configuration corresponds to the trivial phase lacking any end states. Accordingly, all theoretical levels shown as vertical bars in Fig. 3(b) lie in the range of the bands and there are no states within the gap. Again, this prediction is consistent with the experimental spectra in Fig. 3(b).

In our ongoing work we find that also domain walls introduced between the two dimerizations somewhere along the chain give rise to localized states within the gap, in agreement with the SSH model. This shows that the quantum-dot chains explored here provide a versatile means to create artificial boundary states in a 1D electron system.

Coordination Environment of Ga in Amorphous and Annealed $(In,Ga)_2O_3$ and Ga_2O_3 Studied by X-ray Absorption Spectroscopy

A. Reis, M. Hanke, P. Mazzolini[1], O. Bierwagen, E. Welter[2], A. Trampert

Ga_2O_3 is an ultra-wide bandgap semiconductor ($E_g \approx 4.8$ eV) and therefore a promising candidate for the implementation of high-power transistors and UV light emitting diodes. Alloying it with In_2O_3 ($E_g \approx 2.7$ eV) allows for band gap tuning and the design of heterostructure devices. Ga_2O_3 as well as In_2O_3 can crystallize in multiple bulk phases, the most stable ones are monoclinic β-Ga_2O_3 and cubic δ-In_2O_3. The behaviour of heavily disordered systems and the process of phase formation upon crystallization of amorphous solid solutions has recently been addressed by in-situ transmission electron microscopy techniques [C. Wouters *et al.*, Microscopy and Microanalysis **25**(S2), 1890 (2019)]. Complementary to microscopy or diffraction techniques the measurement of the Extended X-ray Absorption Fine Structure (EXAFS) is able to serve as a suitable analytical tool to gain statistical information on the coordination environment of a particular type of atom even in cases when long range order is missing.

Amorphous Ga_2O_3 and $(In_xGa_{1-x})_2O_3$ films of 250 nm thickness and a nominal concentration x=0.5 were deposited at a low growth temperature of 100 °C on a Si (111) substrate in a molecular beam epitaxy chamber. Subsequently, the samples underwent annealing at 800 °C for 15 min in a pure O_2 atmosphere. EXAFS measurements were performed at beamline P65 (synchrotron PETRAIII, Hamburg) across the Ga K-edge at 10367 eV. With respect to the thick Si substrate, data were collected in fluorescence mode. At incident angles ϕ of 25°, 45° and 65° five spectra of each sample were acquired to access the orientation dependence of the spectra.

A major challenge of the measurement on crystalline substrates is the presence of numerous diffraction peaks in the spectra due to the fulfilment of the Bragg condition. In particular artificial high frequencies are added, potentially affecting the EXAFS in the frequency region where multiple scattering at higher coordination shells takes place. To some extend the problem can be overcome since the Bragg condition is angle dependent. First, the spectra were processed for each angular position ϕ separately, i.e. normalization and background removal were performed. Out of this redundant data set, a minimum function for the normalized absorption coefficient $\mu(E)$ can be derived, which eventually yields the EXAFS spectrum $\chi(k)$.

Figure 1(a) shows the resulting EXAFS oscillations probed at the as-grown (amorphous) and annealed samples. Instead of $\chi(k)$ we plot here a weighted EXAFS func-

[1]Department of Mathematical, Physical and Computer Sciences, University of Parma, Viale delle Scienze 7/A, 43124 Parma, Italy

[2]Deutsches Elektronen-Synchrotron, Notkestrasse 85, 22607 Hamburg, Germany

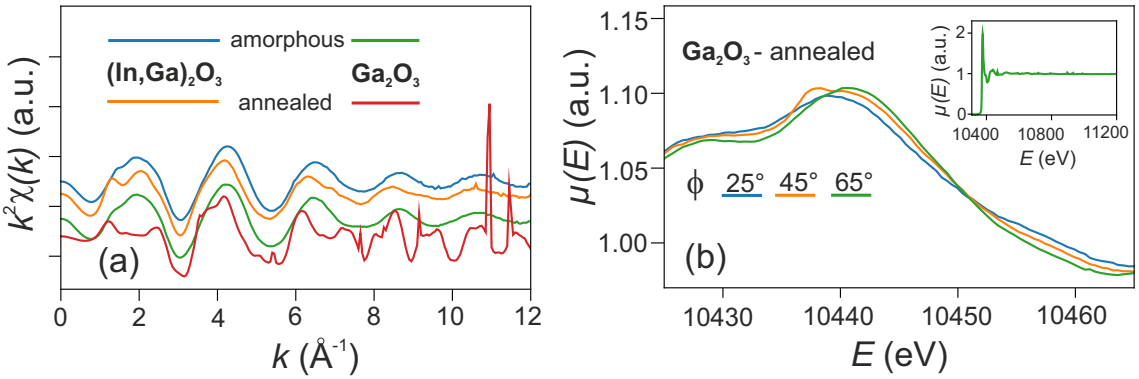

Fig. 1. (a) k^2-weighted EXAFS function $\chi(k)$, i.e. $k^2\chi(k)$, as taken at amorphous and annealed Ga_2O_3 and $(In,Ga)_2O_3$ layers. Smooth oscillations are visible but for the case of annealed Ga_2O_3 Bragg peaks are superimposed. (b) The normalized absorption coefficient $\mu(E)$ of the annealed Ga_2O_3 layers as a function for various incident angles ϕ, showing that different crystallites were probed. The inset shows $\mu(E)$ for an extended energy range.

tion $k^2\chi(k)$. For both spectra of the ternary $(In,Ga)_2O_3$ as well as the amorphous Ga_2O_3 layer this data evaluation process is straight forward, whereas for annealed Ga_2O_3 the strongly fluctuating signal $k^2\chi(k)$ carries several Bragg peaks on top. All recorded EXAFS spectra reflect this issue. Figure 1(b) reveals a part of the normalized absorption coefficient $\mu(E)$ for different incident angles. The oscillations vary in shape, implying that the annealing process induced the formation of a range of disordered crystallites. Since each time other crystallites were probed the Bragg peaks cannot simply be separated from the spectrum by the application of a filter. The inset depicts a normalized extended absorption spectra across the Ga K-edge.

Figure 2(a) shows the absolute value of the Fourier transformed EXAFS function $|\chi(R)| = |\mathcal{F}[k^2\chi(k)]|$ of the amorphous and annealed $(In,Ga)_2O_3$ layers. Both spectra exhibit only one peak originating from single scattering at the first coordination shell. The curve maximum is located at 1.41 Å in both cases, which means that the length of the scattering path and thus the coordination length for next-nearest-neighbor has not been changed. Hence the annealing process did not lead to the formation of higher coordination shells under the given conditions. Figure 2(b) contains $|\chi(R)|$ for the amorphous and annealed Ga_2O_3 layers. The spectral function of the as-grown one has one single maximum at 1.41 Å as well, thus surprisingly the scattering length is identical to the one measured in the ternary alloy. As we assume that the first shell consists only out of O-atoms this implies that the coordination length in both systems must be the same despite the comparatively large atomic number (Z = 49) for In. Consequently the initial amorphous state is very similar to the one of the ternary alloy as deduced from to the Ga–O binding length. On the other hand, the spectral function $|\chi(R)|$ of the annealed Ga_2O_3 layer as probed at different angles ϕ depicts peaks due to the scattering at higher coordination shells indicating that crystallization has started. Additional to the first maximum at 1.38 Å (Ga–O bonds), further broad peaks appear between 2.73

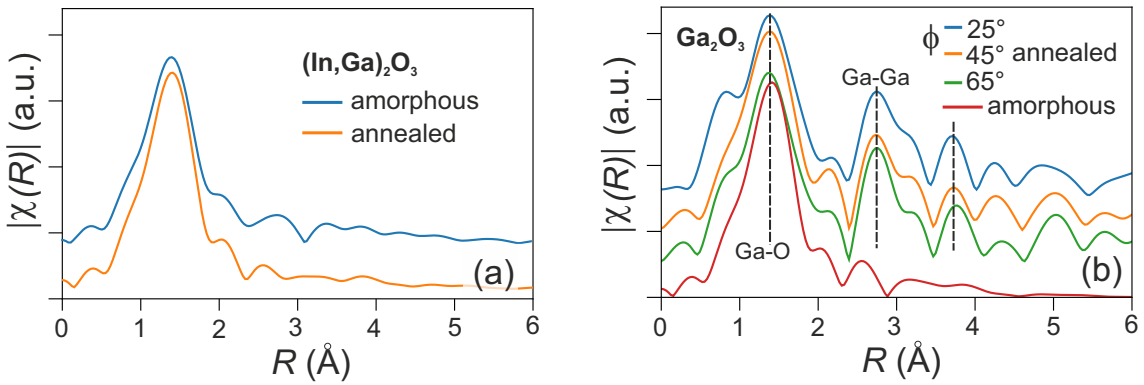

Fig. 2. (a) Magnitude of the Ga-EXAFS function $|\chi(R)|$, which is equivalent to the absolute value of the Fourier transformation $|\mathcal{F}[k^2\chi(k)]|$ of amorphous and annealed $(In,Ga)_2O_3$. Only first shell scattering with identical path lengths is observed. (b) $|\chi(R)|$ of amorphous and annealed Ga_2O_3. Annealing changes the local ordering within the material by the formation of higher coordination shells (dashed lines). Besides the omnipresent Ga–O coordination, a second shell due to Ga–Ga bonds becomes visible and even a third one might be recognized. Curves are vertically shifted for better readability.

and 2.76 Å (Ga–Ga bonds) and between 3.71 and 3.77 Å (Ga–O bonds). These maxima slightly vary in position and amplitude due to the degree of disorder in the not yet completely crystallized Ga_2O_3.

Our results can be compared to those of other groups, who also considered disordered and crystallized Ga_2O_3 films by means of X-ray absorption spectroscopy. H. Yang *et al.* [Appl. Surf. Science **479**, 1246 (2019)] report on a series of Ga_2O_3 thin films grown by pulsed laser deposition at different growth temperatures. For growth temperatures below 700 °C exclusively first shell scattering takes place, whereas for higher temperatures additional second shell features have been observed. S.C. Siah *et al.* [Appl. Phys. Lett. **107**, 252103 (2015)] compared spectra of amorphous Ga_2O_3 thin films to the one of monoclinic β-Ga_2O_3 single crystals. The Fourier transformed EXAFS of the disordered films exhibits only one peak. However, in case of the single crystal multiple peaks originating from higher shell scattering emerge. Values given for the first coordination shell (i.e., Ga–O bond length) coincide very well with our observation ($\Delta R < 0.1$ Å). In case of second coordination shell (Ga–Ga bonds) both groups report distances similar to our findings. Therefrom we conclude that in our case β-Ga_2O_3 has been formed.

In the next step the smooth spectra of Ga_2O_3 and $(In,Ga)_2O_3$ will be fitted using the EXAFS equation given by

$$\chi(k) = S_o^2 \sum_j \frac{N_j f_j(k)}{kR_j^2} e^{-2k^2\sigma_j^2} e^{-2R_j/\lambda(k)} sin(2kR_j + \delta_j(k)),$$

where j indicates the scattering path, R_j the half path length, S_o^2 the scattering amplitude, N_j the coordination number of atoms in the jth shell, σ the Debye-Waller factor and $\lambda(k)$ the mean free electron path length. The scattering amplitude $f_j(k)$ and the phase shift $\delta_j(k)$ are dependent on the atomic number of the scattering atoms. The obtained coordination lengths can then be compared to the result of complementary

measurements, especially X-ray and electron diffraction. The coordination number is of particular interest as it might give evidence whether one of the crystal phases is predetermined by the arrangement of the cations in the solid solution.

To rule out the influence of the Bragg peaks on the signal further EXAFS measurements pursuing a different approach will be performed. Promising candidates would be oxide films on amorphous substrates, as e.g. on glass. EXAFS data taken at the oxygen K-edge at 543 eV (preferably at the synchrotron BESSYII) can provide complementary information since the photo electrons are originating from the oxygen sublattice. Additionally Bragg artifacts are not present at this X-ray energy.

In conclusion we gained information about the coordination environment in disordered Ga_2O_3 and $(In,Ga)_2O_3$ thin films before and after annealing. In case of $(In,Ga)_2O_3$ layers, annealing at 800 °C for 15 min in a pure O_2 does neither lead to scattering at higher coordination shells nor a change of the Ga–O bond length in the first coordination shell. This signifies that short range order is preserved under the given conditions and crystallization has not yet taken place. In case of Ga_2O_3 layers the scattering length of the first shell slightly decreases upon annealing. There are additional contributions to the spectral EXAFS function originating from subsequent Ga–Ga and Ga–O coordination shells. Obviously the annealing process initiates a crystallization process leading to the formation of multiple disordered crystallites of the β-phase.

Impact of Bi on breakdown of epitaxy of low temperature GaAs:Bi

E. Luna, M. Wu[1], T. Aoki[2], M. R. McCartney [2], J. Puustinen[3], J. Hilska [3], M. Guina [3], D. J. Smith [2], A. Trampert

Complex morphology is observed in the GaAs:Bi cap layer of Ga(As,Bi) films grown on GaAs(001) by low-temperature (LT) molecular beam epitaxy (MBE). In recent years, there has been increased interest in the so-called dilute-bismide alloys, due to their potential benefits for high-performance mid-infrared lasers, detectors, and other photonic and/or spintronic devices. In order to successfully incorporate Bi into III-V semiconductors, e.g. GaAs, the material is usually grown under nonconventional growth conditions, which in the case of MBE involve LT growth with substrate temperatures (T_s) below 400°C and a careful control of the As-to-Ga flux ratio close to stoichiometry. Whereas the microstructure of Ga(As,Bi) is extensively investigated, there are scarce reports on the microstructure of the adjacent LT-GaAs material used as barrier and/or cap layer. Furthermore, the incorporation of excess Bi and/or segregated Bi from the underneath Ga(As,Bi) layer into LT-GaAs is anticipated, further complicating the already complex LT-GaAs system.

Using a combination of transmission electron microscopy (TEM) methods, including advanced scanning (S)TEM techniques, we analyze the intricate morphology of the LT-GaAs:Bi cap layer of some Ga(As,Bi) structures. The microstructure is dominated by the presence of V-shaped twinned domains in the LT-GaAs cap layer and by the (unintentional) inhomogeneous incorporation of Bi from the underlying layer. Numerous "V-shaped" features are detected close to the layer surface, see Fig.1. In addition, vertical stripes are detected in the Ga(As,Bi) layer. These reflect the presence of lateral composition modulations in Ga(As,Bi) stemming from surface spinodal decomposition at the growth front, as already addressed [E. Luna *et al.*, J. Appl. Phys. **117**, 185302 (2015); Nanotechnology **27**, 325603 (2016)]. The V-shape of the domain structures in the LT-GaAs cap layer is defined by the presence of defects and/or periodic patterns along adjacent {111} planes. Some V-shaped domains contain sequences of microtwins and/or stacking faults (SFs), as seen in Fig.2(a)-(b). The microstructure of the domains often resembles complex moiré patterns associated with regions of overlapped twins. Notably, in addition to twinned domains, Bi-rich V-shaped domains are also found. They are characterized by a seemingly perfect crystal structure which show slightly brighter contrast than surrounding areas in high-angle annular dark-field (HAADF) images, as in Fig.2(c), that indicates the presence of atoms with large atomic number Z, most likely Bi atoms, inside the domain. The appearance of the domains closely

[1]Universität Erlangen-Nürnberg, Germany
[2]Arizona State University, USA
[3]Tampere University, Finland

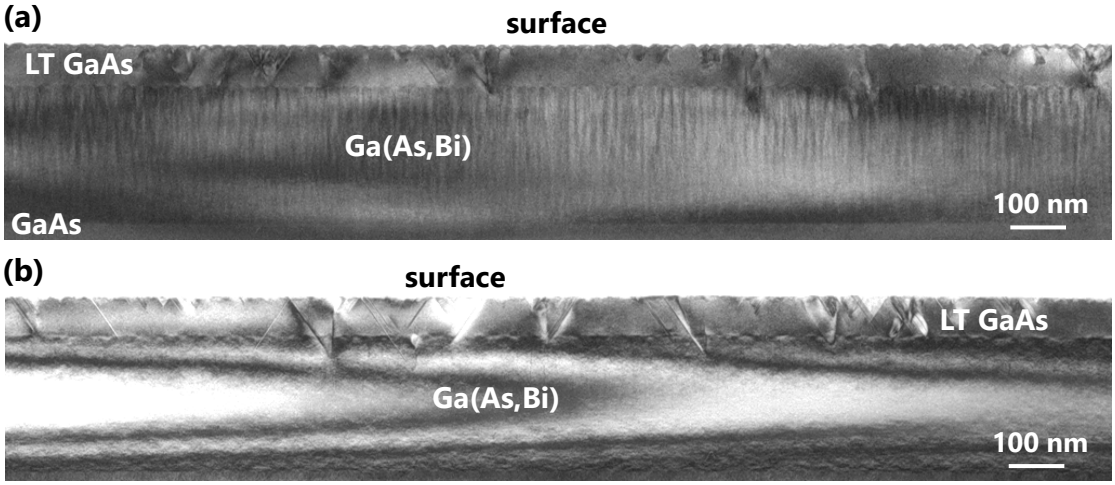

Fig. 1. Overview TEM micrographs of a representative sample showing cross-sections of the Ga(As,Bi)/GaAs heterostructures observed: (a) along the [-110] zone axis, and (b) close to the [110] zone axis. The images were recorded simultaneously, explaining why only one is in exact zone-axis orientation.

resembles that of Bi-rich triple-period-type ordered domains in Ga(As,Bi) epilayers, albeit these here are smaller in size and contain less Bi [M. Wu *et al.*, Appl. Phys. Lett. **105**, 041602 (2014)]. Using different techniques, we have tried to evaluate the average Bi content unintentionally incorporated into LT-GaAs. The measurements suggest that the Bi content in the LT-GaAs cap is very small and below detection limits ($< 1\%$ Bi). Furthermore, the fact that HAADF images show Bi-rich areas in very localized positions indicates that the unintentional Bi incorporation shows preferential incorporation into some specific regions. The Bi atoms which incorporate into LT-GaAs (at trace or impurity levels) most likely stem from the buildup of Bi atoms on the Ga(As,Bi) surface due to the severe and complex Bi segregation in Ga(As,Bi) even for this low T_s and growth conditions.

Advances in aberration-corrected electron microscopy allows investigations of the atomic configurations inside and outside V-shaped domains. Our detailed analysis

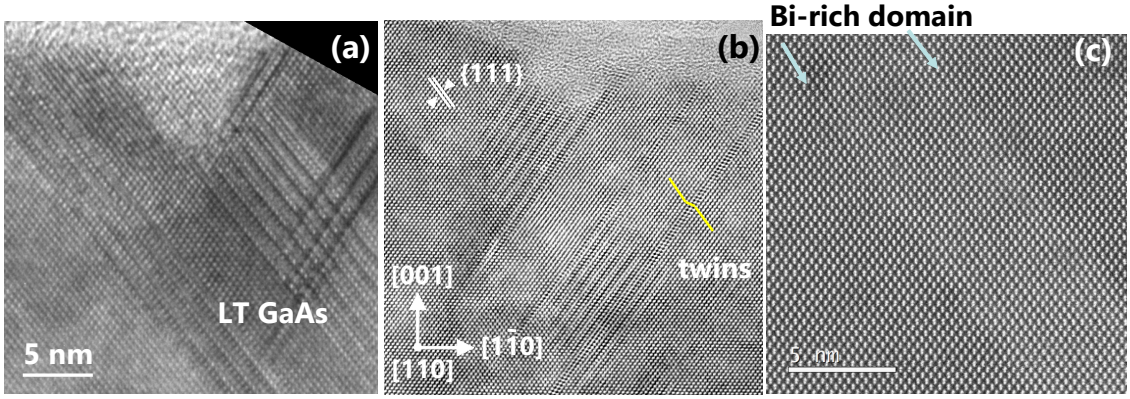

Fig. 2. High-resolution (HR) TEM (a) and aberration-corrected (b) TEM micrographs of V-shaped and semi V-shaped domains in LT-GaAs:Bi cap layer of a representative sample. (c) Atomically resolved HAADF image of Bi-rich domain with a brighter contrast inside the domain (i.e., higher average Z).

of HAADF images at twinned regions unambiguously show that the Ga–As bonds are preserved at the twin planes, i.e. the twins are orthotwins. This can be directly observed in the color-coded HAADF image in Fig.3(a) (noise-reduced via adaptive Wiener filter) and from HAADF intensity line profiles as shown in Fig.3(b)-(c). In our analysis we found no evidence of paratwins, where mirror reflection with respect to the {111} plane gives rise to "wrong" Ga–Ga or As–As bonds across the twin plane. Although paratwins have higher formation energy, these twins would be able to accommodate nonstoichiometry-related point defects by creating, for example, an As excess layer at the twin plane.

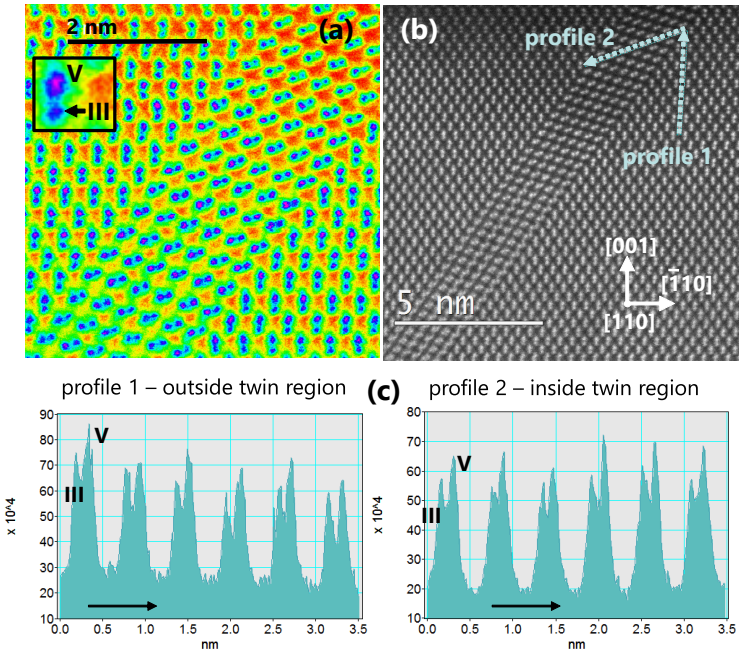

Fig. 3. (a) Color-coded filtered HAADF image and (b) lower magnification HAADF image with intensity line profiles. HAADF images indicate that Ga–As bonds are preserved across twin boundaries.

Some of the twin-containing features observed in the LT-GaAs:Bi cap layer closely resemble the pyramidal-shaped defects frequently occurring in LT-MBE homoepitaxy of semiconductors. A representative example is shown in Fig.4. As observed, in addition to the twins and SFs extending along {111} planes, there is a central defective cone, where an amorphous phase can be locally detected. This very same morphology is indeed recurrently observed in LT-Si, LT-Ge and LT-GaAs and is characteristic of the so-called breakdown of epitaxy associated with LT-growth, a general phenomenon actively investigated in the 1990s. After intense debate over the years, it is nowadays established that such morphology is mainly caused by *kinetic roughening* under LT growth conditions. The accumulation of point defects or the presence of impurities on their own cannot justify the breakdown of epitaxy unless they contribute to the development of surface roughness during growth. In the particular case of LT-GaAs(001), surface kinetics as the origin of breakdown of epitaxy is supported by the evidence that at high As_4 overpressures the surface morphology is characterized by the development of large elongated mounds, significantly increasing surface roughness, prior to the formation of pyramidal-like twinned areas that eventually lead to the breakdown of epitaxy. The mounds develop due to anisotropic adatom diffusion in the presence of Ehrlich-Schwoebel (ES) barriers and is attributed to enhanced adatom surface diffusion at high As/Ga ra-

tios due to an As self-surfactant effect, i.e. the Ga diffusion length is enhanced as the surface is passivated by excess As. Obviously, the presence of ES diffusion barriers, which hinder the downward movement of adatoms at surface step edges so that adatoms tend to accumulate on top of already existing islands, is a key factor in the process. In that respect, the assumed lower adatom diffusivity in LT growth would effectively reduce the consequences of ES barriers and promote a smooth surface unless, for example, a species acting as a surfactant enhances adatom diffusion. This would restore the effect of ES barriers and, depending on the conditions, rapidly increase the surface roughness eventually leading to the observed morphology. In the present case, there are two atomic species potentially behaving as surfactants, As and Bi. Significant As passivation, however, is unlikely to occur here since the samples are grown at near stoichiometric conditions. On the other hand, there is the key presence of Bi atoms, unintentionally incorporated in LT-GaAs. Apart from the well-known surfactant behavior of Bi atoms for III-V growth at higher temperatures, there is experimental evidence that Bi enhances surface diffusion lengths even at these low T_s and that its presence significantly alters the step morphology from large terraces with relatively straight step edges in GaAs to smaller terraces with meandering step edges. Obviously, both effects, i.e., increased step density and enhanced adatom diffusivity are expected to have an impact on the surface kinetics, likely triggering the dramatic effect of ES barriers and promoting rapid roughening. Incidentally, there are recent reports on the presence of regularly distributed, elongated mound-like features on the surface of Ga(As,Bi) epilayers.

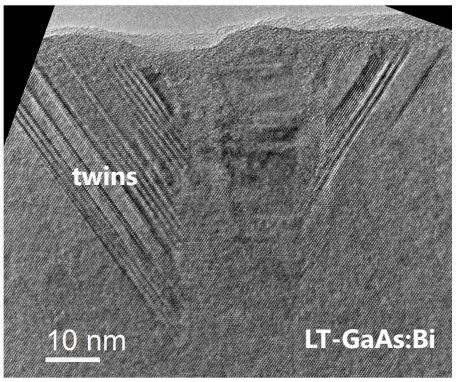

Fig. 4. Aberration-corrected TEM micrograph of representative twinned region with central defective cone. The microstructure closely resembles the one recurrently observed in LT-Si, LT-Ge, and LT-GaAs at the initial stages of breakdown of epitaxy.

Additionally, it is known that kinetic factors based on adatom surface diffusion and ES barriers seem to foster the creation of ordered domains. In this respect, although the driving force for ordering is the thermodynamics at the surface (via the surface reconstruction, in order to reduce reconstruction induced subsurface stresses), atomic ordering processes strongly rely on adatom attachment at steps and its dependence on adatom surface diffusion. Hence, Bi-induced (surface) kinetics effects, with Bi seemingly altering adatom diffusivity and attachment at step edges, play a key role in the resultant morphology and explain our experimental observations, including the development of V-shaped features eventually leading to a breakdown of epitaxy. The results presented here are predicted to be of general applicability to other dilute bismide compounds or highly-mismatched-alloys grown by LT-MBE.

Luminescence properties of $GaP_{1-x}N_x$ grown by chemical beam epitaxy: Correlation with growth conditions

J. Lähnemann, K. Ben Saddik,[1] B. J. García,[1] S. Fernández-Garrido[1]

The incorporation of small amounts of N into GaP induces an indirect-to-direct band gap transition, as described by the band anticrossing (BAC) model [W. Shan *et al.*, Appl. Phys. Lett. **76**, 3251 (2000)]. In addition, for a N mole fraction of $x = 0.021$, the ternary compound $GaP_{1-x}N_x$ has the same lattice parameter as Si and a direct band gap of 1.96 eV. Hence, $GaP_{1-x}N_x$ alloys are of interest for the monolithic pseudomorphic integration of III-V optoelectronic devices with the widespread and highly scalable Si technology – in particular for the fabrication of tandem solar cells or red light-emitting devices. Nevertheless, challenges in the synthesis of $GaP_{1-x}N_x$ alloys with high structural perfection have so far prevented the development of competitive devices.

In this work, we present a comprehensive and systematic study on the correlation between growth conditions and luminescence properties of $GaP_{1-x}N_x$ alloys prepared by chemical beam epitaxy (CBE) on state-of-the-art, nominally on-axis (001) GaP-on-Si substrates. CBE is an ultra-high-vacuum epitaxial growth technique characterized by the use of gaseous precursors in the form of molecular beams for both, group-III and group-V elements. The incorporation of N into the alloy was systematically investigated as a function of the substrate temperature and the fluxes of the N and P precursors 1,1-dimethylhydrazine (DMHy) and tertiary-butylphosphine (TBP), respectively. The 25-nm-thick GaP template layer is free of extended defects and possesses a smooth surface without anti-

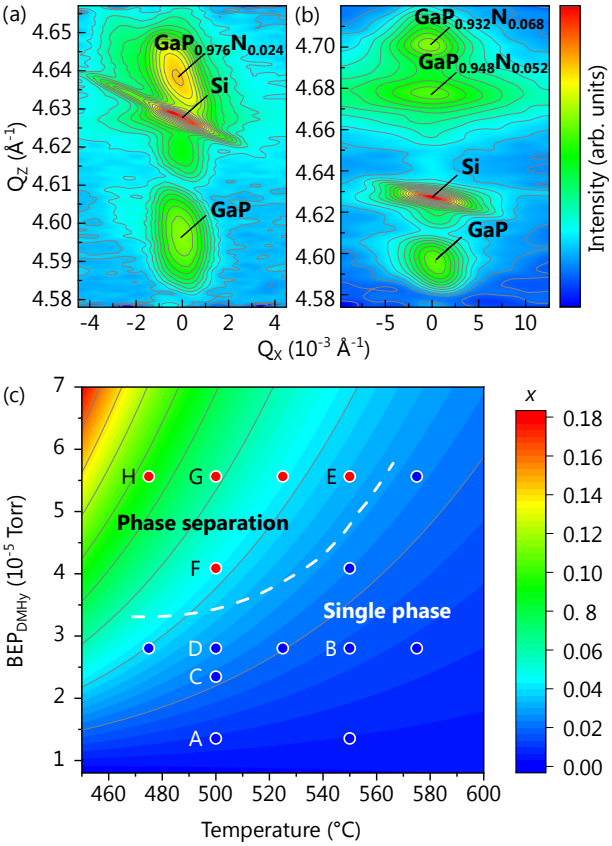

Fig. 1. (a)–(b) HRXRD reciprocal space maps around the symmetric 004 Bragg reflection of two representative $GaP_{1-x}N_x$ layers on a color-coded, logarithmic intensity scale. (c) Growth diagram depicting the dependence of the incorporation of N into $GaP_{1-x}N_x$ on the substrate temperature and the BEP of DMHy, which is directly proportional to its flux. The N mole fraction (x) is displayed on a color-coded, linear scale. The dashed line shows the boundary between single-phase and phase-separated $GaP_{1-x}N_x$ layers. The dots indicate the samples grown for this study, where the labels D and G correspond to the samples shown in (a) and (b), respectively.

[1]Electronics and Semiconductors Group, Applied Physics Department, Universidad Autónoma de Madrid, 28049 Madrid, Spain

phase domains. After desorbing the native oxide, a 15-nm-thick GaP buffer was grown, followed by the approximately 210-nm-thick $GaP_{1-x}N_x$ layers.

Figures 1(a) and 1(b) show two representative reciprocal space maps (RSMs) around the symmetric 004 Bragg reflection measured by high-resolution X-ray diffraction (HRXRD). For low N contents, a single peak associated with the $GaP_{1-x}N_x$ layer is observed [cf. Fig. 1(a)], while the observation of two clearly resolved, $GaP_{1-x}N_x$-related peaks in Fig. 1(b) reveals the occurrence of chemical phase separation. The latter comes along with a roughening of the sample surface (not shown). From such measurements, the growth diagram in Fig. 1(c) was compiled, which summarizes the dependence of the chemical composition of $GaP_{1-x}N_x$ alloys grown by CBE on the flux of the N precursor (DMHy) and the substrate temperature. The diagram holds for fixed beam equivalent pressure (BEP) values of the Ga and P precursors triethylgallium and TBP, respectively. The N content increases linearly with the DMHy flux, while it decreases exponentially with substrate temperature [Ben Saddik *et al.*, arXiv:2107.07848 (2021)]. All samples that contributed to the map are marked with a solid dot, while the samples investigated in more detail in this study are labeled alphabetically according to increasing N content. The samples in Fig. 1(c) are grouped by the occurrence of a single phase or phase separation of the alloy. The boundary between the two growth regimes is indicated by the dashed line. Note that for high DMHy fluxes the phase separation sets in already at lower N contents. Regardless of the growth conditions, the first atomic layers of $GaP_{1-x}N_x$ grow in a two-dimensional layer-by-layer fashion, as demonstrated by the observation of strong reflection high-energy electron diffraction intensity oscillations (not shown).

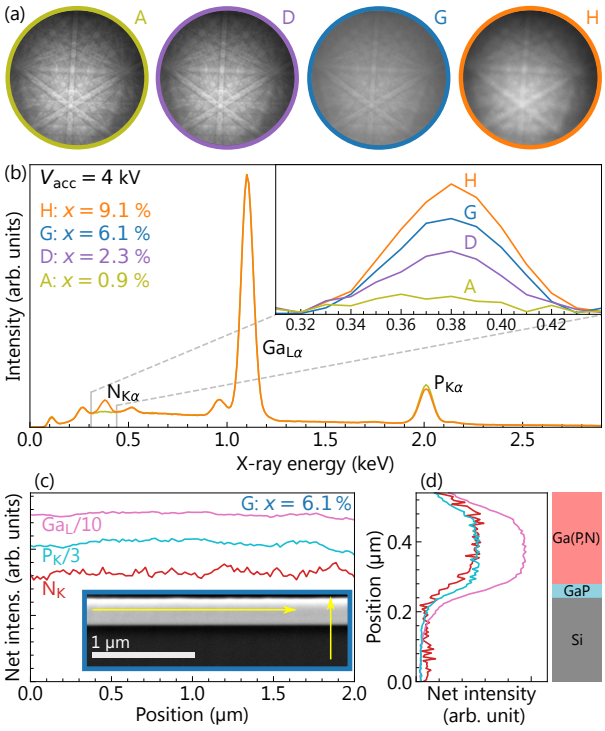

Fig. 2. (a) EBSD Kikuchi patterns of selected samples. (b) Representative EDX spectra of two $GaP_{1-x}N_x$ layers. The inset shows a magnification of the N_K peak for four samples. (c)–(d) Net peak intensities for EDX linescans along and across a polished cross section of sample G as indicated on the SEM image in the inset of (c). For a better comparison, the intensities have been scaled by the indicated factors. The sketch on the right-hand side of (d) illustrates the corresponding layer structure.

The crystal structure and structural quality of the samples can also be characterized by electron backscatter diffraction (EBSD) mapping in a scanning electron microscope (SEM). A homogeneous (001) out-of-plane orientation is confirmed on the microscopic level. However, for the phase-separated samples, the quality of the Kikuchi patterns

degrades with increasing N content. In Fig. 2(a), the single-phase samples A and D show a high pattern quality, in contrast to the phase-separated samples G and H. On the one hand, the phase separation on a nanoscopic level can lead to a distortion of the lattice that affects the pattern quality and leads to a blurring of the Kikuchi bands. On the other hand, the increased surface roughness may also contribute to the reduced pattern quality.

Tab. 1. Summary of the investigated samples ordered by increasing N content x (mean value) as determined by XRD and EDX. The central wavelength λ of the main peak, the full width at half maximum w, and the signal intensity I obtained from a double Gaussian fit (to account for the long wavelength shoulder), together with their standard deviation, obtained by averaging over hyperspectral CL maps are listed. Samples A–D are phase pure, while E–H exhibit a phase separation.

Sample	x_{XRD} (%)	x_{EDX} (%)	λ (nm)	w (nm)	I (counts)
A	0.7	0.9 ± 0.2	585.9 ± 0.2	27 ± 0.2	1990 ± 50
B	1.1	1.8 ± 0.3	601 ± 0.4	28.2 ± 0.3	1490 ± 60
C	1.6	2.1 ± 0.3	609.9 ± 0.5	35.4 ± 0.6	1420 ± 70
D	2.4	2.3 ± 0.3	631.7 ± 0.5	37.6 ± 0.6	720 ± 40
E	2.8	2.7 ± 0.4	637 ± 1	$(67 \pm 1)^{\dagger}$	320 ± 60
F	4.5	3.6 ± 0.5	649.5 ± 0.8	41 ± 1	$160 \pm 10^{*}$
G	6.0	6.1 ± 0.7	663 ± 5	57 ± 8	$1.2 \pm 0.4^{*}$
H	8.0	9.1 ± 0.9	665 ± 3	$(111 \pm 6)^{\ddagger}$	$1.2 \pm 0.2^{*}$

† fitted with a triple Gaussian, ‡ fitted with a single Gaussian
* scaled intensity due to longer exposure times

Both, the average N incorporation and the phase separation detected by HRXRD, were further investigated on a microscopic scale by SEM-based energy-dispersive X-ray spectroscopy (EDX). Figure 2(b) shows EDX spectra recorded over an area of 0.01 mm^2 for samples A and H (lowest and highest detected N content). The inset shows a magnification of the N peak including two intermediate samples. The compositions obtained from the EDX measurements are compiled in Table 1 and compared to those measured by HRXRD. The compositions show the same trend and generally a good agreement within the error margins of the EDX measurements. Deviations may be attributed to the measurement of different sample pieces and the smaller area over which the measurements average in the case of EDX. The composition of sample C indicates that it has the closest lattice match to the Si substrate. To further investigate the phase separation, a polished cross section of sample G was prepared by Ar-ion sputtering, an SEM image of which is displayed in the inset of Fig. 2(c). On this cross section, EDX linescans were measured in-plane and across the epitaxial layer stack with the net X-ray intensities (background removed) displayed in Figs. 2(c) and 2(d), respectively. The linescan along the $GaP_{1-x}N_x$ layer shows a constant composition. Due to the lower signal intensity, the N_K signal is more noisy than for the Ga_L and P_K lines, but the deviations are not sufficient to explain the phase separation on the order of more than 1.5 % (5.2–6.8 %) evidenced in the HRXRD RSM for this sample in Fig. 2(b). Similarly, the N signal does not show a trend or fluctuations when measuring across the $GaP_{1-x}N_x$ layer in Fig. 2(d). Thus, down to the resolution of EDX in an SEM on the order of a few tens of nm, the N content appears to be

constant. Therefore, these measurements need to be complemented by EDX measurements in a transmission electron microscope to further increase the spatial resolution, which might shed light on the nature of the phase separation.

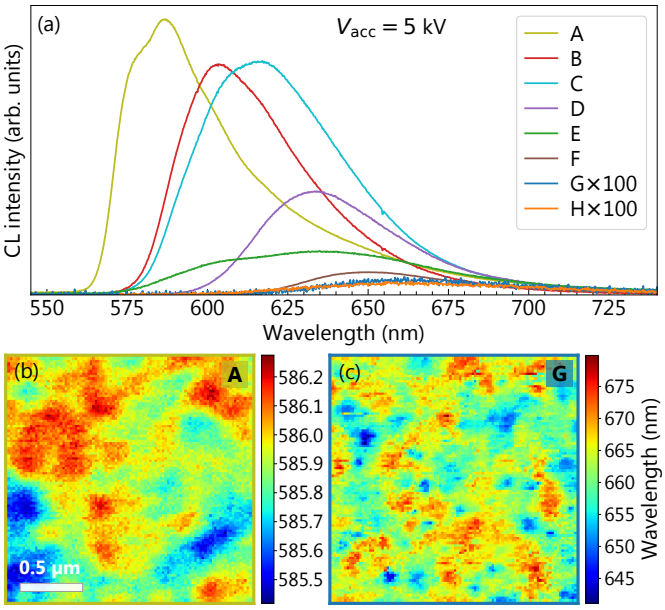

Fig. 3. (a) CL spectra integrated over hyperspectral maps of the samples recorded at 10 K. The intensities of G and H have been scaled by a factor of 100. (b) and (c) Emission wavelength of the main peak obtained from a double Gaussian fit to the hyperspectral maps for samples A ($x_{EDX} = 0.9\,\%$) and G ($x_{EDX} = 6.1\,\%$), respectively.

The luminescence properties of the samples were examined by cathodoluminescence (CL) spectroscopy in the same SEM. Measurements have been performed with a He cold stage at sample temperatures of 10 K. Spatially integrated CL spectra of the samples are presented in Fig. 3(a) and give an overview of the luminescence properties. For each sample, hyperspectral maps containing the emission spectra on a grid of 100×100 points with a 20 nm step size were acquired. The results from a statistical analysis of these maps are summarized in Table 1. The shift of the emission energy is well described by the BAC model up to the point where phase separation sets in. For higher N contents, it is smaller than expected from this model. The emission intensity remains high for compositions up to the lattice match (sample C) and is reduced for higher compositions and even more notably once the phase separation sets in (samples E–H). Similarly, the width of the emission peaks as well as the variation in emission energy and peak width are all notably larger for the phase-separated samples as compared with the phase-pure ones. The spatial fluctuations in the emission wavelength are visualized in Figs. 3(b) and 3(c) for samples A and G, respectively. The strong increase in these fluctuations with increasing N content is accompanied by a reduction of the length scale over which they occur from about 500 nm in sample A to 100–200 nm in sample G. This may be indicative of a reduced carrier diffusion length, since these variations are not correlated to any compositional fluctuations on these length scales as observed by EDX [cf. Fig. 2(c)]. Instead, carrier localization induced by nanoscopic compositional fluctuations and the presence of structural defects may also play a role for the emission properties of the latter samples.

In conclusion, it is feasible to grow $GaP_{1-x}N_x$ lattice matched to Si by CBE with a high crystal quality. Besides the structural properties, the optical properties are not degraded for low N content. However, once reaching the composition range at which phase separation sets in, a drastic decline of the emission properties is observed.

Determining the amplitude of surface acoustic waves using atomic force microscopy

J. Hellemann, F. Müller, M. Msall[1], P. V. Santos, S. Ludwig

Today, surface acoustic waves (SAW) are used in key technologies as miniature radio frequency filters, sensors, or for microscale control of fluids [P. Delsing *et al.*, J Phys. D Appl. Phys. **52**, 353001 (2019)]. Commonly, SAWs are generated, detected, and controlled by employing interdigital transducers. These are periodic arrays of metallic finger gates with a pitch of half the acoustic wavelength λ_{SAW}. Based on the piezoelectric effect, they convert resonant electrical signals into SAWs and vice versa and also function as Bragg mirrors for SAWs. Recent research aims at integrating SAWs into quantum technology, where high-quality phonon cavities that can harbor standing SAWs (SSAWs) at frequencies $f_{\mathrm{SAW}} > 1\,\mathrm{GHz}$ are called for. While the cavity spectrum can be detected using the electric response of the interdigital transducers, the detailed mode properties including amplitude and geometry of SAWs with $\lambda_{\mathrm{SAW}} < 1\,\mu\mathrm{m}$, corresponding to GHz frequencies, are much harder to measure. This knowledge would enable us to refine high-frequency SAW devices as needed for both, new classical and quantum applications. For sub-micron wavelengths, an atomic force microscope (AFM) might be used for imaging SAWs. However, the determination of the SAW amplitude from an AFM measurement is not straightforward due to the transfer of kinetic energy of the moving surface into potential energy of the cantilever tip. Commonly used cantilevers have resonance frequencies smaller than 1 MHz and cannot resolve in time SAWs with larger frequencies. In that case, a cantilever in contact mode can be treated as a slow oscillator driven by a much faster external periodic force. As a result, even if the AFM is configured in contact mode, the cantilever tip hovers above the surface modulated by an SAW and does not directly measure the SAW amplitude.

In Fig. 1(a), we present a scanning electron (SE) micrograph of the surface of our sample showing two Bragg mirrors, which shape a 100-μm-long focusing cavity for SAWs with a wavelength of $\lambda = 1\,\mu\mathrm{m}$. Connected to a radio frequency source, one Bragg mirror serves as an interdigital transducer to generate a SAW. In Fig. 1(b), we display a contact-mode, AFM line scan recorded in the center of the cavity as a function of the lateral cantilever tip position x and f_{SAW}. The lock-in measurement reveals several adjacent cavity modes of the SSAW. Such AFM scans provide information about the mode spectrum of the cavity and the quality factor, here $Q \simeq 3500$. The mode separation is $\delta f_{\mathrm{SAW}} = 12.5\,\mathrm{MHz}$ corresponding to an effective cavity length of $\lambda_{\mathrm{SAW}} f_{\mathrm{SAW}} \,/\, 2\delta f_{\mathrm{SAW}} \simeq 113\,\mu\mathrm{m}$. For all AFM measurements, we used a Bruker *Edge*.

To determine the actual SSAW amplitude, we recorded force curves with the tip of the AFM cantilever at the position of an antinode of an SSAW near $f_{\mathrm{SAW}} = 3\,\mathrm{GHz}$,

[1]Department of Physics and Astronomy, Bowdoin College, Brunswick, Maine 04011, USA.

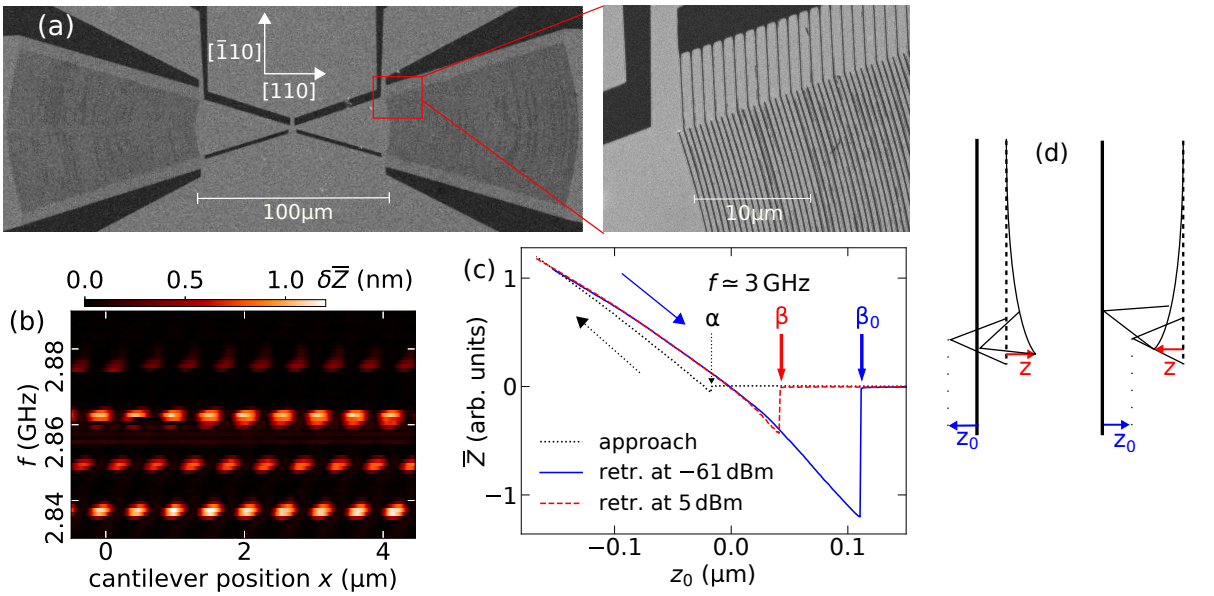

Fig. 1. (a) SE micrograph of the (001) surface (light gray) of a GaAs wafer partly covered with metal gates (dark gray). The blow-up shows the 250-nm-wide metal fingers at a pitch of 500 nm forming the two Bragg mirrors of an SSAW cavity oriented along the [110] crystal direction. (b) AFM contact-mode lock-in measurement of an SSAW in the center of the focusing cavity as a function of f_{SAW} and the position x along [110]. The SSAW power was modulated between $0 \leq P \leq 9$ dBm with a frequency of 250 Hz (P is the on-chip power after subtraction of cable losses, reflections, etc.). Color scale: $\delta\overline{Z}$ corresponds to the response caused by the SSAW of the time-averaged cantilever deflection $\overline{Z}$. (c) Measured force curves $\overline{Z}(z_0)$ for two different SSAW powers. The approach curves are identical. $z(t)$ corresponds to the momentary deflection of the cantilever and z_0 to the notional distance between surface and the tip for $z(t) = 0$. For practical reasons, we define $z_0 = 0$, where the retraction and approach curves cross at $\overline{Z} = 0$. To the right of $z_0 = \alpha$, β_0, and β, the cantilever tip is completely detached from the surface, $\overline{Z} = 0$. (d) Sketch of two relevant situations with the cantilever in contact for $R = 0$: the cantilever pulled towards the surface for $z_0 > 0$ or bent away from the surface for $z_0 < 0$.

while vertically moving the cantilever first from high above towards the surface (approach) and then back away from the surface (retraction). In Fig. 1(c), we present the time-averaged deflection $\overline{Z}$ of the cantilever (averaged over the resonant cantilever oscillations and many SSAW periods) as a function of its nominal vertical position z_0, defined in Fig. 1(d). During approach (dotted line) $\overline{Z} = 0$ until at $z_0 = \alpha$, the tip is pulled towards the surface. The solid line is the retraction curve at very low SSAW power, essentially without an SSAW. The difference between the approach and retraction curves for $z_0 < 0$ was interpreted in terms of a radial shirk of the cantilever [J. H. Hoh *et al.*, Langmuir **9**, 3310 (1993)], which unfortunately conceals the accurate interaction potential V between tip and surface. As a consequence, we instead map below a realistic model potential to our experimental results.

While the cantilever is further retracted for $z_0 > 0$, its tip stays connected to the surface such that $\overline{Z} < 0$, until at a height of $z_0 = \beta_0$ the spring force of the cantilever surpasses the attraction force and the cantilever flips back to stall at $\overline{Z} = 0$. The resulting deflection curve is characterized by a sizable triangle at negative deflection, quantified as β_0. This triangular hysteresis between approach and retraction curves indicates a competition between two stable solutions. The dashed line in Fig. 1(c) corresponds to

a retraction curve measured for a much larger SSAW power of $P = 5\,\mathrm{dBm}$. Strikingly, the strong SSAW yields a smaller $\beta < \beta_0$. The physical reason is a reduction of the attractive force between the cantilever tip and the surface, as the cantilever tip hovers above a surface modulated by an SAW. Below, we show, how the actual amplitude R of an SSAW can be determined from the measured $\beta(P)$.

The equation of motion of the cantilever is $m(\ddot{z} + \omega^2 z) = -V'\,[z + z_0 + R\cos(\Omega t)]$. Here $z(t)$ denotes the momentary cantilever deflection and V the a-priori unknown interaction potential. The cantilever is characterized by its force constant $m\omega^2 \simeq 0.32\,\mathrm{N/m}$ and its resonance frequency $f = \omega/2\pi \simeq 65\,\mathrm{kHz}$. The momentary distance between the tip and the surface is $z + z_0 + R\cos(\Omega t)$, where R denotes the amplitude of the SSAW and $\Omega/2\pi = f_{\mathrm{SAW}}$. Performing a separation of the corresponding time scales ($\Omega \gg \omega$) and expanding V' around both, $R = 0$ and the contribution to $z(t)$ oscillating with Ω, yields an estimate of the steady state average cantilever deflection

$$\overline{Z} = -\frac{V'(\overline{Z} + z_0)}{m\omega^2} + \delta\overline{Z}\,; \qquad \delta\overline{Z} = -\frac{V'''(\overline{Z} + z_0)}{4m\omega^2}\,\frac{m\Omega^2 - 3V''(\overline{Z} + z_0)}{m\Omega^2 - V''(\overline{Z} + z_0)}\,R^2\,. \qquad (1)$$

The prediction for the SSAW contribution, $\delta\overline{Z} \propto R^2$, is correct as long as $\delta\overline{Z} \propto P$ is fulfilled in the experiment. The solution of Eq. (1) describes the steady-state balance of the forces $-F_{\mathrm{cl}} \equiv m\omega^2\overline{Z} = -V'(\overline{Z} + z_0) + m\omega^2\delta\overline{Z} \equiv F_{\mathrm{i}}$, where F_{cl} denotes the cantilever spring force and F_{i} the interaction force between its tip and the surface.

From the force curve for $R = 0$ [cf. Fig. 1(c)], we can estimate the attraction between the tip and the surface at $z_0 = \beta = -\overline{Z}$ just before the cantilever detaches from the surface during retraction: $F_{\mathrm{i}}(\beta) = -F_{\mathrm{cl}}(\beta) = -m\omega^2\beta \simeq -40\,\mathrm{nN}$ points to interatomic forces holding the tip at the surface. We fitted such a potential introduced for Ge [J. Tersoff, Phys. Rev. B **39**, 5567 (1989)] to our measured data as described below. It was sufficient to reduce the attractive contribution of the original Tersoff potential by 1.9 %, expressing the strong similarities between GaAs and Ge. In Fig. 2(a), we present the interaction force $F_{\mathrm{i}} = -\partial V/\partial z$ for $R = 0$ (solid line) as a function of the tip-surface distance $z + z_0$, where V denotes the optimized Tersoff potential, together with $-F_{\mathrm{cl}}$ for three different values of z_0 (broken lines). Note that $\overline{Z} = z(t)$ for $R = 0$. The intersection points $F_{\mathrm{i}} = -F_{\mathrm{cl}}$ are the solutions of Eq. (1). Depending on the value of z_0, up to three solutions coexist, of which only two are stable. Stable fixed points are indicated by open symbols: triangles for the cantilever tip detached from the surface with $z \simeq 0$ and circles for the cantilever in contact with the surface. The dashed line 1 for $z_0 = 50\,\mathrm{nm}$ presents the case of three solutions. Triangles mark the occupied fixed point during approach and circles the ones during retraction. Lines 2 and 3 indicate the situations for $z_0 = \alpha = 0.3\,\mathrm{nm}$ and $z_0 = \beta = 120\,\mathrm{nm}$, respectively. For $z_0 < \alpha$ during approach and $z_0 > \beta$ during retraction, the only remaining solution is the yet unoccupied fixed point, explaining the abrupt change of $\overline{Z}$ at $z_0 = \alpha$ and $z_0 = \beta$.

We fit our model to the measured $z_0 = \beta$, where exactly two solutions exist and not

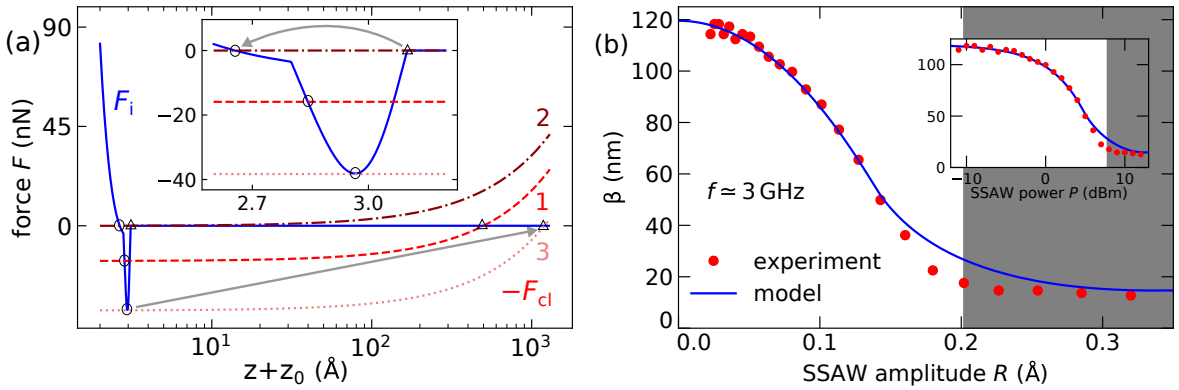

Fig. 2. (a) Interaction force F_i (solid line) derived from the optimized Tersoff potential for $R = 0$ and negative cantilever spring force $-F_{cl}$: line 1 for $z_0 = 50\,\text{nm}$, line 2 for $z_0 = \alpha = 0.3\,\text{nm}$ and line 3 for $z_0 = \beta = 120\,\text{nm}$. Stable fixed points are indicated by open symbols as described in the text. The inset shows a blow-up near the minimum of F_i. (b) Cantilever position at detachment $\beta(R)$ (symbols) as determined from the measured $\beta(P)$ in the inset in comparison with the model prediction (lines).

only the forces are equal, i.e., $F_i = -F_{cl}$, but also their derivatives $F_i' = -F_{cl}' = m\omega^2 = 0.32\,\text{N/m}$. Our model prediction $\delta\overline{Z} \propto R^2$ in Eq. (1) corresponds to $R = \sqrt{P/C}$ in the experiment. To determine C, we iteratively adjust both, the parameters of the Tersoff potential as well as C itself, until we find the best overall fit within the range of validity of our model. In the inset of Fig. 2(b), we present the measured values of β (symbols) as a function of P, while the main figure shows the final result for $\beta(R)$. It provides a calibration, which can be used to determine the SSAW amplitude R, e.g. for a given cantilever deflection. The solid lines are the model curves $\beta(R)$ determined from Eq. (1) using the optimized Tersoff potential. The fitted conversion factor is $C = 123\,\text{mW/Å}^2$. For $R > 0.2\,\text{Å}$ corresponding to $P > 8\,\text{dBm}$ [shaded regions in Fig. 2(b)], we begin to observe non-linear effects in our measurements, and $P \propto R^2$ is no longer valid. At these large powers, the actual values of R can be reduced compared to those shown in Fig. 2(b). The overall agreement between our measured data and the model curve is excellent for $R < 0.2\,\text{Å}$. The cantilever deflection in contact mode [cf. Fig. 1(b) for $P = 5\,\text{dBm}$] is in our measurements 50 times larger than the actual SSAW amplitude.

In summary, one directly measures with AFM the average deflection of the cantilever $\overline{Z}$. For an SAW with a frequency exceeding the resonance frequency of the cantilever by far, $\overline{Z}$ can be orders of magnitude larger than the actual amplitude R of the SAW. The solution of the equation of motion describes $\overline{Z}(R)$, which is proportional to R^2 and depends on the derivatives of the interaction potential. Because the accurate interaction potential is unknown, we iteratively fit a suggestive model potential to the measured relation between the SSAW power P and a length scale β, which is related to a jump between two stable solutions. In this way, it is possible to reliably calibrate the actual amplitude R of an SSAW using AFM force curve measurements.

The authors thank F. von Oppen for fruitful discussions and C. Hermann, W. Anders, and A. Tahraoui for technical support.

Charge storage at 77 K in metal-chalcogenide junctions

Y. Takagaki

It is a familiar scene of a chilly winter: a car will not start because the battery is dead. People know from such daily-life experiences that conventional secondary batteries do not work well at icy temperatures. The operating temperature range of the famous lithium-ion batteries is -20 to 60 °C, where the low-temperature limit arises from the reduction of the ionic conductivity in the electrolytes. In this work, bilayer junctions consisting of a metal and a metal-chalcogenide are revealed to be capable of storing electrical charges. Remarkably, the storage capacity increases as the temperature is lowered from room temperature to 77 K by orders of magnitude. Although the charge storage presented in this work would never be competitive with existing batteries, the storage excels at cryogenic temperatures, where the conventional batteries have no chance of doing the required task.

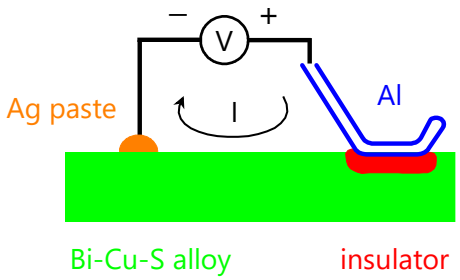

Fig. 1. Al/Bi-Cu-S bilayer junction. An Al wire was pressed to the Bi-Cu-S film by means of ultrasonic bonding. The solids reacted with each other spontaneously, giving rise to the formation of an insulating layer at the interface. The *I-V* characteristics were obtained by applying a voltage V to the Al lead with respect to an ohmic contact of the Bi-Cu-S film prepared using silver paste.

The structure of the charge storage device is illustrated in Fig. 1. The construction is simple. Merely an Al wire having a diameter of 25 μm was attached to the film of a Bi-Cu-S alloy by means of ultrasonic wire-bonding. The wire was pressed to form an Al electrode having an expanded width of about 100 μm and a length of several hundred μm. When the alloy is in contact with Al, an electrical isolation layer is produced spontaneously at the junction interface. This chemical reaction between the solids takes place even at room temperature and is responsible for the charge storage. Chalcogens such as S belong to the oxygen family of the periodic table. The spontaneous reaction is the oxidation process of the metal. The insulating layer can be dissolved electro-chemically. In fact, this property leads to a resistance switching phenomenon as shown below. These oxidation and reduction processes are the underlying mechanism in the device operation. Therefore, the Al/Bi-Cu-S junctions act like a solid-state chemical factory.

The Bi-Cu-S film was synthesized in vacuum by exposing a Cu film, which was deposited on a Si substrate, to the vapor of Bi_2S_3 at a high temperature. The Bi atoms in Bi_2S_3 were replaced in part by the Cu atoms. The material substitution reaction thus gave rise to a synthesis of the Bi-Cu-S alloy. The composition and the crystal structure of the Bi-Cu-S alloy varied with the synthesis temperature T_s. Nevertheless, the charge storage was observed regardless of T_s, at least, in the range of $T_s = 250$ to 500 °C.

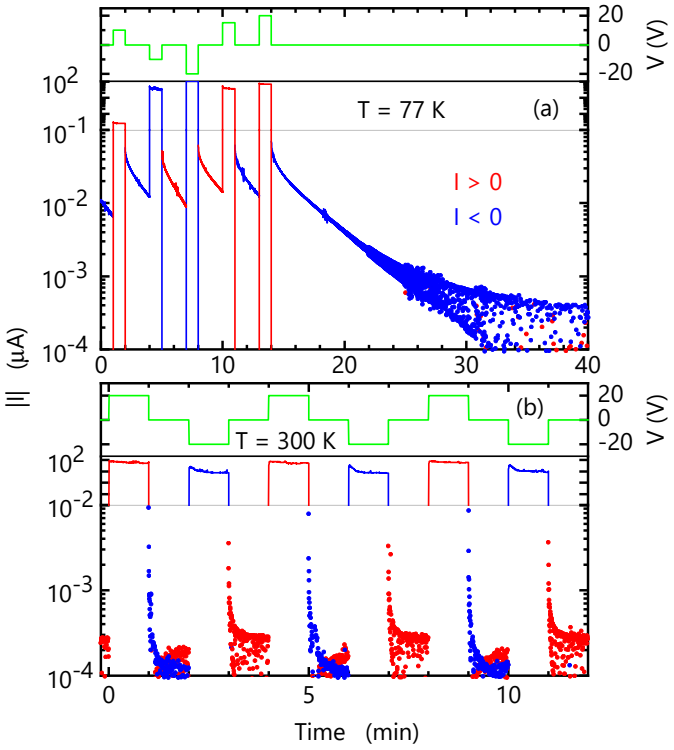

Fig. 2. Storing electrons in Al/Bi-Cu-S junction. The time evolution of the current I is shown when the voltage bias V applied to the junction was varied step-wise as shown by the green curves. The operating temperature T was set to (a) 77 K and (b) room temperature. As the absolute value $|I|$ is plotted, positive and negative values of I are distinguished by the red and blue curves, respectively. Note that the current did not exactly decay to zero due to the current generated by the offset voltage of the source measure unit. The vertical scale is changed at (a) 10^{-1} and (b) 10^{-2} μA for clarity.

In Fig. 2, the bias V applied to the Al/Bi-Cu-S junction was varied step-wise as shown by the green curves. The flow of the current I was then monitored. One finds that the current did not vanish when the bias was set from finite values abruptly to zero. Following the application of $V = 20$ V for 1 min in the example of Fig. 2(a), the current fell below the detection limit (about 0.4 nA) nearly half an hour after the bias was turned off, i.e., the current decayed by two orders of magnitude in 30 min. The charge release corresponds to storing electrons with a density of about 10^{21} m^{-2} in the electrode area. The dependences of the amplitude and the decay characteristics of the discharging current on the polarity and the strength of the charging bias were insignificant. The charge storage polarity was hence invertible.

The measurement shown in Fig. 2(a) was performed at a temperature $T = 77$ K, since the charge storage was enhanced by reducing T. Figure 2(b) shows that the effect was recognizable also at room temperature. Here, the release current from the junction was examined when charging biases of ± 20 V were applied for 1 min using alternating polarities. The discharge current was a few orders of magnitude smaller in amplitude at room temperature in comparison to the one at $T = 77$ K. The current thus vanished in less than 1 min. Nevertheless, the characteristic reversal in the polarity of the current between the charging and discharging processes is noticed.

It is emphasized that conventional batteries such as lithium- and aluminum-ion batteries cannot operate at temperatures such as 77 K as the ionic conduction freezes out. The operation of the present device does not rely on the ionic charge transport. Battery systems that utilize elements other than Li, such as Na, Mg, and Al, have attracted rapidly increasing attention in recent years as post-lithium energy storage systems. Given Al being the most abundant metal element in the Earth's crust, a rechargeable battery based on aluminum chemistry could be a low-cost system. In addition, Al-

based batteries are attractive due to the fact that the energy storage capacity of Al is one of the highest among all elements.

In the remainder of this report, let us turn our attention to the resistance switching phenomenon. Although the Bi-Cu-S film itself exhibited metallic conduction, the resistance of the Al/Bi-Cu-S junction became high as a consequence of the blocking of the current by the spontaneously generated interface barrier. The insulating compounds of the barrier were dissolved electro-chemically when the bias of an appropriate polarity was applied to the junction. The disappearance of the barrier resulted in an abrupt decrease of the junction resistance in its bias dependence.

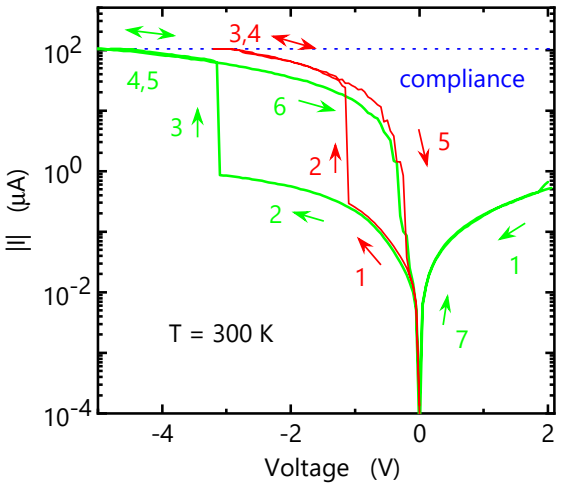

Fig. 3. Interfacial resistance switching in Al/Bi-Cu-S junction at room temperature. Two resistance switching cycles are shown by the red and green curves. The numbered arrows show the sequence of the voltage sweeps with the sweep direction. Note that the measurements of the current were restricted by the compliance of the source measure unit, which is indicated by the blue dotted line.

In Fig. 3, two examples of the resistance switching behavior are shown as the red and green curves. The bias was varied in the sequences indicated by the numbered arrows. The small initial current when V was varied from 0 to -3.2 V in the red curve was due to the existence of the interface barrier. The bias-induced annihilation of the barrier gave rise to an abrupt increase of $|I|$ at $V = -1.1$ V as indicated by the red arrow 2. The absence of the barrier continued until its spontaneous regeneration, which occurred when V was changed to be around zero. Therefore, the switching behavior was repeated with the bias being varied between a large negative value and about zero. In comparison to conventional resistance switching, the high-resistance state is realized spontaneously without applying a *set* voltage in the interfacial resistance switching.

Interestingly, the voltage at which the resistance switching takes place can be altered by applying a reverse bias prior to triggering the switching. As manifested in the green curve in Fig. 3, the switching voltage shifted to -3.1 V when the bias sweep started from 2 V. With respect to the charge storage phenomenon presented above, this manipulation of the switching voltage is driven by the charges stored at the Al/Bi-Cu-S interface, i.e., the charge storage and the interfacial resistance switching are closely related to each other. Note that the Al/Bi-Cu-S junctions work as memristive devices as demonstrated above. The unique properties of the interfacial resistance switching may be utilized for improving the performance of artificial neural networks constructed by memristors. Artificial intelligence such as machine learning may also benefit from it.

Drastic effect of sequential deposition resulting from flux directionality on the luminescence efficiency of nanowire shells

H. Küpers, R. B. Lewis, P. Corfdir, M. Niehle, T. Flissikowski, H. T. Grahn, A. Trampert, O. Brandt, L. Geelhaar

The chamber geometry of a system for molecular beam epitaxy (MBE) is known to affect technical aspects such as the macroscopic deposition homogeneity across a wafer. However, for the microscopic mechanisms governing the growth of thin films on a planar substrate, the chamber geometry does not play any role. Conceptually, a different situation arises for the growth of compound shells around nanowires standing perpendicularly on the substrate. Due to the directional nature of the deposition in MBE and self-shadowing by the nanowire core, a nanowire sidewall facet is exposed at a given moment in time only to molecular beams from cells with free line of sight onto this facet. Substrate rotation leads to a subsequent exposure of this sidewall facet to all open cells. Consequently, the deposition of the constituents is inherently sequential, and the azimuthal arrangement of the cells in the MBE chamber is decisive for the deposition sequence. Here, we show that the luminescence efficiency of (In,Ga)As/GaAs shell quantum wells (QWs) grown around GaAs nanowires changes by more than two orders of magnitude depending on the relative position of the As cell compared to the group-III cells due to the resulting differences in the deposition sequences.

The core-shell structure of the nanowires under investigation is schematically depicted on the left-hand inset of Fig. 1(a). A 10-nm-thick $In_{0.15}Ga_{0.85}As$ shell QW was grown around a GaAs nanowire core with a diameter of 50 nm and covered with an outer GaAs shell of 30 nm thickness. The right-hand inset is a representative scanning electron micrograph of an ordered nanowire array used here. The NWs of the two samples that will be compared in the following exhibit a similar morphology. Both samples were grown by MBE using the same growth conditions. The only difference between the two growth protocols is the choice of the As cell for the shell growth.

The photoluminescence (PL) spectra of these two samples presented in Fig. 1(a) show severe differences. The spectrum of the sample grown with cell As2 is dominated by an intense band at 1.37 eV associated with emission from the shell QW. In contrast, the PL intensity of the As1 sample is more than two orders of magnitude smaller. Furthermore, this spectrum consists of sharp lines in the spectral range 1.30 to 1.40 eV. We interpret these sharp lines as emission from excitons localized in the minima of potential fluctuations in the shell QW. Both, the lower PL intensity and the broad band of sharp lines, indicate a much lower photogenerated charge carrier concentration in the As1 sample. Since light coupling is identical for the two samples, the difference between the integrated PL intensities reveals directly that the internal quantum efficiency must be more than two orders of magnitude lower in this sample.

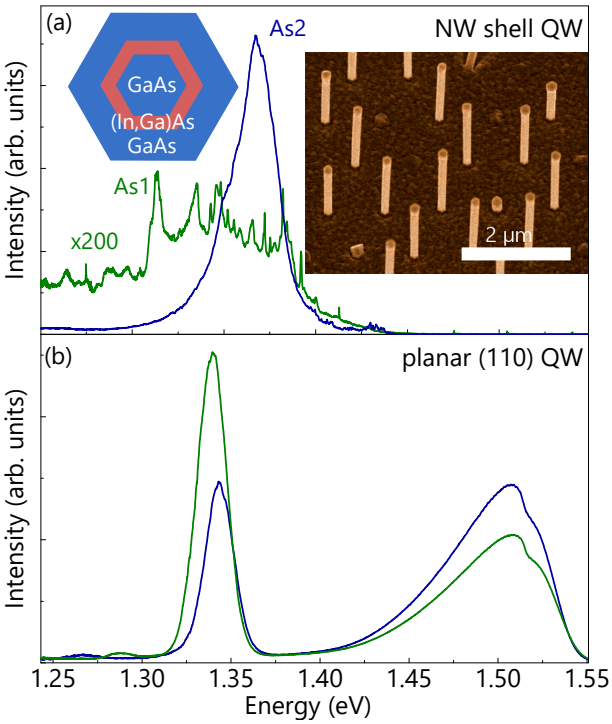

Fig. 1. Comparison of PL spectra recorded at 10 K of the nanowire and planar $In_{0.15}Ga_{0.85}As$ QWs grown with different As cells: (a) Core-shell nanowires grown with As cell As1 (green curve) and As2 (blue curve). The insets show the core-shell structure of the samples and a representative scanning electron micrograph of a nanowire array under investigation, tilted by 25° from the normal. (b) Planar (110) QW samples with a structure equivalent to the shells of the nanowire samples grown with As cell As1 (green curve) and As2 (blue curve).

Figure 1(b) depicts PL spectra of two planar reference samples containing an $In_{0.15}Ga_{0.85}As$ QW with the same thickness as the shell QW of the NW samples. In order to mimic the shell QWs as closely as possible, we used GaAs(110) substrates, which are of the same crystallographic orientation as the NW sidewall facets. The QWs of these two samples were grown using the same growth conditions as for the QWs in the NW samples, and the only difference between the two samples was again the choice of the As source. In marked contrast to the NW samples, these spectra are very similar and show an intense band at 1.34 eV as well as a broader, weaker band around 1.50 eV. The first band can be assigned to the $In_{0.15}Ga_{0.85}As$ QW. The second broader band corresponds to luminescence from the *n*-type GaAs substrate. The similarity in the PL spectra of the two planar samples rules out a possible contamination of one of the As sources as a reason for the drastic difference in the PL intensity between the two NW samples.

The only difference between the two identical As sources is their location in the MBE system, which is shown in Fig. 2(a). The direction of the impinging fluxes relative to a given NW sidefacet can be characterized by the azimuthal angle α and the polar angle β [cf. Fig. 2(b)]. The angle α varies continuously during substrate rotation. The fluxes impinging on one sidefacet calculated as a function of time are presented in Fig. 2(c) for using cell As1 and in Fig. 2(d) for using cell As2. In both sequences, the Ga and In fluxes overlap widely due to the cells' location next to each other. Using cell As1, there is also a large overlap of the As flux with the In and Ga fluxes. In contrast, for cell As2, there is no overlap of the As and In fluxes due to the opposite location of the cells to each other. Consequently, using cell As1, all constituents are mostly co-deposited, whereas for using cell As2, As and In are never co-deposited. The flux modulation with sequential group-III and As deposition resembles the one that is used for migration enhanced epitaxy (MEE) of planar films. In that case, cell shutters are opened and closed such that the group-III and group-V fluxes impinge

after each other on the substrate, with the aim to increase the diffusion of the group-III adatoms [Y. Horikoshi *et al.*, Jpn. J. Appl. Phys **27**, 169 (1988)].

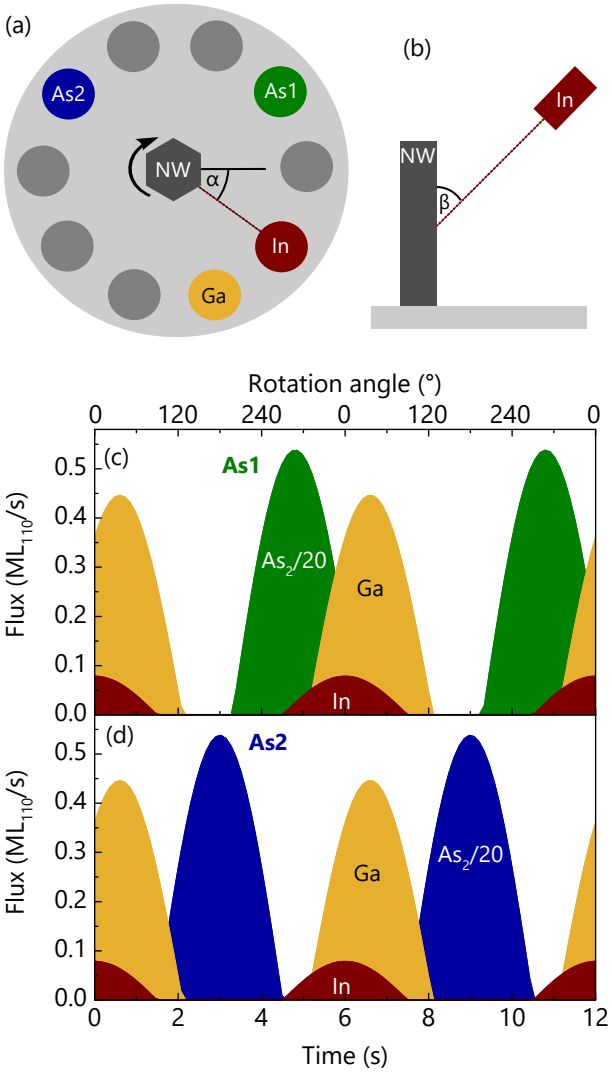

Fig. 2. (a) Schematic of the cell configuration of the MBE system used for this study as seen from the top. (b) Schematic of the flux impinging on the nanowire sidewall as seen from the side. (c,d) Calculated material fluxes impinging on a given nanowire side facet as a function of time and rotation angle using (c) cell As1 and (d) cell As2 for the experimental rotation speed of 6 rpm.

The investigation of the As1 sample by transmission electron microscopy showed that the shell QW is coherent and elastically strained, and we did not find any indication of dislocations. Thus, the low luminescence efficiency of this samples is not caused by extended defects.

In order to identify the physical origin of the reduced luminescence efficiency for co-deposition, we carried out time-resolved PL measurements. Figures 3(a,b) display streak camera images obtained upon pulsed excitation at 10 K for the two nanowire samples. In both cases, the QW emission is detected at about 1.42 eV, i. e., at roughly 50 meV higher energy as compared to the emission obtained with continuous-wave excitation [cf. Fig. 1(a)]. This blueshift is a result of the higher photoinduced carrier concentration for pulsed excitation and the entailing saturation of localized states. The most obvious difference between the samples is the time scale of the decay. To quantify this difference, we spectrally integrated the respective emission band and analyzed the resulting PL transients as shown in Fig. 3(c). In addition to the drastically different decay kinetics, which reflects the participation of non-radiative processes in the recombination, the peak intensity of the transients differs significantly. Since the two samples are basically identical in terms of nanowire diameter and pitch, the peak intensity is directly related to the radiative rate, i. e., the inverse radiative lifetime $\tau_{F,\mathrm{r}}$ of the free exciton.

For the As2 sample, we analyzed the experimental transient with a coupled rate equation system for free and bound excitons used previously for similar samples [H. Küpers *et al.*, Phys. Status Solidi RRL **13**, 1800527 (2019)], which is visualized in the inset of Fig. 3(c). The fit returns the time constants $\tau_c = 0.56$, $\tau_e = 1.18$, $\tau_F = 0.34$,

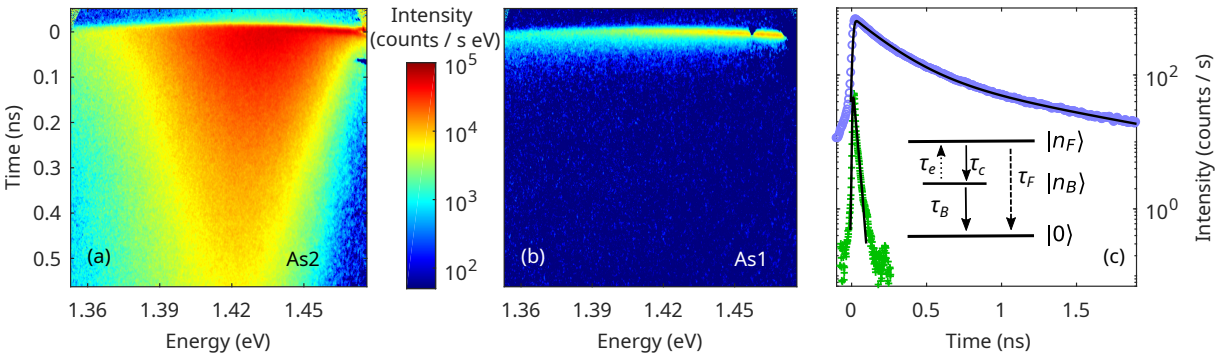

Fig. 3. Analysis of the PL decay at 10 K for the two nanowire samples. (a,b) Streak camera images of the nanowires grown with cells (a) As2 and (b) As1. (c) Transients of the PL intensity extracted from the data presented in (a) (blue symbols) and (b) (green symbols) by integrating across the entire spectral range. The lines are fits employing for the upper curve a coupled rate equation system for free and bound excitons and for the lower curve a monoexponential decay. The inset depicts an energy level scheme visualizing the coupled free ($|n_F\rangle$) and bound ($|n_B\rangle$) exciton states involved in the radiative decay to the ground state $|0\rangle$.

and $\tau_B = 1.58$ ns, with τ_c and τ_e characterizing the coupling of the two exciton states and the effective lifetimes τ_F and τ_B of free and bound excitons, respectively. Taking the radiative lifetime $\tau_{F,\mathrm{r}} = 1.3$ ns of the free exciton as deduced in the above reference and assuming that the effective lifetime is lower due to an enhanced nonradiative contribution, we obtain a minimum nonradiative lifetime of $\tau_{F,\mathrm{nr}} = 0.46$ ns for the As2 sample. In comparison, the initial decay time found for the As1 sample amounts to 10 ps.

In principle, nonradiative recombination at the large surface could explain this drastic difference. However, in the above reference, we showed that at 10 K the outer GaAs shell presents a sufficiently high barrier for charge carriers to suppress this channel. Thus, a higher density of deep point defects acting as non-radiative recombination centers is the most likely explanation for the much shorter nonradiative decay time of the sample grown with cell As1. In addition, the peak intensity of this sample is reduced by an order of magnitude, i. e., the radiative lifetime exceeds 10 ns. Such an excessively long radiative lifetime for a free exciton in a QW clearly suggests the presence of substantial electric fields in the QW, decreasing the electron-hole wave function overlap and thus the radiative rate. Most probably, such fields result from the incorporation of electrically active shallow point defects such as carbon in combination with radial surface band bending due to Fermi level pinning at the nanowire sidewalls.

In conclusion, a high PL intensity is obtained for $In_{0.15}Ga_{0.85}As$ shell QWs around GaAs nanowires only for a flux sequence corresponding to MEE, i. e., when As and the group-III metals essentially do not impinge at the same time. Our sample structure is a model system for optically active nanowire shells, and we expect that our findings generally hold for compound nanowire shells. We emphasize that the azimuthal cell arrangement is in this context of extraordinary relevance, but difficult to change between growth runs.

Cross-sectional shape of MBE-grown GaN nanowires on Si(111): Small-angle x-ray scattering and transmission electron microscopy study

V. Kaganer, O. Konovalov,[1] R. Volkov,[2] N. Borgardt,[2] O. Brandt, S. Ferńandez-Garrido[3]

GaN nanowires (NWs) differ from planar GaN epitaxial films in two essential points: they provide the reduction of the lattice defects due to the ability of free elastic relaxation of the material near the interface to the substrate and a large area of side facets. Various applications of GaN NWs, such as gas sensors or solar water splitting, make use of the side facets and essentially depend on their crystallographic orientation. It is commonly accepted in the NW community that the side facets are the GaN$\{1\bar{1}00\}$ planes, which are prominently observed in the top view scanning electron micrographs. High-resolution transmission electron microscopy revealed also rounded corners between $\{1\bar{1}00\}$ facets (O. Brandt *et al.*, Cryst. Growth Design **14**, 2246 (2014)]. On the other hand, numerous *ab initio* calculations, from which we cite only few [J. E. Northrup and J. Neugebauer, Phys. Rev. B **53**, R10477 (1996); D. Segev and C. G. Van der Walle, Surf. Sci. **601**, L15 (2007); H. Li *et al.*, Phys. Rev. Lett. **115**, 085503 (2015)], give close values for the surface energies of $\{1\bar{1}00\}$ and $\{11\bar{2}0\}$ facets. These values are about 100 meV/Å^2 or slightly above, with the $\{1\bar{1}00\}$ surface energy lower than that of the $\{11\bar{2}0\}$ surface by about 5 meV/Å^2. A Wulff construction based on these values gives rise to the equilibrium crystal shape with the ratio of the areas of the $\{11\bar{2}0\}$ and $\{1\bar{1}00\}$ facets of about 0.5.

Small angle x-ray scattering is a powerful tool to study sizes and shapes of the ensembles of nanoparticles and is not affected by their internal structure. In the previous annual report (2020) we have reported its application to GaN NWs [V. Kaganer *et al.*, Acta Cryst. A **77**, 42 (2021)]. In this former study, the cross-sectional shape of NWs has been modeled by hexagons possessing only $\{1\bar{1}00\}$ facets. In the present report, we extend the analysis to gain more detailed information on the cross sections of NWs.

In the present study, we use the samples of GaN NWs grown on Si(111) by molecular beam epitaxy from a series of samples grown in identical conditions for different times. This series allowed us to reveal the NW bundling during their growth [V. Kaganer *et al.*, Nano Lett. **16**, 3717 (2016)]. Figure 1 presents by gray lines grazing incidence small angle x-ray scattering (GISAXS) intensities from two samples with GaN NWs on Si(111). The lengths of the NWs are 230 nm in Figs. 1(a) and 1(b) and 650 nm in Figs. 1(d) and 1(e), respectively. Since the GISAXS intensity $I(q_x)$ (where x axis is along the substrate surface in the direction normal to the incident x-ray beam) follows at large q_x Porod's law $I(q_x) \propto q_x^{-4}$, the product $I(q_x)q_x^4$ is plotted. Red broken lines

[1]ESRF, Grenoble, France
[2]National Research University of Electronic Technology—MIET, Moscow, Russia
[3]now at Universidad Autónoma de Madrid, Madris, Spain

are the results of our former study. They present Monte Carlo simulations that assume NW cross sections as distorted hexagons. These simulations adequately reproduce scattering intensity in the direction of the normal to the $\{1\bar{1}00\}$ facets (facet truncation rods) at the orientations of 0° and 60°, but give too low intensity in the direction of the NW edges, at the orientation of 30°. Hence, we improve the model with the aim to properly describe the scattering intensity in the direction of the edges between $\{1\bar{1}00\}$ facets.

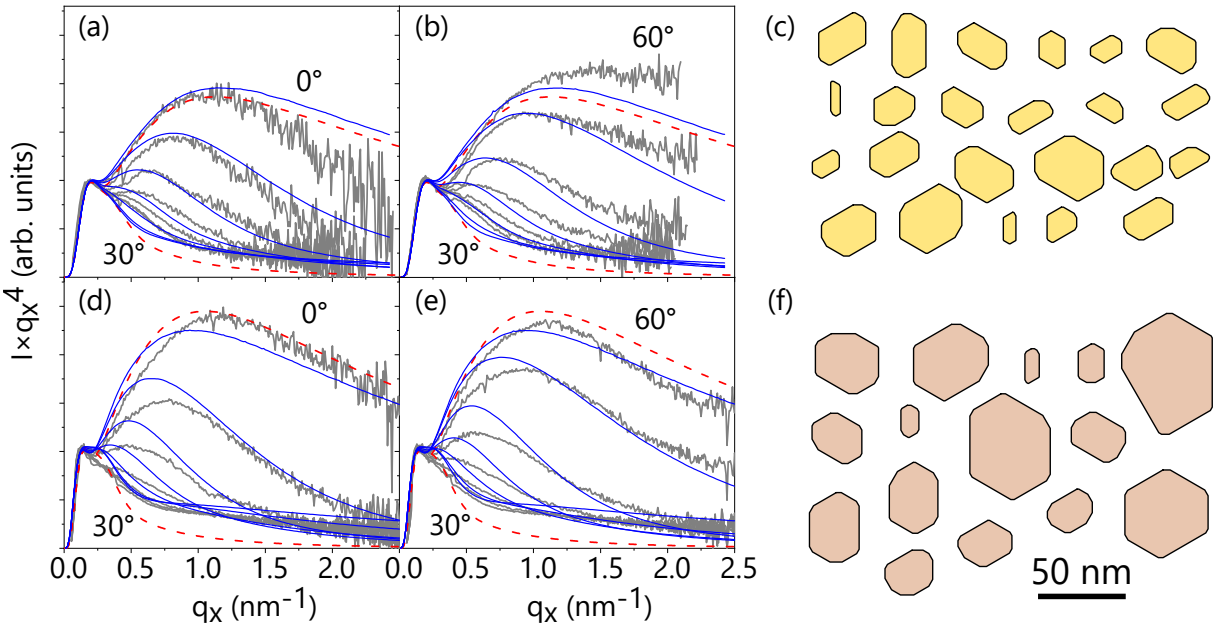

Fig. 1. GISAXS intensity from samples with NW arrays of the average NW length (a), (b) 230 nm and (d), (e) 650 nm (gray lines). The intensity curves are obtained at different azimuthal orientations of the samples from 0° to 60° with a step of 5°. Red dash lines show Monte Carlo simulations assuming hexagonal cross-sectional shape of NWs. Blue lines are the results of the Monte Carlo simulation presenting the cross-sections as dodecagons with both $\{1\bar{1}00\}$ and $\{11\bar{2}0\}$ sides. Simulations reveal a 1° misalignment of the samples with respect to the NW facets and profiles at nominally 5° and 55° are thus not equivalent. Examples of the NW cross sections used in the simulations of the two samples are presented in (c) and (f), respectively.

For this purpose, we model the cross sections of NWs by hexagons with the vertices that are cut to represent the $\{11\bar{2}0\}$ facets. Hence, the cross-sectional shape, instead of a hexagon (a polygon with six vertices), is a dodecagon (a polygon with twelve vertices). Figures 1(c) and 1(f) exemplify the cross-sectional distributions in the Monte Carlo simulations of the two samples. Since the scattering amplitude of an arbitrary polygon is expressed through coordinates of the vertices, the simulations are performed in the same way as in the former study. The simulated GISAXS intensity curves for the two samples are shown in Figs. 1(a), 1(b) and 1(d), 1(e) by blue curves. The curves for the orientation of 30°, i.e., the $\{11\bar{2}0\}$ facet truncation rods, are now close to the experimental curves. The root-mean-squared (rms) roughness of the side facets for the two samples is found from the Monte Carlo simulations to be 0.7 and 0.8 nm, respectively. These values are less than 3 times the height of the atomic step on the $1\bar{1}00$ facet.

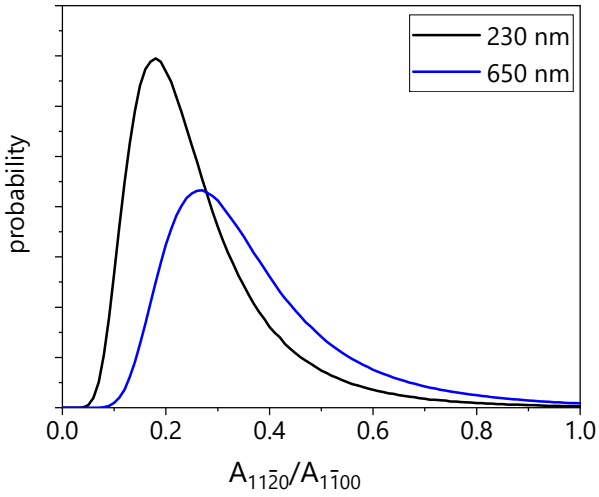

Fig. 2. Distributions of the ratios of the areas of the $\{11\bar{2}0\}$ and $\{1\bar{1}00\}$ facets obtained in the Monte Carlo simulations of the GISAXS intensities. The NW distributions obtained in the simulations are exemplified in Figs. 1(c) and 1(f).

Figure 2 presents the distributions of the ratio of the areas of the $\{11\bar{2}0\}$ and $\{1\bar{1}00\}$ side facets of NWs obtained in the Monte Carlo simulations. The average ratios are 0.26 and 0.37 for the two samples. Hence, the NWs of a larger length are more roundish, as one also can directly see from comparison of Figs. 1(c) and 1(f). We recall that the ratio of the side facet areas that follows from Wulff construction based on the *ab initio* calculations is about 0.5. Hence, the cross-sectional shape of NWs tend to the expected equilibrium shape. We note here that GISAXS intensity is an average over whole volume of NWs, so that both the top and the bottom parts of longer nanowires contribute to the GISAXS signal. One can also see from Figs. 1(c) and 1(f) that the longer NWs possess larger cross-sectional areas and a wider area distribution. The NW radii of the two samples (defined as a radius of the circle with the same area) obtained in the Monte Carlo simulations are 11.5 ± 3.6 and 18.0 ± 7.2 nm, where the first number is the mean radius and the second is the standard deviation.

Figure 3 presents high-angle annular dark-field (HAADF) scanning electron microscopy (STEM) micrographs of the samples equivalent to the ones studied by GISAXS. In the course of the TEM specimen preparation, the space between NWs was filled by a mix of platinum nanoparticles and amorphous carbon (Pt, a-C). The NWs are recognized as compact regions with almost homogeneous or monotonically varied intensity. The TEM specimens are prepared at the same distance of about 200 nm from the substrate, i.e., they correspond to the top parts of the shorter NWs and the bottom parts of the longer NWs.

Figures 3(a) and 3(b) reveal the same size and shape transformation of NWs with the increasing growth time as the snapshots of the NW distributions in Figs. 1(c) and 1(f) obtained in the Monte Carlo simulation of the GISAXS intensity: the NWs become larger, posses a broader size distribution, and become more roundish. The development of the $\{11\bar{2}0\}$ oriented parts of the surface is evident from a comparison of Figs. 3(c) and 3(d).

Thus, Monte Carlo simulation of the GISAXS intensities and the TEM micrographs show that, during NW growth, their cross-sectional shape transforms to develop $\{11\bar{2}0\}$ facets in addition to the $\{1\bar{1}00\}$ ones and tend to the equilibrium crystal shape that follows from the Wulff construction with the *ab initio* calculated surface energies.

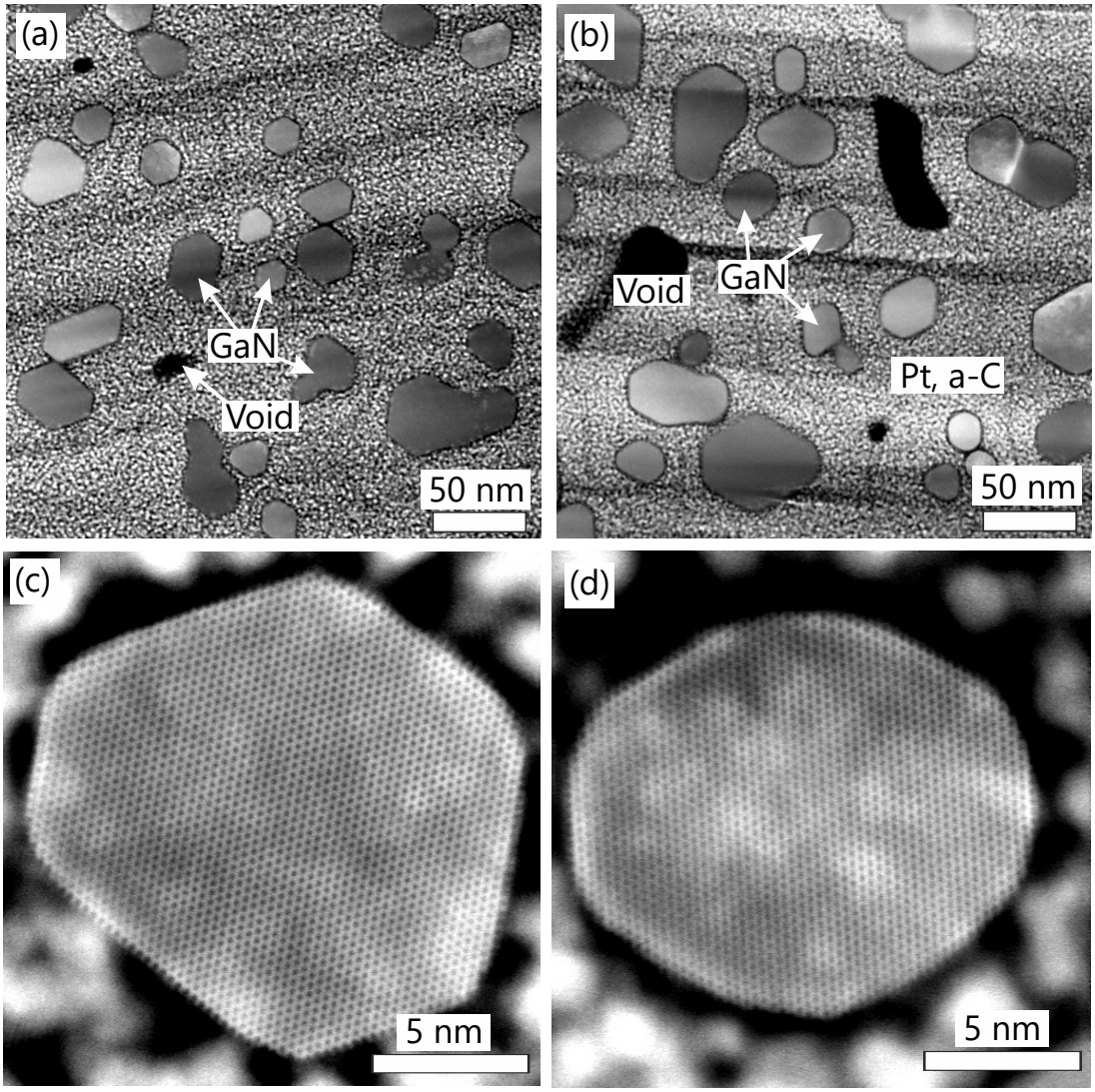

Fig. 3. HAADF STEM micrographs of GaN NWs of (a), (c) 230 and (b), (d) 650 nm in length. The cross sections are taken at the same distance of about 200 nm from the substrate.

Anisotropic spin-acoustic resonance in silicon carbide at room temperature

A. Hernández-Mínguez, A. V. Poshakinskiy[1], M. Hollenbach[2,3], P. V. Santos, G. V. Astakhov[2]

Hybrid spin-mechanical systems are promising platforms for the implementation of universal quantum transducers and ultra-sensitive quantum sensors. Similarly to a radio frequency (RF) magnetic field, the application of a resonantly oscillating strain field induces interlevel transitions for spin control. Their selection rules are imprinted by the crystal symmetry and device geometry, which provide a high degree of flexibility for on-chip coherent spin manipulation. In this contribution, we demonstrate spin control in silicon carbide (SiC) at room temperature by means of spin-acoustic resonance (SAR). Specifically, we use high-frequency vibrations to manipulate the half-integer $S = 3/2$ spin of the negatively charged silicon vacancy (V_{Si}) center. Figure 1(a) displays a schematic representation of our spin-acoustic structure. An ensemble of V_{Si} centers is created at a mean depth of 250 nm below the surface of a semi-insulating 4H-SiC substrate by proton irradiation. The mechanical vibrations are applied via a surface acoustic wave (SAW) resonator consisting of a pair of focusing interdigital transducers (IDTs) patterned on the surface of a piezoelectric ZnO film. Figure 1(b) displays the RF scattering (S) parameters of the IDTs measured using a vector network analyzer. They show a series of sharp dips (S_{11}, S_{22}) and peaks (S_{21}) within the resonance band of the IDTs at a frequency $f_{SAW} \approx 916$ MHz, which correspond to the excitation of the Rayleigh SAW modes of the resonator.

The optically detected SAR experiments are performed in a setup for confocal microphotoluminescence (PL), where the sample is excited by a 780-nm-wavelength laser focused onto a spot size of 10 μm at the center of the SAW resonator. The spin transition frequencies are tuned to the SAW frequency by applying an in-plane magnetic field $\mathbf{B}$. Figure 1(c) shows the Zeeman shift of the spin sublevels. Optical excitation followed by spin-dependent recombination via metastable states leads to a preferential population of the $m_S = \pm 3/2$ spin sublevels indicated by the green dots. As the PL intensity is stronger for the $m_S = \pm 1/2$ states (see light bulbs next to each spin sublevel), the PL intensity is sensitive to the resonant spin transitions between the $m_S = \pm 1/2$ and $m_S = \pm 3/2$ sublevels. The optically detected SAR as a function of B is presented in Fig. 1(d). We observe two resonances at $B = 16.7$ and 33.3 mT, which are ascribed to the acoustically driven $\Delta m_S = \pm 2$ and $\Delta m_S = \pm 1$ spin transitions, respectively. Both resonances are well fitted by a Lorentzian function [solid curves in Fig. 1(d)] centered at the magnetic field strengths expected for the resonance frequency f_{SAW} [cf. double

[1]Ioffe Physical-Technical Institute, Russian Academy of Sciences, 194021 St. Petersburg, Russia
[2]Helmholtz-Zentrum Dresden-Rossendorf, 01328 Dresden, Germany
[3]Technische Universität Dresden, 01062 Dresden, Germany

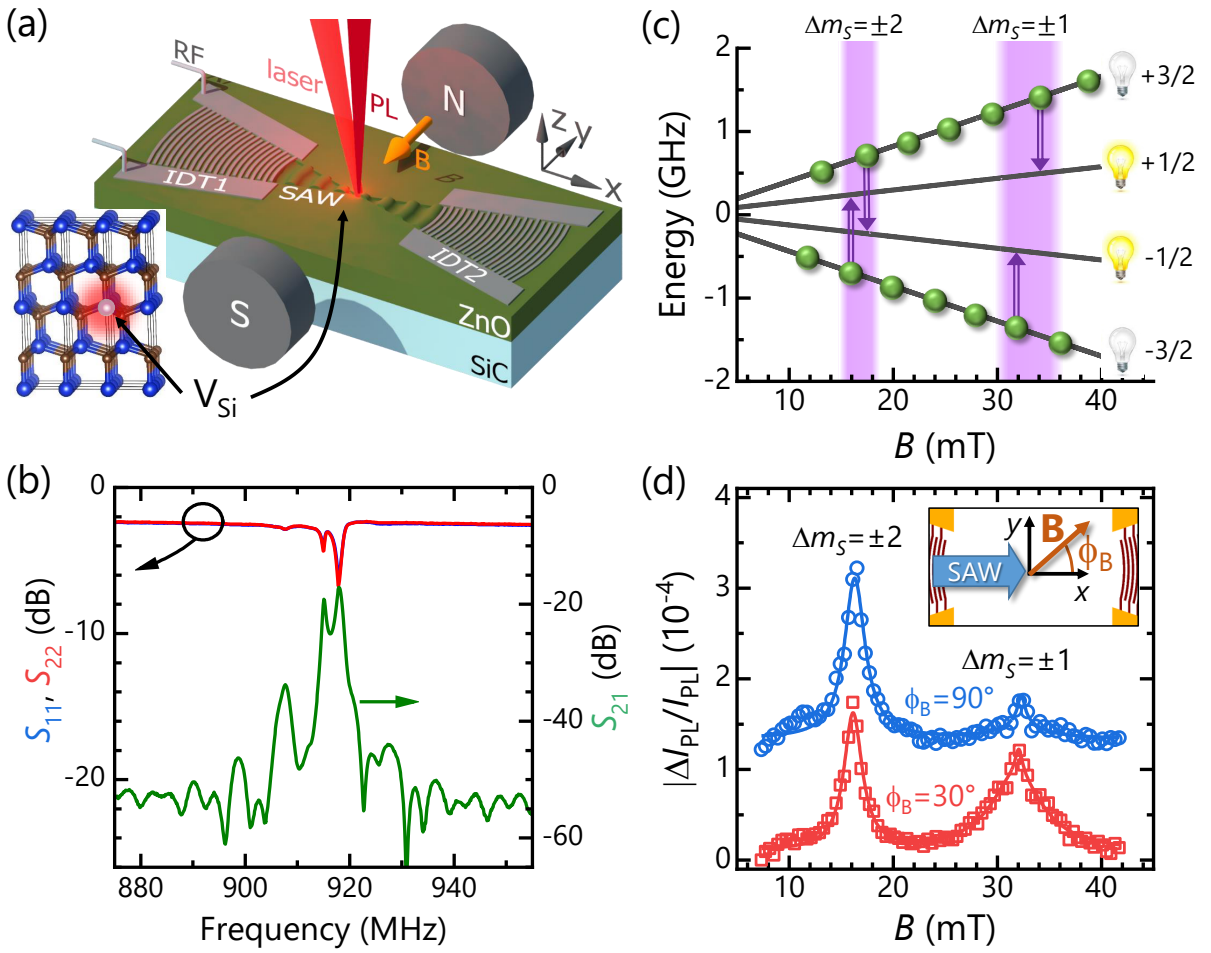

Fig. 1. (a) Focusing interdigital transducers (IDTs) excite and detect SAWs propagating in a ZnO-coated 4H-SiC sample hosting a V_{Si} ensemble. The poles of an electromagnet apply an in-plane magnetic field **B**. The inset shows a schematic representation of the 4H-SiC lattice with one V_{Si}. (b) RF power reflection coefficients of IDT_1 (S_{11}) and IDT_2 (S_{22}) as well as the power transmission coefficient S_{21}. (c) Dependence of the V_{Si} spin sublevels on B. The vertical double arrows indicate the resonant spin transitions induced by the SAW. (d) The SAR signal as a function of B for two magnetic field angles (ϕ_B) with respect to the SAW propagation direction (see inset). The solid curves are fits to a multi-peak Lorentzian function. The data are vertically shifted for clarity.

vertical arrows in Fig. 1(c)]. A remarkable property of the SAR interaction illustrated in Fig. 1(d) is the ability to selectively excite $\Delta m_S = \pm 1$ as well as $\Delta m_S = \pm 2$ transitions. In particular, the $\Delta m_S = \pm 2$ transitions are normally forbidden for RF-driven spin resonances. Therefore, their excitation in Fig. 1(d) represents clear evidence of the acoustic nature of the observed resonances.

We now discuss the anisotropic nature of the SAR. Figure 1(d) compares the optically detected SAR signal for two angles ϕ_B between the SAW propagation direction and **B**. While the magnetic field strengths at which the SARs take place are independent of ϕ_B, the SAR intensities do clearly depend on it. The full anisotropic behavior of the SAR intensity is summarized by the circles in Figs. 2(a) and 2(b) for the $\Delta m_S = \pm 1$ and $\Delta m_S = \pm 2$ SARs, respectively. The solid lines show the angular dependence of the spin transition rates $W_{\pm 1}$ and $W_{\pm 2}$ predicted by our microscopic model [A. Hernández-

Mínguez *et al.*, Phys. Rev. Lett. **125**, 107702 (2020)] for the spin-acoustic interaction, given by

$$W_{\pm 1} \propto 3\cos^2\phi_B\langle u_{xx}^2 \sin^2\phi_B + u_{xz}^2\rangle \tag{1}$$

$$W_{\pm 2} \propto \frac{3}{4}\langle (u_{xx}\sin^2\phi_B - u_{zz})^2 + 4u_{xz}^2\sin^2\phi_B\rangle\,. \tag{2}$$

Here, u_{xx}, u_{zz}, and u_{xz} are the non-vanishing strain components within the SAW resonator and the brackets $\langle\rangle$ indicate averaging along z to take into account the depth distribution of the V_{Si} ensemble as well as the strain field. The angular dependence of the $\Delta m_S = \pm 1$ SAR has a butterfly-like shape with vanishing signal for $\phi_B = \pm 90°$ and maxima when the magnetic field rotates towards $\phi_B \approx \pm 45°$ or $\pm 135°$. In contrast, the angular dependence of the $\Delta m_S = \pm 2$ SAR has a cocoon-like shape with maxima for $\phi_B = \pm 90°$. We attribute the deviations between experimental data and theoretical predictions to fluctuations in the position of the laser spot on the SAW path as the sample is rotated during the measurement.

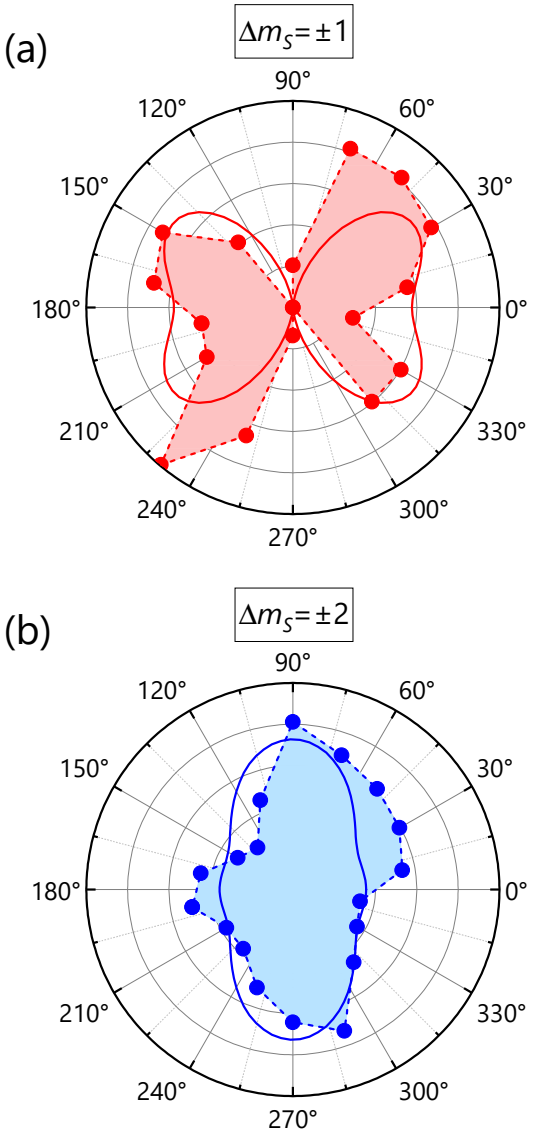

Fig. 2. Angular (ϕ_B) dependences of the (a) $\Delta m_S = \pm 1$ and (b) $\Delta m_S = \pm 2$ transition intensities. Circles represent the experimental data, the thin dashed lines are guides to the eye. The thick lines show the results of a calculation according to Eqs. (1) and (2).

In conclusion, we observe spin-acoustic resonances in SiC at room temperature. Using an SAW resonator patterned on the SiC surface, we are able to optically address both the $\Delta m_S = \pm 1$ and the $\Delta m_S = \pm 2$ spin transitions of the V_{Si} spin-3/2 center without requiring extra microwave electromagnetic fields. The SARs reveal a complex dependence on the magnetic field orientation with respect to the SAW propagation direction. Such a room temperature hybrid spin-mechanical platform can be used to implement quantum sensors with compact on-chip SAW control as well as to realize acoustically driven topological states. It can be also applied to implement microwave-free spin and optical control of single quantum memories in SiC.

High-reflectivity back-facet coating for improved operating parameters of terahertz quantum-cascade lasers

B. Röben, X. Lü, L. Schrottke, K. Biermann, H. T. Grahn

The operating parameters of terahertz (THz) quantum-cascade lasers (QCLs) such as threshold current density, maximum output power, and maximum operating temperature are determined by both, the optical gain of the active medium and the losses of the resonator. While the optical gain and its dependence on the applied current and operating temperature of the active medium are affected by the actual design and the thermal properties of the laser mount, the resonator losses are determined by the waveguide parameters and the mirror reflectivity. For the development of THz QCLs with optimum operating parameters, in particular with respect to the operating temperature, the optical gain has to be increased, and the resonator losses have to be reduced. Here, we investigate the effect of a high-reflectivity back-facet coating on the operating parameters of THz QCLs.

Steady-state lasing is achieved when the modal gain Γg, i.e., the mode confinement factor Γ multiplied by the material gain g, equals the resonator losses. At threshold, we may write

$$\Gamma g_{\mathrm{th}} = \frac{1}{2L} \ln\left(\frac{1}{\sqrt{R_f R_b}}\right) + \alpha_{\mathrm{wg}} \tag{1}$$

with L denoting the resonator length, R_f and R_b the reflectivity of the front and back facet, respectively, and α_{wg} the waveguide losses. The reflectivity of the uncoated facets is estimated to be about 0.3 for our lasers. If now R_b can be increased to a value of about 1 by deposition of a high-reflectivity coating on the back facet, the threshold gain and hence the threshold current density can be significantly reduced. This effect is expected to be larger for shorter resonator lengths and/or lower waveguide losses.

For an estimation of the possible maximum output power by a coating of the back facet, we have to take into account that the photon flux Φ inside the resonator and also the gain is not constant. We have to solve the following differential equations

$$\begin{aligned} \frac{d\Phi^+(x)}{dx} &= \left[\Gamma g(x) - \alpha_{\mathrm{wg}}\right] \Phi^+(x) \\ \frac{d\Phi^-(x)}{dx} &= -\left[\Gamma g(x) - \alpha_{\mathrm{wg}}\right] \Phi^-(x) \end{aligned} \tag{2}$$

inside the laser cavity between 0 and L with the boundary conditions $\Phi^+(0) = R_f \Phi^-(0)$ and $\Phi^-(L) = R_b \Phi^+(L)$. The total photon flux $\Phi(x) = \Phi^+(x) + \Phi^-(x)$ is the superposition of the forward and backward traveling fluxes $\Phi^+(x)$ and $\Phi^-(x)$, respectively. Within our model for the transport and optical properties of QCL structures, g can be determined as a function of Φ so that the position-dependent gain can be calculated by $g(x) = g[\Phi(x)]$, while Eqs. (**??**) can be solved by a standard numerical approach.

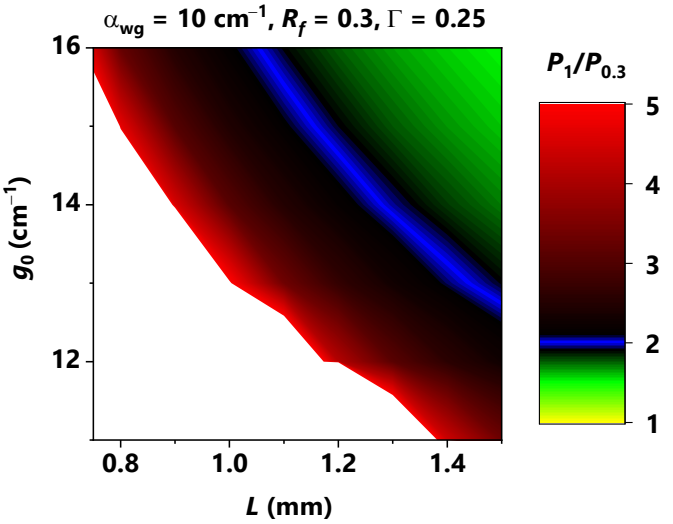

Fig. 1. Calculated values for the ratio of the output power P_1 for a back-facet reflectivity of 1 (coated facet) and the output power $P_{0.3}$ for a back-facet reflectivity of 0.3 (uncoated facet) as a function of L and g_0 for the set of given resonator parameters. The white area corresponds to the operating range of the uncoated laser below threshold.

Figure ?? shows an example for the simulated enhancement of the output power by implementing a high-reflectivity back-facet coating as a function of resonator length and idler gain g_0, which denotes the gain of the active medium without the influence of the resonator. The idler gain represents basically the applied current density, since g_0 is approximately a linear function of the current density. The numerical results clearly show that the enhancement is stronger for shorter cavities and lower idler gain/current density values. The latter means that the effect of the back-facet coating is strongest for operation at higher temperatures or near threshold (for low pump powers), when g_0 is rather small.

To experimentally investigate the effect of high-reflectivity back-facet coatings, we first mounted a laser with an uncoated back facet and determined its temperature-dependent output power-current density-voltage (L-I-V) characteristics. After the laser was demounted, the back facet was coated with a 120-nm-thick SiO_x insulating layer, a 10-nm-thick Ti layer, and a 50-nm-thick Au layer. The laser with the coated back facet was again mounted, and the L-I-V characteristics was measured. During the deposition of the SiO_x and metal layers, the surface of the QCL chip, i.e., the two contacts and the side facets, should not be contaminated by the deposited materials. Therefore, a special mount was developed, which protects the surface. Furthermore, we found that the remaining gold balls from the original bonding make the rebonding easier.

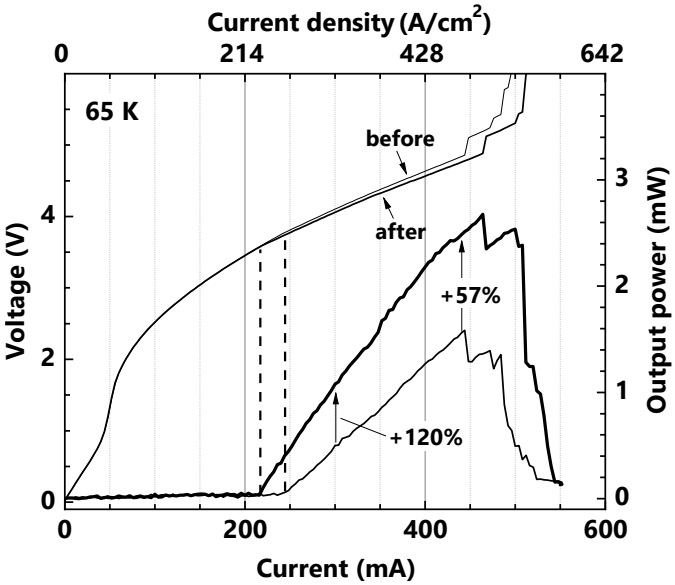

Fig. 2. L-I-V characteristics for a QCL emitting at about 3.9 THz in continuous-wave operation in a Stirling cooler. The thin lines mark the results of the uncoated QCL, while the thick lines refer to the QCL with a back-facet coating. The cavity length of the QCL is 0.78 mm.

Figure ?? shows the L-I-V characteristics for a prototypical QCL emitting at about 3.9 THz. As indicated by the vertical dashed lines,

the reduction of the mirror losses by increasing the back-facet reflectivity results in a shift of the threshold current from about 240 to 215 mA, which can be expected from the discussion of Eq. (**??**). Furthermore, we found a substantial increase of both, the optical output power and the slope efficiency. While at a driving current of about 450 mA the relative change is about 57 %, at 300 mA an enhancement of 120 % is obtained. Interestingly, the effect of the back-facet coating is also visible in the *I-V* curve. Above the threshold current for the coated laser, the additional output power is related to an increased current. Below this threshold, both *I-V* curves are identical, which confirms that the electrical properties of the QCL have not changed due to the coating process.

The higher enhancement at lower driving currents, i.e., lower idler gain, is in good qualitative agreement with the calculated results shown in Fig. **??**. Similarly, the relative increase of the output power at the driving current for maximum output power increases with increasing operating temperatures (not shown here). For example, we found values of 35 %, 55 %, and 135 % for 40, 60, and 70 K, respectively.

Since the effect of the high-reflectivity back-facet coating is rather large for operating conditions with low gain, e.g. at higher operating temperatures, we expect that this approach can contribute to a significant improvement of the practical operating temperature T_{po}, i.e., the operating temperature at which the QCL provides a continuous-wave output power of at least 1 mW under practical operating conditions. As a preliminary result, Fig. **??** shows the estimated T_{po} values for our prototypical QCL. For the uncoated laser, a value between 66 and 69 K is found, while it is close to 72 K after coating the back facet. We expect that a systematic investigation of the effect of back-facet coating for various resonator configurations will lead to a significant improvement of the T_{po} value. Higher operating temperatures are important for many applications, where the necessary cooling of the lasers remains a challenge. Together with the new designs (cf. contribution of X. Lü), the back-facet coating may also lead to the development of THz QCLs with T_{po} values towards 100 K, which is important for passive cooling required for satellite-based heterodyne spectrometers for astronomy.

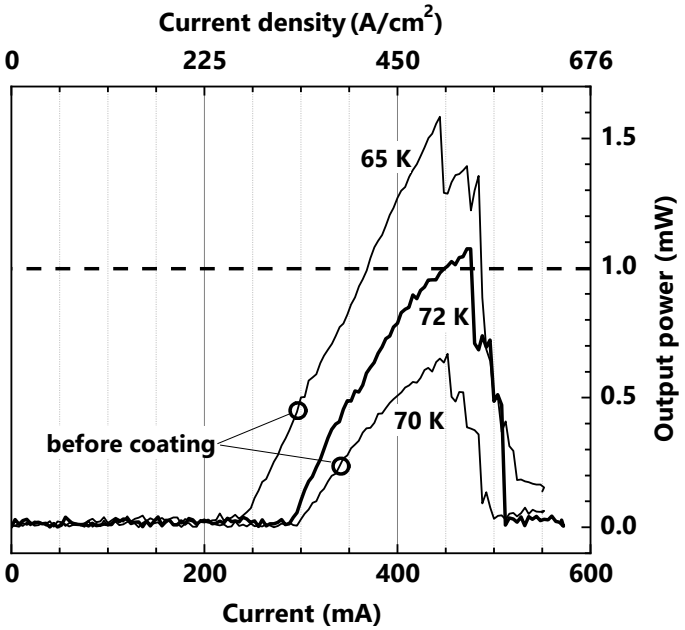

Fig. 3. *L-I* characteristics for the 3.9-THz QCL for continuous-wave operation in a Stirling cooler at various operating temperatures as indicated. The thin lines mark the results of the uncoated QCL, while the thick line refers to the QCL with a back-facet coating.

Terahertz quantum-cascade lasers for operation at low pump powers

X. Lü, B. Röben, L. Schrottke, K. Biermann, H. T. Grahn

GaAs/AlAs terahertz (THz) quantum-cascade lasers (QCLs) based on the hybrid design are promising sources for high-resolution absorption spectroscopy due to their relatively high wall plug efficiency and large tuning range despite the necessary operation at cryogenic temperatures. For applications of THz QCLs, for instance to pump the mixer in a heterodyne receiver, the optical output power is an important operating parameter, which typically has to be at least 1 mW for continuous-wave (cw) operation. Therefore, we defined a practical operating temperature T_{po} at which an output power of 1 mW is still obtained in cw mode. To increase the T_{po} value, designs with high optical gain at elevated temperatures are required. Since T_{po} depends also significantly on the interplay of the thermal properties of the lasers with the electrical pump power, a reduction of the pump powers of the QCLs can result in higher operating temperatures. Furthermore, low pump powers are beneficial for the operation of THz QCLs at limited available cooling powers or with long resonators for frequency comb applications with a very small mode spacing.

Based on our established hybrid design, we developed a new active region by including an additional quantum well (QW) as shown in Fig. 1. This QW contains another transition, which is quasi-resonant to the energy of the longitudinal optical (LO) phonon (E_{LO}), but is somewhat detuned to lower energies ($E < E_{\mathrm{LO}}$) so that only electrons in the upper state with larger momentum values can be scattered at LO phonons. Therefore, a certain electron *cooling* is expected due to the reduced momentum or kinetic energy E_{kin}. At the same time, the ground state of this additional QW leads to an extension of the sequence of states with increasing subband energies from the doped QW to the QW with the laser levels. We believe that the carrier transport through this shallow stairs supported by electron-electron scattering will result in a conversion of kinetic into potential energy ($E_{\mathrm{kin}} \Rightarrow E_{\mathrm{pot}}$) and hence in an additional carrier *cooling*. The operation at lower electrical field strengths and reduced leakage currents due to the increased length of the period may also contribute to a reduction of the pump power.

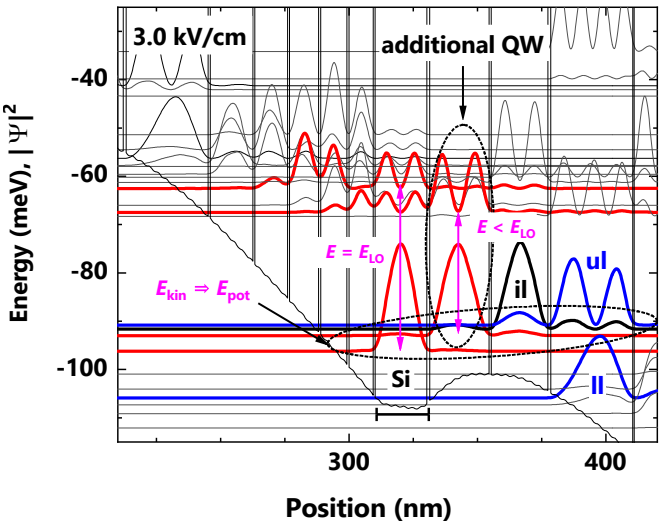

Fig. 1. Conduction band profiles, subband structure, and positions of the Si doping for the design of a low-input power QCL operating at about 3.5 THz and at an applied field strength of 3.0 kV/cm (ul: upper laser level, ll: lower laser level, il: injector level).

For this design, we realized a QCL using the GaAs/AlAs materials system by molecular beam epitaxy (MBE). The Fabry-Pérot ridge QCLs are based on single-plasmon waveguides and operated in a mechanical cryocooler. We mounted two lasers from the same wafer with different laser ridge dimension, QCL A with 0.12×2.032 mm^2 and QCL B with 0.08×10.011 mm^2. In order to determine T_{po} and the temperature-dependent pump power, we measured the light output-current density-voltage (L-J-V) characteristics at different temperatures. Figure 2 shows the L-J-V characteristics for several operating temperatures of QCL A.

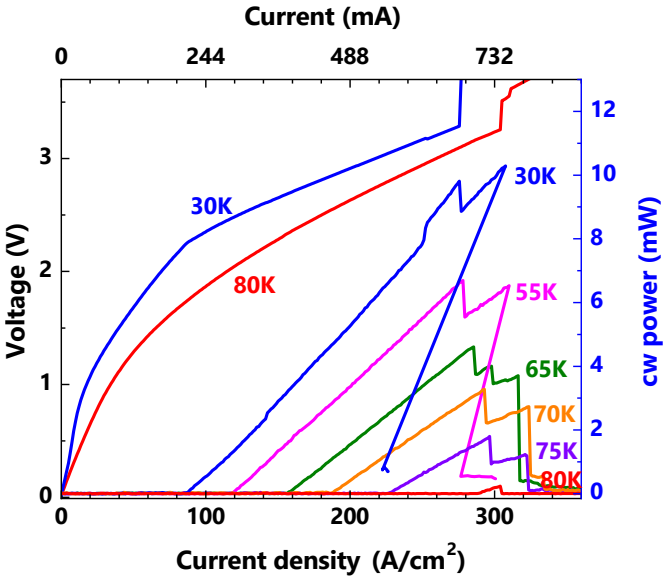

Fig. 2. L-J-V characteristics for several operating temperatures of QCL A under cw operation.

This laser can be operated in cw mode up to 80 K with a maximum output power of 10 mW at 30 K. At the latter temperature, the operating current range amounts to 0.21–0.75 A (86–307 A cm^{-2}), while the corresponding pump power is 0.45–2.94 W. For GaAs/AlAs THz QCLs based on the hybrid design, the typical ridge dimensions for QCLs operating in cw mode are about 0.12×1.00 mm^2. However, due to the extremely low threshold current density of this QCL (86 A cm^{-2} at 30 K), even a QCL with a cavity length of about 2 mm can be operated in a mechanical cryocooler with sufficient output power as well as a large dynamic range.

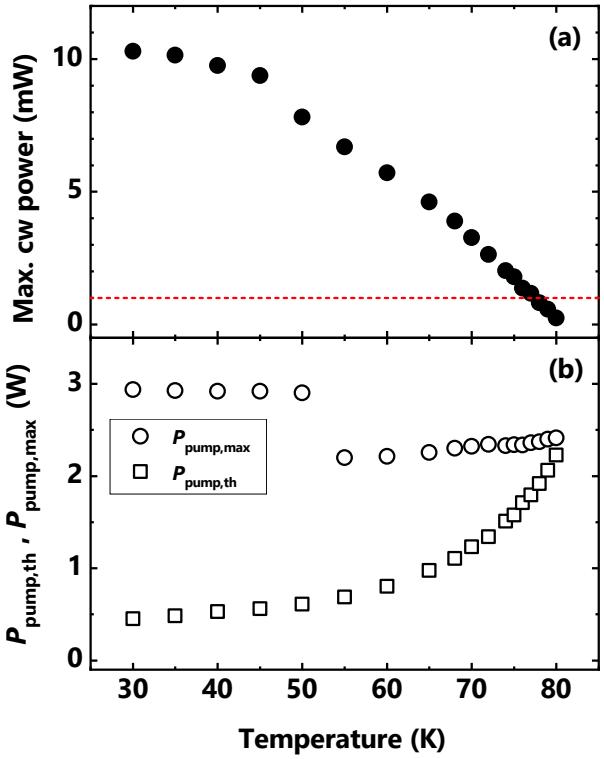

Fig. 3. (a) Maximum cw output power and (b) pump power at threshold $P_{pump,th}$ as well as at the maximum output power $P_{pump,max}$ of QCL A as a function of the heat sink temperature operated in a cryocooler. The dashed line in (a) indicates an output power of 1 mW.

Figure 3(a) depicts the maximum cw output power of QCL A as a function of heat sink temperature. The data show that T_{po} reaches 77 K, which is the highest value we have achieved so far using standard Fabry-Pérot resonators, i.e., without a high-reflectivity back-facet coating (cf. contri-

bution by B. Röben) or an additional mirror at the back facet. Figure 3(b) shows the temperature dependence of the pump power at threshold $P_{\mathrm{pump,th}}$ and at the maximum output power $P_{\mathrm{pump,max}}$. The jump of $P_{\mathrm{pump,max}}$ at 50 K is due to the change of the value for the applied current corresponding to the maximum cw output power. The pump powers mainly vary between 0.5 and 2.5 W. According to the cooling capacity of the cryocooler, QCL A can be stably operated in the cryocooler over a wide range of values for the applied current and operating temperature.

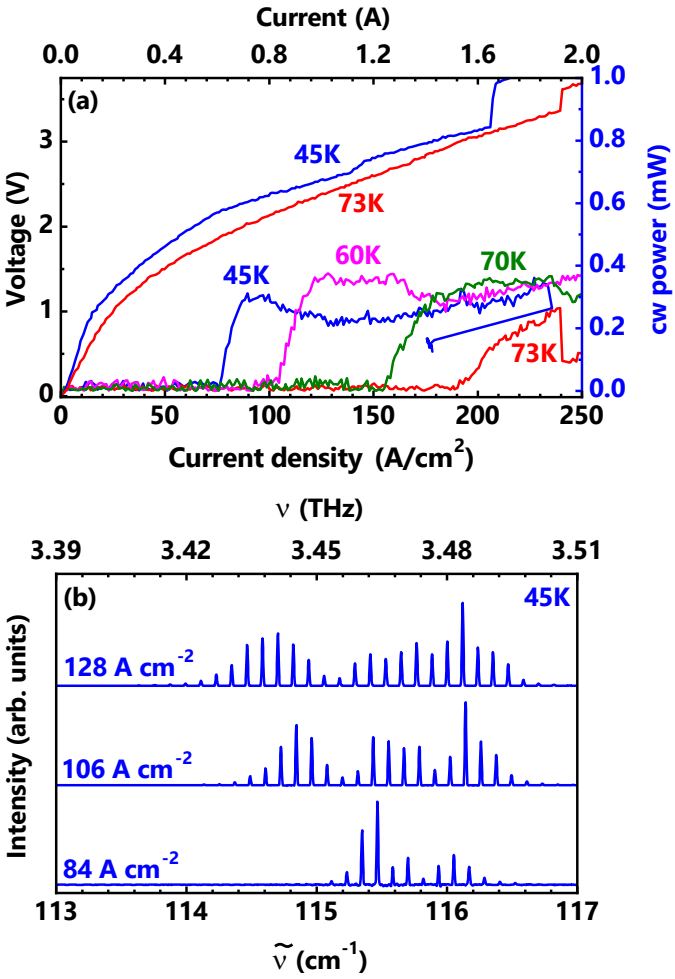

Fig. 4. (a) *L-J–V* characteristics for several operating temperatures and (b) lasing spectra for several current densities of QCL B under cw operation.

Figure 4(a) displays the *L-J–V* characteristics as a function of several operating temperatures for the long-cavity QCL B. The rather low cw output power can be explained by a non-optimal thermal contact between the QCL chip and the mount, since the laser ridge is longer than the standard size of the submount. In comparison with QCL A, self-heating is more significant in QCL B and needs to be carefully considered in further investigations. Nevertheless, this output power level is still sufficient for the measurement of the emission spectra. Figure 4(b) shows the emission spectra under cw operation at 45 K for several current densities. The multimode emission spectra cover a relatively large range of frequencies, while the mode spacing becomes 3.6 GHz (0.12 cm^{-1}). The broadband spectral coverage and small mode spacing are important for the development of frequency comb emission of THz QCLs.

The development of efficient THz QCLs with low pump powers based on this new design requires empirical investigations of the fine tuning of the thicknesses of individual layers and the optimization of the doping profile as well as numerical simulations of the (non-thermal) intra-subband carrier distributions and the possible carrier *cooling*. For the empirical investigations, long growth-run campaigns under stable conditions have to be carried out. If different MBE systems are used, a sufficient overlap of the respective growth campaigns are necessary, since different nominal design parameters

may be necessary to obtain identical parameters for the laser structure. The numerical investigation of the transport and optical properties requires an extension of our simulation tool to the full density matrix. Possible non-thermal intra-subband carrier distributions have to be taken into account, and electron-electron scattering rates have to be included. The combination of improved QCL designs with optimized resonator configurations may lead to the development of THz QCLs with T_{po} values towards 100 K.

Facts and Figures

Al Hassan, A., W. A. Salehi, R. B. Lewis, T. Anjum, C. Sternemann, L. Geelhaar, and U. Pietsch,
Transition from elastic to plastic strain release in core−shell nanowires revealed by in-plane x-ray diffraction,
Nanotechnol. **32**, 205705, 9 pages (2021).
DOI: 10.1088/1361-6528/abe5db

Al-Humaidi, M., L. Feigl, J. Jakob, P. Schroth, A. AlHassan, A. Davtyan, J. Herranz, T. Anjum, D. Novikov, S. Francoual, L. Geelhaar, T. Baumbach, and U. Pietsch,
In situ x-ray analysis of misfit strain and curvature of bent polytypic GaAs–$In_xGa_{1-x}As$ core–shell nanowires,
Nanotechnol. **33**, 015601, 11 pages (2022), published online 20 October, 2021.
DOI: 10.1088/1361-6528/ac29d8

Auzelle, T., M. Azadmand, T. Flissikowski, M. Ramsteiner, K. Morgenroth, C. Stemmler, S. Fernández-Garrido, S. Sanguinetti, H. T. Grahn, L. Geelhaar, and O. Brandt,
Enhanced radiative efficiency in GaN nanowires grown on sputtered TiN_x: effects of surface electric fields,
ACS Photonics **8**, 1718-1725 (2021).
DOI: 10.1021/acsphotonics.1c00224

Auzelle, T., F. Ullrich, S. Hietzschold, C. Sinito, S. Brackmann, W. Kowalsky, E. Mankel, O. Brandt, R. Lovrincic, and S. Fernández-Garrido,
External control of GaN band bending using phosphonate self-assembled monolayers,
ACS Appl. Mater. Interfaces **13**, 4626-4635 (2021).
DOI: 10.1021/acsami.0c17519

Bahrami, D., A. AlHassan, A. Davtyan, R. Zhe, T. Anjum, J. Herranz, L. Geelhaar, D. V. Novikov, R. Timm, and U. Pietsch,
Impact of electrical current on single GaAs nanowire structure,
Phys. Status Solidi B **258**, 2100056, 8 pages (2021).
DOI: 10.1002/pssb.202100056

Biermann, K., P. L. J. Helgers, A. Crespo-Poveda, A. S. Kuznetsov, A. Tahraoui, B. Röben, X. Lü, L. Schrottke, P. V. Santos, and H. T. Grahn,
In-situ control of molecular beam epitaxial growth by spectral reflectivity analysis,
J. Cryst. Growth **557**, 125993, 9 pages (2021).
DOI: 10.1016/j.jcrysgro.2020.125993

Boley, A., E. Luna, C. Zhang, N. Faleev, C. B. Honsberg, and D. J. Smith,
Interfacial intermixing and anti-phase boundaries in GaP/Si(0 0 1) heterostructures,
J. Cryst. Growth **562**, 126059, 7 pages (2021).
DOI: 10.1016/j.jcrysgro.2021.126059

Copetti, G., E. H. Nunes, T. O. Feijó, L. A. Galves, M. Heilmann, G. V. Soares, J. M. J. Lopes, and C. Radtke,
Strain-inducing photochemical chlorination of graphene nanoribbons on SiC (0001),
Nanotechnol. **32**, 145707, 6 pages (2021).
DOI: 10.1088/1361-6528/abd43a

Feldl, J., M. Feneberg, A. Papadogianni, J. Lähnemann, T. Nagata, O. Bierwagen, R. Goldhahn, and M. Ramsteiner,
Bandgap widening and behavior of Raman-active phonon modes of cubic single-crystalline $(In,Ga)_2O_3$ alloy films,
Appl. Phys. Lett. **119**, 042101, 6 pages (2021).
DOI: 10.1063/5.0056532

Harris, T. G. A. A., N. Heidary, S. Frielingsdorf, S. Rauwerdink, A. Tahraoui, O. Lenz, I. Zebger, and A. Fischer,
Electrografted interfaces on metal oxide electrodes for enzyme immobilization and bioelectrocatalysis,
ChemElectroChem **8**, 1329-1336 (2021).
DOI: 10.1002/celc.202100020

Heilmann, M., V. Deinhart, A. Tahraoui, K. Höflich, and J. M. J. Lopes,
Spatially controlled epitaxial growth of 2D heterostructures via defect engineering using a focused He ion beam,
Npj 2D Mater. Appl. **5**, 70, 7 pages (2021).
DOI: 10.1038/s41699-021-00250-z

Hernández-Mínguez, A., A. V. Poshakinskiy, M. Hollenbach, P. V. Santos, and G. V. Astakhov,
Acoustically induced coherent spin trapping,
Sci. Adv. **7**, eabj5030, 7 pages (2021).
DOI: 10.1126/sciadv.abj5030

Hoffmann, G., Z. Cheng, O. Brandt, and O. Bierwagen,
Drastically enhanced cation incorporation in the epitaxy of oxides due to formation and evaporation of suboxides from elemental sources,
APL Mater. **9**, 111110, 10 pages (2021).
DOI: 10.1063/5.0058541

Janzen, B. M., P. Mazzolini, R. Gillen, V. F. S. Peltason, L. P. Grote, J. Maultzsch, O. Bierwagen, R. Fornari, and M. R. Wagner,
Comprehensive Raman study of orthorhombic κ/ε-Ga_2O_3 and the impact of rotational domains,
J. Mater. Chem. C **9**, 14175-14189 (2021).
DOI: 10.1039/D1TC03500B

Janzen, B. M., P. Mazzolini, R. Gillen, A. Falkenstein, M. Martin, H. Tornatzky, J. Maultzsch, O. Bierwagen, and M. R. Wagner,
Isotopic study of Raman active phonon modes in β-Ga_2O_3,
J. Mater. Chem. C **9**, 2311-2320 (2021).
DOI: 10.1039/D0TC04101G

Jayasankar, D., V. Drakinskiy, N. Rothbart, H. Richter, X. Lu, L. Schrottke, H. T. Grahn, M. Wienold, H.-W. Hubers, P. Sobis, and J. Stake,
A 3.5-THz, ×6-harmonic, single-ended Schottky diode mixer for frequency stabilization of quantum-cascade lasers,
IEEE Trans. THz Sci. Technol. **11**, 684-694 (2021).
DOI: 10.1109/TTHZ.2021.3115730

Kaganer, V. M., O. V. Konovalov, and S. Fernández-Garrido,
Small-angle X-ray scattering from GaN nanowires on Si(111): Facet truncation rods, facet roughness and Porod's law,
Acta Crystallogr. Sect. A **77**, 42-53 (2021).
DOI: 10.1107/S205327332001548X

Kaganer, V. M., I. Petrov, and L. Samoylova,
Resolution of a bent-crystal spectrometer for X-ray free-electron laser pulses: Diamond versus silicon,
Acta Crystallogr. Sect. A **77**, 268-276 (2021).
DOI: 10.1107/S2053273321003697

Küpers, H., R. B. Lewis, P. Corfdir, M. Niehle, T. Flissikowski, H. T. Grahn, A. Trampert, O. Brandt, and L. Geelhaar,
Drastic effect of sequential deposition resulting from flux directionality on the luminescence efficiency of nanowire shells,
ACS Appl. Mater. Interfaces **13**, 50220-50227 (2021).
DOI: 10.1021/acsami.1c12371

Kuznetsov, A. S., D. H. O. Machado, K. Biermann, and P. V. Santos,
Electrically driven microcavity exciton-polariton optomechanics at 20 GHz,
Phys. Rev. X **11**, 021020, 16 pages (2021).
DOI: 10.1103/PhysRevX.11.021020

Lopes, J. M. J.,
Synthesis of hexagonal boron nitride: from bulk crystals to atomically thin films,
Prog. Cryst. Growth Charact. Mater. **67**, 100522, 33 pages (2021).
DOI: 10.1016/j.pcrysgrow.2021.100522

Lopes, J. M. J., D. Czubak, E. Zallo, A. I. Figueroa, C. Guillemard, M. Valvidares, J. Rubio-Zuazo, J. López-Sanchéz, S. O. Valenzuela, M. Hanke, and M. Ramsteiner,
Large-area van der Waals epitaxy and magnetic characterization of Fe_3GeTe_2 films on graphene,
2D Mater. **8**, 041001, 8 pages (2021).
DOI: 10.1088/2053-1583/ac171d

Lü, X., B. Röben, L. Schrottke, K. Biermann, and H. T. Grahn,
Correlation between frequency and location on the wafer for terahertz quantum-cascade lasers,
Semicond. Sci. Technol. **36**, 035012, 6 pages (2021).
DOI: 10.1088/1361-6641/abdd4b

Martinez, G., J. Wyzula, I. Mohelsky, C. Faugeras, M. Orlita, M. Potemski, A. Riedel, R. Hey, and K. J. Friedland,
Polaronic interaction in a single modulation-doped GaAs quantum well with the Feynman-Hellwarth-Iddings-Platzman approximation,
Phys. Rev. B **104**, 045312, 9 pages (2021).
DOI: 10.1103/PhysRevB.104.045312

Nicolai, L., K. Biermann, and A. Trampert,
Application of electron tomography for comprehensive determination of III-V interface properties,
Ultramicroscopy **224**, 113261, 8 pages (2021).
DOI: 10.1016/j.ultramic.2021.113261

Rio Calvo, M., J. Rodriguez, C. Cornet, L. Cerutti, M. Ramonda, A. Trampert, G. Patriarche, and É. Tournié,
Crystal phase control during epitaxial hybridization of III-V semiconductors with silicon,
Adv. Electron. Mater. **8**, 2100777, 10 pages (2021).
DOI: 10.1002/aelm.202100777

Ruiz-Cigarrillo, O., L. F. Lastras-Martínez, E. A. Cerda-Méndez, G. Flores-Rangel, C. A. Bravo-Velazquez, R. E. Balderas-Navarro, A. Lastras-Martínez, N. A. Ulloa-Castillo, K. Biermann, and P. V. Santos,
Optical anisotropies of asymmetric double GaAs (001) quantum wells,
Phys. Rev. B **103**, 035309, 6 pages (2021).
DOI: 10.1103/PhysRevB.103.035309

Runge, M., T. Kang, K. Biermann, K. Reimann, M. Woerner, and T. Elsaesser,
Mono-cycle terahertz pulses from intersubband shift currents in asymmetric semiconductor quantum wells,

Optica **8**, 1638-1641 (2021).
DOI: 10.1364/OPTICA.438096

Scolfaro, D., M. Finamor, L. O. Trinchão, B. L. T. Rosa, A. Chaves, P. V. Santos, F. Iikawa, and O. D. D. Couto,
Acoustically driven Stark effect in transition metal dichalcogenide monolayers,
ACS Nano **15**, 15371-15380 (2021).
DOI: 10.1021/acsnano.1c06854

Takagaki, Y.,
Quantum magnetotransport oscillations in graphene nanoribbons coupled to superconductors,
J. Phys.: Condens. Matter **33**, 255301, 12 pages (2021).
DOI: 10.1088/1361-648X/abf8d1

Takagaki, Y.,
Charge storage in metal-chalcogenide bilayer junctions,
J. Phys. D: Appl. Phys. **54**, 295105, 8 pages (2021).
DOI: 10.1088/1361-6463/abfbf8

Takagaki, Y., M. Hanke, and M. Ramsteiner,
Surfactant-induced alterations of epitaxial orientation in β-In_2S_3 layers on InP,
Cryst. Growth Des. **21**, 6314-6320 (2021).
DOI: 10.1021/acs.cgd.1c00756

Terker, M., L. Nicolai, S. Gaucher, J. Herfort, and A. Trampert,
In Situ transmission electron microscopy of disorder–order transition in epitaxially stabilized $FeGe_2$,
J. Phys. Chem. C **125**, 2779-2784 (2021).
DOI: 10.1021/acs.jpcc.0c10716

Tornatzky, H., C. Robert, P. Renucci, B. Han, T. Blon, B. Lassagne, G. Ballon, Y. Lu, K. Watanabe, T. Taniguchi, B. Urbaszek, J. M. J. Lopes, and X. Marie,
Spin dependent charge transfer in $MoSe_2$/hBN/Ni hybrid structures,
Appl. Phys. Lett. **119**, 263103, 6 pages (2021).
DOI: 10.1063/5.0075554

van Deurzen, L., M. Gómez Ruiz, K. Lee, H. Turski, S. Bharadwaj, R. Page, V. Protasenko, H. (Grace) Xing, J. Lähnemann, and D. Jena,
Dislocation and indium droplet related emission inhomogeneities in InGaN LEDs,
J. Phys. D: Appl. Phys. **54**, 495106, 10 pages (2021).
DOI: 10.1088/1361-6463/ac2446

Varotto, S., L. Nessi, S. Cecchi, J. Sławińska, P. Noël, S. Petrò, F. Fagiani, A. Novati, M. Cantoni, D. Petti, E. Albisetti, M. Costa, R. Calarco, M. Buongiorno Nardelli, M. Bibes, S. Picozzi, J.-P. Attané, L. Vila, R. Bertacco, and C. Rinaldi,
Room-temperature ferroelectric switching of spin-to-charge conversion in germanium telluride,
Nat. Electron. **4**, 740-747 (2021).
DOI: 10.1038/s41928-021-00653-2

Vogt, P., F. V. E. Hensling, K. Azizie, C. S. Chang, D. Turner, J. Park, J. P. McCandless, H. Paik, B. J. Bocklund, G. Hoffmann, O. Bierwagen, D. Jena, H. G. Xing, S. Mou, D. A. Muller, S.-L. Shang, Z.-K. Liu, and D. G. Schlom,
Adsorption-controlled growth of Ga_2O_3 by suboxide molecular-beam epitaxy,
APL Mater. **9**, 031101, 13 pages (2021).
DOI: 10.1063/5.0035469

Wang, R., R. Calarco, F. Arciprete, and V. Bragaglia,
Epitaxial growth of GeTe/Sb_2Te_3 superlattices,
Mater. Sci. Semicond. Process **137**, 106244, 5 pages (2022), published online 5 October, 2021.
DOI: 10.1016/j.mssp.2021.106244

Windsor, Y. W., D. Zahn, R. Kamrla, J. Feldl, H. Seiler, C.-T. Chiang, M. Ramsteiner, W. Widdra, R. Ernstorfer, and L. Rettig,
Exchange-striction driven ultrafast nonthermal lattice dynamics in NiO,
Phys. Rev. Lett. **126**, 147202, 8 pages (2021).
DOI: 10.1103/PhysRevLett.126.147202

Wojnar, P., J. Płachta, A. Reszka, J. Lähnemann, A. Kaleta, S. Kret, P. Baranowski, M. Wójcik, B. J. Kowalski, L. T. Baczewski, G. Karczewski, and T. Wojtowicz,
Near-infrared emission from spatially indirect excitons in type II ZnTe/CdSe/(Zn,Mg)Te core/double-shell nanowires,
Nanotechnol. **32**, 495202, 7 pages (2021).
DOI: 10.1088/1361-6528/ac218c

Wong, M. H., O. Bierwagen, R. J. Kaplar, and H. Umezawa,
Ultrawide-bandgap semiconductors: an overview,
J. Mater. Res. **36**, 4601-4615 (2021).
DOI: 10.1557/s43578-021-00458-1

Xu, H., R. Wu, J.-Y. Zhang, W. Han, L. Chen, X. Liang, C. Y. Haw, P. Mazzolini, O. Bierwagen, D.-C. Qi, and K. H. L. Zhang,
Revealing the electronic structure and optical properties of $CuFeO_2$ as a p-Type oxide semiconductor,
ACS Appl. Electron. Mater. **3**, 1834-1841 (2021).
DOI: 10.1021/acsaelm.1c00090

Yuan, M., K. Biermann, S. Takada, C. Bäuerle, and P. V. Santos,
Remotely pumped GHz antibunched emission from single exciton centers in GaAs,
ACS Photonics **8**, 758-764 (2021).
DOI: 10.1021/acsphotonics.1c00094

Zaytseva, Yu. S., N. I. Borgardt, A. S. Prikhodko, E. Zallo, and R. Calarko,
Electron Microscopy Study of Surface Islands in Epitaxial $Ge_3Sb_2Te_6$ Layer Grown on a Silicon Substrate,
Crystallogr. Rep. **66**, 687-693 (2021).
DOI: 10.1134/S1063774521030317

Ph. D. Theses

Freudenfeld, Jaan
Coupling Quantum Point Contacts via Ballistic Electron Optics
Freie Universität Berlin, February 2021

Gaucher, Samuel
Growth of lattice-matched hybrid semiconductor-ferromagnetic trilayers using solid-phase epitaxy
Humboldt-Universität zu Berlin, March 2021

Helgers, Paulus Leonardus Joseph
Acoustic Charge and Spin Transport in Sidewall Quantum Wires on GaAs (001) Substrates
Humboldt-Universität zu Berlin, August 2021

Kuşdemir, Erdı
Investigation of periodic Mg doping in (0001) (Ga,In)N/GaN superlattices grown on by plasma-assisted molecular beam epitaxy (PAMBE) for hole injection in light emitting diodes
Humboldt-Universität zu Berlin, November 2021

Master Theses

Isceri, Stefania
Epitaxy of Two-Dimensional Tellurium on Silicon: A Combined Experimental and First-Principles Study
Politecnico di Milano, April 2021

Pudelski, Maximilian
Wachstum durch Molekularstrahlepitaxie und Simulationen von GaN/(In,Ga)N-Heterostrukturen auf "top-down"-produzierten GaN-Nanodrähten
Humboldt-Universität zu Berlin, June 2021

Graser, Karl
TEM Untersuchungen der Defektstruktur in epitaktischen GaSb/GaAs/Si-Schichtsystemen
Humboldt-Universität zu Berlin, July 2021

Ibáñez Romero, Pablo
Characterization of metastable FeGe2 thin films
Technische Universität Darmstadt, November 2021

Students Working on their Master Thesis

Castro Martínez, Aron Ernesto
Humboldt-Universität zu Berlin

Litschauer, Maximilian
Humboldt-Universität zu Berlin

Seminars of visitors (zoom-meetings)

08.02.2021
Andreas K. Hüttel, Universität Regensburg
Single nanotube optomechanics and quantum electronics

15.03.2021
Dominik Bühler, University of Valencia
On-chip acousto-optical modulators for integrated quantum photonics

23.08.2021
Oliver Marquardt, Weierstraß-Institut für angewandte Analysis und Stochastik
Modelling the electronic properties of semiconductor nanowire heterostructures

01.11.2021
Alex Fainstein, Centro Atómico Bariloche and Instituto Balseiro, Argentina
Optomechanical parametric oscillation of a quantum light-fluid in a lattice

Budget Summary

Fiscal year	2020 (actual amount)	2021 (actual amount)
	k€	k€
Revenues		
Allocations	9,257.5	9,998.9
Earnings	42.3	31.0
Sum	9,299.8	10,029.9
Expenditures		
Staff	5,385.3	5,315.6
Administrative expenses	2,356.4	2,584.3
Equipment investment funds	1,060.9	1,302.7
Sum	8,802.6	9,202.6
External funding through projects		
Granted funds	2.005.8*	2.309.0*
Spent funds	862.4	989.8

Summary of External Funding

Agency	Period	Title	Project leader	FST
BMBF	15.04.2018 – 31.01.2021	Monolithically integrated laser made from III-V nanowires for silicon photonics (MILAS)	Dr. Lutz Geelhaar	9186
BMBF	01.06.2018 – 31.03.2022	InterPOL - Verbundprojekt: Polariton lattices: a solid-state platform for quantum simulations of correlated and topological states - Teilvorhaben: Development of polariton lattices with correlated and topological states for quantum simulation	Dr. Paulo V. Santos	9192
EFRE	01.08.2016– 31.03.2022	Application laboratory electron tomography	Dr. Achim Trampert	9178
DAAD	01.01.2021 – 31.12.2022	(In,Ga)N overgrowth of top-down nanowire heterostructures	Dr. Jonas Lähnemann	9215
DFG	01.12.2015– 31.12.2023	Quantum Hall based Aharonov-Bohm spectroscopy: electron-electron interaction in non-linear magnetotransport	Dr. PD. Stefan Ludwig	9174
DFG	01.05.2017- 30.09.2021	Nonequilibrium phenomena and interactions in ultrapure III-V nanowires	Dr. PD. Stefan Ludwig	9180
DFG	01.03.2018 – 31.05.2021	Coherent acousto-optical interactions in structured polariton microcavities	Dr. Alexander Kuznetsov	9190
DFG	01.10.2018 – 30.09.2021	Coherent acousto-optical interactions in structured polariton microcavities	Dr. Paulo V. Santos	9191
DFG	01.11.2018 – 29.02.2024	Controlling Electron-Phonon Interaction in Nanocircuits — Strong Coupling Regime	Dr. PD. Stefan Ludwig	9195
DFG	01.04.2019 – 31.03.2022	Controlling Electron-Phonon Interaction in Nanocircuits — Strong Coupling Regime	Dr. Paulo V. Santos	9196
DFG	01.05.2019 – 31.10.2022	Far-infrared magneto-spectroscopy of novel semiconductor materials in megagauss magnetic fields using quantum-cascade lasers	Prof. Dr. Holger T. Grahn	9200
DFG	01.06.2020 – 31.05.2023	Artificial quantum states on semiconductor surfaces created and probed by cryogenic scanning tunneling microscopy	Dr. Stefan Fölsch	9209
DFG	01.04.2021 – 31.03.2024	Nanoscale optomechanical interactions in semiconductor microcavities	Dr. Paulo V. Santos	9208
DFG	01.01.2021 – 31.12.2023	Charge carrier dynamics under the influence of extreme strain gradients realized in bent semiconductor nanowires	Dr. Lutz Geelhaar	9210
DFG	01.02.2021 – 31.01.2024	Photoelectrochemical CO_2 conversion with tunable semiconductor nanostructures	Dr. Lutz Geelhaar	9213

DFG	01.03.2021 – 29.02.2024	Point defects control in Ga_2O_3 thin films grown via molecular beam epitaxy	Dr. Oliver Bierwagen	9217
DFG	01.09.2021 – 31.08.2024	New strategies for dislocation density reduction in monolithic III/V epitaxy on Si	Dr. Achim Trampert	9218
ESA/ DLR	12.02.2019 – 30.09.2021	Frequency stabilization of a Quantum Cascade Laser for Supra-THz applications	Prof. Dr. Holger T. Grahn	9201
EU	01.01.2019 – 30.06.2022	BeforeHand – Boosting Performance of Phase Change Devices by Hetero- and Nano-Structure Material Design	Dr. Stefano Cecchi	9199
WGL (SAW)	01.04.2018 – 31.03.2022	Barium stannate based heterostructures for electronic applications (BaSTet)	Dr. Oliver Bierwagen	9194
WGL (SAW)	01.06.2018 – 31.12.2021	Terahertz detection of atoms in plasma processes (TERAPLAS)	Prof. Dr. Holger T. Grahn	9168
WGL (SAW)	01.07.2021 – 30.06.2024	Defect-engineering in graphene via focused ion beam for tailored van der Waals epitaxy of h-BN (ENGRAVE)	Dr. J. Marcelo J. Lopes	9216
WGL (SAS)	01.07.2020 – 30.06.2024	Growth and fundamentals of oxides for electronic applications (GraFOx II)	Dr. Oliver Bierwagen	9211

Staff

(December 31, 2021)
Scientific staff: including Ph. D. students (D) and externally funded personnel (P)

Aggarwal, Neha	Defect-engineering in graphene for tailored van der Waals epitaxy of hexagonal BN
Ardenghi, Andrea (D, P)	Point defects control in Ga_2O_3 thin films grown via molecular beam epitaxy
Ashurbekov, Nazim (D, P)	Radio-frequency phonon resonators for coherent electron-phonon coupling
Auzelle, Thomas	Epitaxy of group-III nitride nanowires and related applications
Ayuso Pérez, Irene (D)	Quantum transport in nanowires
Biermann, Klaus	Molecular beam epitaxy of GaAs-based advanced heterostructures
Bierwagen, Oliver	Molecular beam epitaxy of oxides
Brandt, Oliver	Group-III nitrides and semiconductor nanowires
Dinh, Duc Van	Growth of (Sc,Al)N thin films
Egbo, Kingsley Onyekachi	P-type semiconducting oxides and solid-phase epitaxy of metastable group-III sesquioxide alloys
Engel-Herbert, Roman	Director
Flissikowski, Timur	Ultrafast dynamics of semiconductor structures
Fölsch, Stefan	Low-temperature scanning tunneling microscopy and spectroscopy
Geelhaar, Lutz	Molecular beam epitaxy and semiconductor nanowires
Gómez Ruiz, Mikel (D)	Cathodoluminescence spectroscopy and correlated chemical and structural analysis of core/shell nanowires
Grahn, Holger	Optical and electrical properties of semiconductor nanostructures
Graser, Karl (D, P)	Transmission electron microscopy on dislocation reduction in III-V on Si heterostructures
Hanke, Michael	Synchrotron x-ray diffraction
Hellemann, Jan (D)	Electron-phonon interaction in nanostructures
Herfort, Jens	Ferromagnet-semiconductor heterostructures
Hernández Mínguez, Alberto	Manipulation of optical and electronic properties of low-dimensional structures using surface acoustic waves
Hoffmann, Georg (D, P)	Growth and doping of $BaSnO_3$ and $LaInO_3$
Hucho, Carsten	Technology and transfer
Jordão Lopes, João Marcelo	Epitaxy of two-dimensional materials
Kaganer, Vladimir	Theories of molecular-beam-epitaxial growth and x-ray scattering
Kang, Jingxuan (D, P)	Top-down synthesis and optical properties of ordered (In,Ga)N nanowire arrays
Kurlov, Sergii (P)	Terahertz quantum-cascade lasers for far-infrared magneto spectroscopy in pulsed megagauss magnetic fields
Kuznetsov, Alexander (P)	Coherent electro-optomechanics at GHz frequencies with confined microcavity exciton-polaritons
Lähnemann, Jonas	Spatially resolved optical spectroscopy and structural as well as compositional analysis of nanostructures

Lü, Xiang (P)	Terahertz quantum-cascade lasers
Ludwig, Stefan	Quantum transport in nanoelectronic systems
Luna Garcia de la Infanta, Esperanza	Transmission electron microscopy of heterointerfaces
Lv, Hua	Spin-transport phenomena in layered and two-dimensional magnetic materials
Marín Largo, Francisca (D, P)	Growth and luminescence analysis of bent GaAs nanowires
Oliva, Miriam (D)	Photoluminescence spectroscopy of ordered nanowire arrays
Paysen, Ekaterina (D, P)	Multi-scale electron tomography of interfaces.
Pham, Van Dong (P)	Atom manipulation on III-V semiconductors by low-temperature scanning tunneling microscopy
Ramsteiner, Manfred	Electronic, vibrational, and magnetic properties of semiconductors
Reis, Anna (D, P)	In-situ x-ray scattering study of surface and interface dynamics at growing crystalline layers
Richter, Steffen (P)	Student assistant BALET
Santos, Paulo	Acoustic, optic, and magnetic properties of nanostructures
Schrottke, Lutz	Quantum-cascade lasers and optical properties of heterostructures
Sırt, Serkan (D, P)	Interplay between the quantum Hall and Aharonov-Bohm effects in mesoscopic circuits
Tahraoui, Abbes	Comprehensive semiconductor technology
Takagaki, Yukihiko	Electric properties of nanometer-scale materials
Trampert, Achim	Microstructure and electron microscopy
Yuan, Mingyun (P)	Optomechanical interaction between exciton polaritons and acoustic phonons

Non-Scientific Staff

Anders, Walid	Technology
Arnhold, Kerstin	Finances/Purchasing
Baumann, René	Workshop
Behnke, Steffen	Technician
Bluhm, Anne-Kathrin	Technician
Ehrensack, Kerstin	Technician
Ferber, Thomas	Workshop
Geike, Janka	Technician
Hablizel, Kai (P)	European and National Grant Management and Equal Opportunities Officer
Hartung, Andreas	Human Resources and Travel Management
Heinitz, Sebastian	Electrician
Herrmann, Claudia	Technician
Kentchadze, Tamar	Student Assistant Library
Krauß, Sabine	Technician and Chairwoman Works Council
Matzeck, Christopher	Technician
Matzeck, Margarita	Technician
Morgenroth, Katrin (P)	Technician
Pakulat, Bernd	Head of IT and Data Protection Officer
Pfeiffer, Astrid	Technician
Pfeiffer, Jörg	Head of Workshop
Rauwerdink, Sander	Technology
Reischel, Mercedes	Transfer Management
Schönherr, Hans-Peter	Technician
Seidel, Werner	Technology
Sieg, Michael	Workshop
Steffen, Doreen	Technician
Stemmler, Carsten	Technician
Suchilina, Ekaterina	Office Assistant
Timm, Anne Susanne	Library
Venohr, Thomas	Workshop
Wendt, Christian	Intern IT
Wirsig, Arno	Technology
Wirt-Brunnckow, Andreas	IT